EFFECT OF LOAD RATE ON THE FRACTURE TOLERANCE OF THE TIBIA

THE EFFECT OF LOAD RATE ON THE AXIAL FRACTURE TOLERANCE OF THE ISOLATED TIBIA DURING AUTOMOTIVE AND MILITARY IMPACTS

By ALBERTO A. MARTINEZ, B.Eng.

A Thesis Submitted to the School of Graduate Studies in Partial Fulfilment of the Requirements for the Degree Master of Applied Science

McMaster University MASTER OF APPLIED SCIENCE (2016) Hamilton, Ontario
(Mechanical Engineering)

TITLE:	The effect of load rate on the axial fracture tolerance of the isolated tibia during automotive and military impacts
AUTHOR:	Alberto A. Martinez, B.Eng.
SUPERVISOR:	Cheryl E. Quenneville, B.Sc., M.E.Sc., Ph.D.
NUMBER OF PAGES:	xv, 151

Lay Abstract

Fractures of the lower leg are common during frontal automotive collisions and military blasts. Due to the viscoelastic nature of bone, it remains unclear whether safety limits from automotive experiments can be applied to higher-rate blasts. The purpose of this work was to study the effect of load rate on the fracture tolerance of the tibia during these two scenarios.

Impact testing was performed on twelve human cadaveric tibias. Specimens impacted at higher rates required greater forces to achieve fracture, which suggests that load rate needs to be accounted for in future injury criteria. Two commonly used crash test dummy lower legs were tested under similar loading conditions, and a finite element model was developed and tested to simulate loading of the tibia during high-rate impacts.

The results of this work can be used to design and evaluate improved protective systems to be implemented in vehicles.

Abstract

Fractures of the lower leg are common during frontal automotive collisions and military blasts. These two scenarios cause injury via a similar axial loading mechanism. The majority of previous studies that have conducted axial impact tests to determine the injury limits of the lower leg have simulated automotive impacts; however, due to the viscoelastic nature of bone, it remains unclear whether limits from automotive experiments can be applied to higher-rate blasts. The purpose of this work was to study the effect of load rate on the fracture tolerance of the tibia during these two scenarios.

The instrumentation required to quantify impacts to lower leg specimens using a pneumatic impactor was developed, and included capturing synchronized load, acceleration, velocity, strain, and high-speed video data. Subsequently, impact testing was performed on twelve human cadaveric tibias. Velocities and impact durations were matched to literature values to simulate an automotive collision and a military blast. Force and impulse were found to significantly differ between the two conditions, while kinetic energy did not. Specimens impacted at higher rates required greater forces to achieve fracture, which suggests that load rate needs to be accounted for in future injury criteria. Two commonly used anthropomorphic test device lower legs were tested under similar loading conditions, and new thresholds were developed for these devices. Finally, a finite element model was tested for its ability to simulate loading of the tibia during varied impacts. This model can be used to assess injury risk and protective measures for the leg.

Understanding the effect of load rate on the tibia’s fracture tolerance is essential when developing injury thresholds that can be applied to impacts of various rates. The

results of this work can be used in the future to design and evaluate improved protective systems to be implemented in vehicles.

Acknowledgements

I would like to thank my supervisor, Dr. Cheryl Quenneville, for her guidance, support, and giving me the opportunity to pursue my graduate studies. I truly appreciate her mentorship, encouragement, and ability to remain optimistic when things were not going well. I don't think I could've worked with a better supervisor. I would also like to thank Dr. Wohl, who could always be relied on for support around the lab, and most of all, a good laugh.

I'd like to thank my lab mates at the Injury Biomechanics Lab: Chris, Avery, Clodagh, Fatemeh, Ishan, Muir, and Cooper, who always made a day in the lab or the office fun. Special shout outs must go to Chris, for answering my endless modelling questions, and Avery, for the support and entertainment during testing despite the long hours spent in the lab. I must also thank the guys in the machine shop: Mark, John, Dan, Ron, and Mike, who always provided fantastic design advice and were incredibly patient when dealing with my lack of machining and electronics knowledge.

Outside of school, I would like to thank Meliss, who I could always rely on for enthusiasm, motivation, and for always asking how my day was.

Most of all, I'd like to thank my family for their support, especially my parents, who have sacrificed a lot to give me better opportunities in life. I certainly wouldn't be here without them. ¡Los quiero mucho, ustedes!

Lastly, I'd like to acknowledge McMaster University for providing me with the funding to conduct this work.

Table of Contents

List of Figures

List of Tables

List of Abbreviations, Symbols, and Nomenclature

°	degree
ρ	density
”	inch
α	level of significance
%	percent
±	plus/minus
ν	Poisson’s ratio
1D	one-dimensional
3D	three-dimensional
ABS	accrylonitrile butadiene styrene
ATD	anthropomorphic test device
BNC	Bayonet Neill–Concelman electrical connector type
CAD	computer aided design
cm	centimetre
CT	computed tomography
DAQ	data acquisition system
F	force
FE	finite element
g	standard acceleration due to gravity
GPa	gigapascal
HU	Houndsfield units
J	joule

kg	kilogram
KE	kinetic energy
kHz	kilohertz
kN	kilonewton
LED	light-emitting diode
m	metre
mm	millimetre
MPa	megapascal
ms	millisecond
mV	millivolt
N	Newton
NATO	North Atlantic Treaty Organization
NI	National Instruments
psi	pounds per square inch
PMHS	post-mortem human subjects
PMMA	polymethyl methacrylate
PVC	polyvinyl chloride
R^2	coefficient of determination
s	second
STL	stereolithography file format
V	volt

Declaration of Academic Achievement

The following is a declaration that I, Alberto Martinez, completed the research outlined in this thesis and recognizes the contributions of Dr. Cheryl Quenneville, Avery Chakravarty, and Clodagh Duffy. I contributed to the study, performed the experimental testing, data analysis, finite element model creation, and writing of the thesis. Dr. Cheryl Quenneville assisted with the study design and review of the thesis, and developed the finite element mesh of the tibia. Avery Chakravarty assisted with experimental impact testing. Clodagh Duffy developed the finite element mesh of several of the components used in the current experimental testing configuration.

CHAPTER 1 – INTRODUCTION

Overview: *Fractures of the distal tibia are common during frontal automotive collisions and military underbody blasts, where loads are transferred to the leg through the floor plate. Most of the research to determine the injury tolerance in this region has been conducted by the automotive field, and it remains unknown whether protective standards based on limits from automotive studies can be applied to higher-rate military scenarios. This introductory chapter outlines the anatomy of the lower leg, surrogates that are commonly used to determine injury limits for the lower leg, previous experimental and computational work that has been conducted to determine these limits, and it concludes with the study rationale, objectives, and hypotheses for this work.*[1]

1.1 Motivation

Motor vehicle crashes remain a major cause of serious injury to the general population, with 6.3 million police-reported crashes occurring in the United States in 2015, leading to 2.44 million injured people (National Highway Traffic Safety Administration 2016). The implementation of improved safety mechanisms in automobiles for the head and thorax (*e.g.*, seatbelts, airbags) has shifted the focus of injuries to other areas of the body, particularly the lower extremity (Seipel *et al.* 2001).

---

[1] Due to the interdisciplinary nature of this work, a glossary of anatomical terms is included in Appendix A.

Improvements to modern restraint systems have led to an increase in the number of occupants that survive what once were fatal high-energy collisions but still sustain lower extremity injuries (Burgess *et al.* 1995, Dischinger *et al.* 2004). During frontal collisions, the lower extremity has become the second most injured region of the body after the head, encompassing approximately 30% of all moderate to severe injuries (Morgan *et al.* 1991, Pattimore *et al.* 1991), and is often the site of the most severe injury (Pattimore *et al.* 1991). Lower extremity injuries also occur commonly in military settings. Data from combats in Iraq and Afghanistan show that lower limb injuries occur in 45% of all casualties (Ramasamy *et al.* 2011a).

Fractures of the distal portion of the tibia, or pilon fractures, while typically not life-threatening, are considered to be one of the severest forms of injury to the lower extremity, and are the most important in terms of disability and impairment (Kitagawa *et al.* 1998, Ramasamy *et al.* 2013). These fractures tend to be high-energy injuries and involve the disruption of the roof of the ankle joint. Due to the ankle being a weight bearing joint and cartilage in this region being poorly vascularized, pilon fractures can be one of the most challenging orthopaedic injuries to treat, often resulting in long term complications including infection, malunion, and osteoarthritis (Helfet *et al.* 1994, Funk *et al.* 2002).

Pilon fractures that occur during automotive collisions and military scenarios are caused by the same injury mechanism (Bailey *et al.* 2015). These fractures result from the talus being driven into the distal tibia, comminuting the metaphyseal bone and occasionally extending to the proximal diaphysis (Jacob *et al.* 2015). In frontal automotive collisions, axial loads are transferred along the long axis of the lower leg due to floor intrusion or interaction with the vehicle's pedals (Klopp *et al.* 1997). In military scenarios, blasts occur below the vehicle's body and cause the floor plate to deflect upwards, transferring a great amount of energy to the lower leg (Ramasamy *et al.* 2011a). However, the magnitude of velocity and duration of the impact vary between the two scenarios. Automotive floor intrusions typically have velocities between 2 and 6 m/s (Crandall *et al.* 1998, McKay and Bir 2009), and impacts lasting between 15 and 45 ms (McKay and Bir 2009). Meanwhile, floor plate velocities during military scenarios have been reported to exceed 12 m/s (Wang *et al.* 2001), with load durations less than 10 ms (North Atlantic Treaty Organization HFM-090 Task Group 25 2007). The long term impairment and rehabilitation process that is associated with these injuries lead to high economic burden (Owen and Lowne 2001). In order to reduce these societal costs that accompany these fractures, it is essential to understand the fracture mechanisms and injury limits in these areas and design appropriate preventative systems and repair procedures.

Several studies have conducted experiments to determine the injury limits of the cadaveric lower leg during axial loading. For practical and ethical reasons, impact testing cannot be conducted on humans *in vivo*, so human surrogates are used instead. These surrogates are usually post-mortem human subjects (PMHS), anthropomorphic test devices (ATDs) or commonly "crash test dummies", or computational models.

The majority of research that has investigated the injury limit of the cadaveric lower leg during axial impacts has been carried out with an automotive focus. However, due to the viscoelastic properties of bone, it remains unclear whether results from automotive experiments can be successfully applied to higher loading rate military blasts. Most of these studies have used the intact lower limbs and have delivered loads to the plantar surface, along the axis of the shank. While the use of intact limbs may be more representative of humans during impacts, it adds a high degree of complexity that does not allow for the direct investigation of the injury tolerance of a specific bone, as load may be dissipated through soft tissue deformation and joint articulation.

Anthropomorphic test devices, or crash test dummies, are human surrogates that aim to represent the dimensions, geometry, mass distribution, and joint articulations of a specific human population. They were originally designed by the automotive industry to evaluate risk of injury during crash testing (Mertz 1993) ATDs are placed in a vehicle during a simulated collision and data recorded through instrumentation built into the body segments. The Hybrid III 50th percentile male ATD (Humanetics Innovative Solutions, Plymouth, MI, USA) is currently the most widely used dummy to evaluate injury during frontal collisions. Despite being originally designed for automotive collisions, the Hybrid III has been used to assess injury during military loading (McKay and Bir 2009). Concern over the Hybrid III lower leg’s ability to predict injury in higher-rate scenarios led to the development of the MIL-LX (Military Lower Extremity) lower leg (Humanetics Innovative Solutions, Plymouth, MI, USA), to be used specifically to analyze anti-vehicular land mine protective systems. In order to determine an ATD’s ability to predict injury, their response needs to be compared to actual human response during loading.

While there are several experimental studies of lower leg injury tolerance, there are numerous limitations to this type of testing. Testing using cadaveric specimens is costly and impacts cannot be repeated after failure, and while ATDs may replicate the mass of human segments, their geometry and articulation are not perfectly accurate, they cannot replicate fracture, and are often overly stiff. Computer modeling through finite element analysis (FEA) is a powerful tool that allows for repeated testing in multiple configurations. Once a FE model has been built, the user can specify any number of impact conditions to study, which makes FE modelling an inexpensive tool. The models allow for measurement of displacement, strain, and stress at any location in the model, eliminating the complications that may arise when instrumenting a cadaveric specimen. FE models are typically created using specimen geometries extracted from medical imaging scans, which allow for accurate model geometry.

The overall purpose of this research was to investigate the effect of impact duration and impulse on the fracture tolerance of the tibia during axial automotive and military impacts, to evaluate the performance of the Hybrid III and MIL-LX legs under these impact conditions, and to further develop a finite element model of the tibia that can predict injury under these loads.

1.2 Anatomy of the Lower Leg

The lower leg refers to the region of the body distal to the knee, which consists of the shank, ankle, and foot. The shank is made up of two long bones, the tibia and the fibula, which articulate with the femur and patella at the knee and run along the length of the shank to articulate distally with the talus (Figure 1.1). The tibia runs along the medial side of the shank, while the fibula runs along the lateral side. The tibia bears the majority of the weight supported by the leg, approximately 90% (Takebe *et al.* 1984).

Like other long bones, the tibia is composed of a diaphysis, or the shaft of the tibia, and two epiphyses, the rounded extremities at each end of the bone. The proximal epiphysis of the tibia is made up of two condyles, a lateral and medial condyle, which are both flattened in the transverse plane. The flattened surface of the condyles is called the tibial plateau, which articulates with the femur to form the tibiofemoral joint. The shaft of the tibia is generally triangular in cross-section, forming a medial, lateral, and posterior surface. The anterior crest of the tibia is a bony prominence that runs along the diaphysis of the bone and separates the medial and lateral surfaces. The distal articular surface of the tibia, called the plafond, articulates with the talus at the ankle.

The ankle is the region where the shank and the foot meet, and is comprised of four bones: the tibia, the fibula, the talus, and the calcaneus. The ankle is made up of three joints: the talocrural joint that connects the distal ends of the tibia and fibula to the talus, the subtalar joint that connects the talus to the calcaneus, and the inferior tibiofibular joint which connects the distal end of the tibia to the fibula.

The foot is a complex mechanical structure that contains 26 bones, including the talus, calcaneus, cuneiforms, cuboid, navicular, metatarsals, and phalanges, and 33 joints.

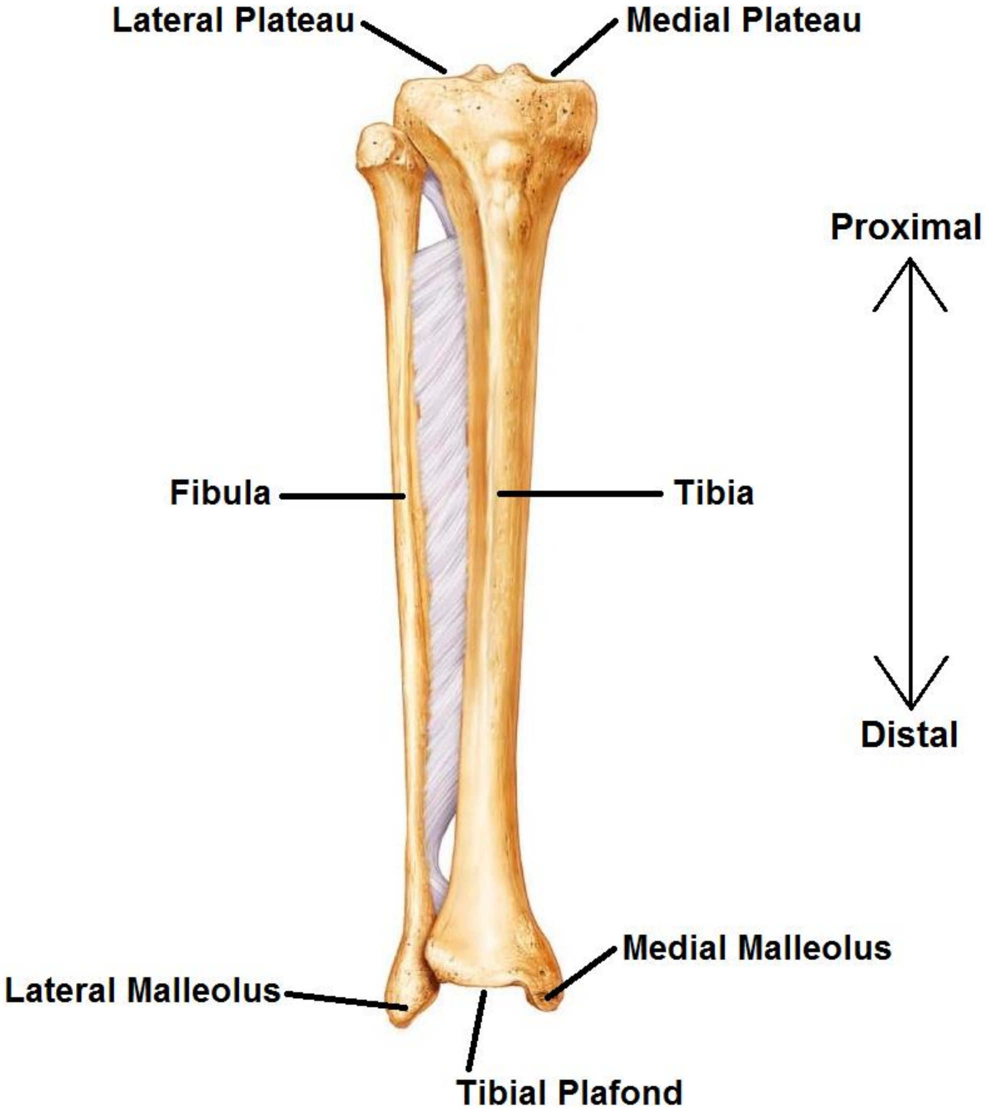

Figure 1.1: Lower Leg Anatomy
Frontal view of the bones of the right-sided lower leg, with key anatomical landmarks highlighted. Adapted from Martini *et al*. (2009).

1.3 Anthropomorphic Test Devices

The injury limits previously mentioned are usually developed using experimental impact testing on cadaveric specimens; however, due to the inherent inability to conduct repeated destructive testing, great variability in population, and biohazard considerations, the use of post mortem human subjects (PMHS) is not always practical. For this purpose, surrogates have been developed to evaluate human injury risks. Anthropomorphic test devices are such of the surrogates, and are designed to be biofidelic under specific loading conditions. ATDs are developed to mimic the geometry, mass, mass distribution, kinematics, and kinetics of the human body, and are often instrumented with transducers that quantify the body's response to loading (Carpanen *et al.* 2016). The geometric consistency and their ability to be used multiple times even after being subjected to injurious loads make them practical and consistent tools for evaluating human injury; however, their ability to correlate to actual human response must be quantified before they can be deemed reliable.

1.3.1 Hybrid III 50th Male Leg

The Hybrid III 50th Percentile Male (Humanetics Innovative Solutions, Plymouth, MI, USA) is the most commonly used ATD lower leg for automotive frontal collisions. The mass and geometry of this ATD is based on the 50th percentile male of the USA population between 1970 and 1980 (Carpanen *et al.* 2016). The Hybrid III lower leg consists of a steel shaft that attaches to the knee via an angled clevis with a ball joint that attaches the foot to the shank and approximates ankle range of motion (Figure 1.2a). The angulation of the clevis has been shown to induce artificial moment measurements during axial impacts (Quenneville and Dunning 2012). The Hybrid III leg has instrumentation options that include 6-axis load cells located at the upper and lower tibia, a 5-axis ankle load cell, and a single-axis foot load cell. Load measured at the lower tibia load cell is typically used for injury risk assessment (Carpanen *et al.* 2016), with the threshold for injury is considered to be 5.4 kN measured at this location (Yoganandan *et al.* 1996, North Atlantic Treaty Organization 2011).

1.3.2 MIL-LX Leg

The MIL-LX (Military Lower Extremity) lower leg was designed to be biofidelic under loading conditions that occur during anti-vehicular blast events. The MIL-LX leg features a straight shaft, knee clevis, and ankle, which align the knee pivot, long axis of the tibia, and ankle, thus allowing for optimised measurement of axial force through the tibia (Figure 1.2b) (Humanetics Innovative Solutions 2015a). The shaft contains a compliant rubber element, which is designed to simulate the human cadaveric response to military blast loading (Carpanen *et al.* 2016). This ATD also has a variety of instrumentation options available, including 5-axis upper and lower tibia load cells, a 3-axis tibia accelerometer, and four foot accelerometers. The compliant element is located directly distal to the upper tibia load cell, and as such, the force measured at the upper tibia load cell is used for prediction of risk of leg injuries (Carpanen *et al.* 2016). The threshold for injury has been established as 2.6 kN measured at this upper load cell (North Atlantic Treaty Organization 2011).

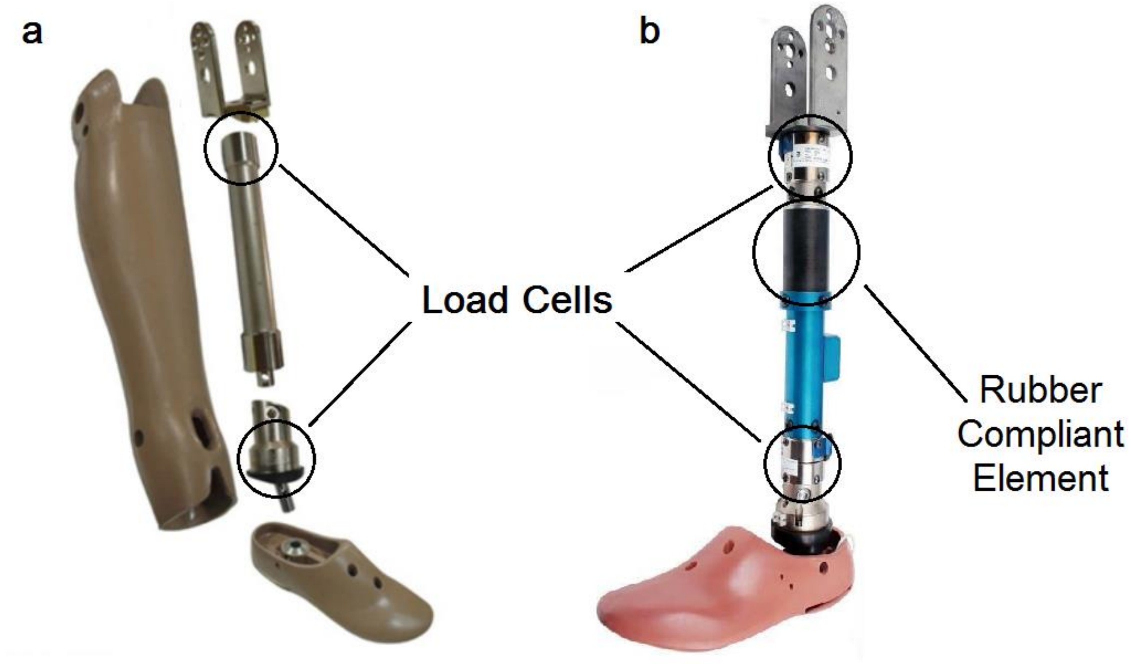

Figure 1.2: Lower Leg ATDs
a) The Hybrid III 50th Percentile Male legform (Humanetics Innovative Solutions 2015b) and **b)** the MIL-LX lower leg (Humanetics Innovative Solutions 2015a) showing the location of load cells implemented into the leg.

1.4 Finite Element Analysis of Bone

While there are numerous studies that have conducted experimental testing to determine the injury tolerance of the lower leg, there are certain limitations to this type of work. Cadaveric testing can be very costly, especially when a number of specimens are required for testing, only few parameters can be tested during destructive impacts, and instrumentation can be challenging. While testing using ATDs is repeatable, the biofidelity of these surrogates is certainly not perfect. Numerical modeling through the use of finite element analysis offers the advantages of being repeatable, cost-effective, and measurements of stress, strain, and displacement can be taken at any point in the model. Finite element analysis is often used as a method of injury assessment in the automotive and defence industries (Sapuan *et al.* 2006).

Finite element analysis is a computerized numerical technique used to approximate solutions to complex problems by diving intricate geometries into smaller, simpler parts, called finite elements. This method is ideal for the mechanical analysis of bone, since it is a structure with such a complex geometry. Finite elements are small shapes joined together at specific points, known as nodes. The total assembly of elements is called the mesh, which is tailored to fit the geometry of the structure being analyzed. The parts in a finite elements model are assigned material properties, and boundary conditions and loads are applied in accordance with the loading conditions being studied.

There are two common types of element shapes that are typically used in FEA, tetrahedral and hexahedrals (Figure 1.3). For dynamic simulations, hexahedral elements

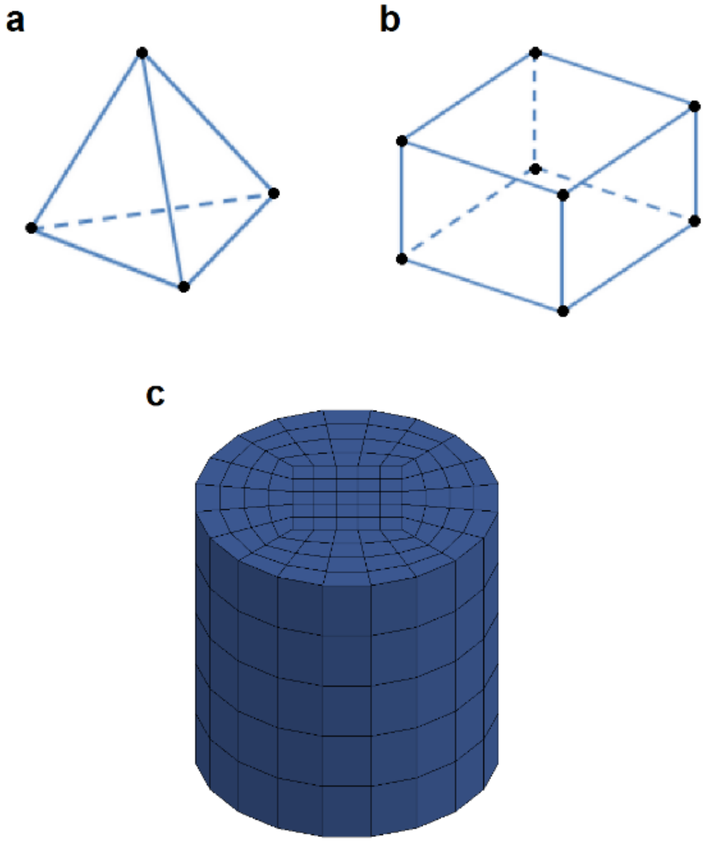

Figure 1.3: Types of Elements
a) Tetrahedral and **b)** hexahedral elements are two common types of elements used in FE modelling, nodes are shown in black. The network of elements and nodes forms the **c)** mesh.

have been shown to be more accurate than tetrahedral elements (Untaroiu *et al.* 2005). Within these types of elements, there are two types of element structures that are frequently used, solid elements and shell elements. Shell elements are less computationally demanding than solid elements, but are only used for parts with very small thicknesses relative to their other dimensions. Solid elements are used much more commonly, when the state of stress is unknown. There are also 1D bar elements that connect two nodes and acts as springs.

Creating the mesh for FEA can be an intensive process, especially when dealing with complex biological structures, such as bone. Non-invasive imaging techniques, such as Computed Tomography (CT), can be used to obtain the geometry and density information of bone. In order to do so, the 3D surface geometry of the bone is extracted from CT images and the mesh is generated based on the surface geometry. The mechanical properties of the material being simulated are assigned to the model prior to application of simulated loads and boundary conditions. Once a model is built, a computer-based solver is then used to analyze the problem. The solver calculates the displacement of each node throughout the simulation and also calculates the state of stress of each element based on the material properties and loads applied.

1.5 Review of Previous Experimental Lower Leg Injury Tolerance Studies

Experimental impact testing is generally used to determine the force levels that cause fracture during axial lower leg loading events. These experiments typically involve using cadaveric subjects as specimens; however, cadaveric specimens are not commonly used in the automotive and defence industries. Instead, these industries use ATDs to evaluate the loads applied to specimens during collisions or blasts. The following studies that have examined the injury tolerance of the lower leg using experimental impacts of cadaveric or ATD specimens are summarized in this section, organized from oldest to newest based on published date.

1.5.1 Cadaveric Axial Impact Studies

The majority of the cadaveric studies investigating the injury tolerance of the lower leg have been conducted with a focus on automotive collisions. Most of these works have used whole lower leg specimens, typically sectioned at the knee or femur, that still contain all soft tissue and the foot and ankle. These impacts most often produce fractures at the talus and calcaneus, while occasionally producing fractures at the distal tibia and fibula. These experiments have used varying instrumentation to quantify the loads in specimens, but have mostly used load cells and accelerometers. These studies typically produced injury risk curves that can be used to evaluate protective systems in vehicles. The key findings from these studies are summarized in Table 1.1 at the end of this section.

Some of the most frequently cited lower leg axial impact works are the studies conducted by Yoganandan *et al.* (1996, 1997) to quantify the biomechanics of the foot-ankle complex under motor vehicle impacts. This study conducted impacts on intact human lower leg cadaveric specimens from males with ages ranging from 27 to 67 years.

The specimens were attached to a mini-sled apparatus that rode along a horizontal rail and bearing system. An impacting pendulum of 24 kg mass was used to impact the plantar aspect of the foot at velocities ranging from 2.2 – 7.6 m/s. The specimens were fixed at the knee and ballasted to 16 kg to ensure a constant mass among all samples. Both an accelerometer and a uniaxial load cell were placed at the pendulum to record input impact conditions, while a load cell was attached to the proximal mounting of the tibia at the mini-sled apparatus to record output forces. Impact forces at the plantar surface of the foot averaged 15.1 ± 2.7 kN for the fracture tests, and were significantly higher than the forces at the proximal end of the tibia, which averaged 10.2 ± 1.5 kN for the fracture tests. Since age was found to be a predictor variable, injury risk curves were developed for specimens of 25, 45, and 65 years of age. The 10% risk of injury for a 45 year old was chosen as the injury tolerance to be used to design protective measures, which corresponded to a 5.4 kN force (North Atlantic Treaty Organization HFM-090 Task Group 25 2007).

Seipel *et al.* (2001) set out to quantify the force tolerance of the calcaneus during frontal automotive crashes. Twenty-two lower extremity cadaveric specimens potted at the proximal tibia were impacted using a pendulum to create a dynamic axial load. The input impact velocities ranged from 2.2 to 6.7 m/s, with energies ranging from 58 to 540 J. Twelve of the 22 specimens tested produced calcaneal fractures, while 10 tests did not cause fracture. Peak fracture forces ranged from 3.6 to 11.4 kN. The probability of calcaneal fracture was determined using a risk curve, showing a 10% probability of fracture at an impact force of 2.5 kN.

One of the first studies to investigate the fracture tolerance of the lower leg during military blasts was conducted by Griffin *et al.* (2001). With the goal of evaluating the protective capabilities of anti-mine protective footwear, full body cadavers were subjected to land mine detonations by placing the heel over a land mine. Loads were measured using load cells attached at the proximal tibia and strain gauges on the distal tibia and calcaneus. The axial loading rate, axial impulse (defined as the area under the force-time curve), weight of the explosive, and peak tibia force were determined to be contributing factors to prediction of pilon fractures. The risk of pilon fractures for the 50th percentile male was plotted over a range of loading rates, including 5, 10, and 20 kN/ms. During loading at a rate of 10 kN/ms, the force associated with a 10% risk of pilon fracture was 2.1 kN. Impacts delivered at greater load rate values resulted in higher force tolerances in the specimens.

Funk *et al.* (2002) investigated the effect of Achilles tension on axial loading tolerance of the foot/ankle complex. Forty-three lower extremity specimens were impacted axially with and without simulated Achilles tension, in order to study its effect. The Achilles tension replicated the active muscle tension that commonly occurs when occupants tense their legs prior to impact. A test apparatus was used to deliver an axial dynamic impact to the plantar surface of the foot at approximately 5 m/s. Active triceps surae muscle tension was replicated by applying tension to the Achilles tendon. Age, gender, body mass, and peak Achilles force were identified as predictor variables of the probability of injury. Assuming no Achilles tension, a 10% risk of fracture in the lower leg corresponded to a force of 5.8 kN for a 45-year-old 50th percentile male. Active muscle tension during impact exerted through the Achilles tendon increased the axial tibial force associated with a 10% risk of fracture by as much as 2 kN.

McKay *et al.* (2009) used lower extremity post mortem human specimens (PMHS) to develop injury criteria for occupants involving short duration axial loads of the lower leg from underbelly blast events. Eighteen specimens were each instrumented with a tibia triaxial load cell at the midshaft and strain gage rosettes were attached to the medial aspect of the calcaneus and to the medial surface of the tibia. The specimens were impacted using a high rate, linear floorplate impactor weighing 36.7 kg. The steel floorplate impacted the plantar surface of the foot, and was allowed to travel 24 mm to mimic floorplate intrusion after impact. The PMHS specimens were divided into three groups, using three incrementally severe loading scenarios (average impact velocities of 7.2, 9.9, and 11.8 m/s and kinetic energies of 941, 1802, and 2494 J, respectively). Each specimen was subjected to a single impact. Twelve of the specimens suffered fractures of the calcaneus, talus, fibula, and/or tibia. Peak axial tibia force and impactor velocity were determined to be the best factors to identify injuries. The survival analysis identified a tibia axial force of 2.4 kN as having a 10% probability of incapacitating injury (Figure 1.4).

While previous experimental studies have used intact lower limbs, Quenneville *et al.* (2011) studied the fracture tolerance of the isolated tibia during short-duration axial loading. Male cadaveric tibias were secured horizontally at the proximal end to a bracket that was free to move on bearings on a horizontal rail, ensuring that the apparatus

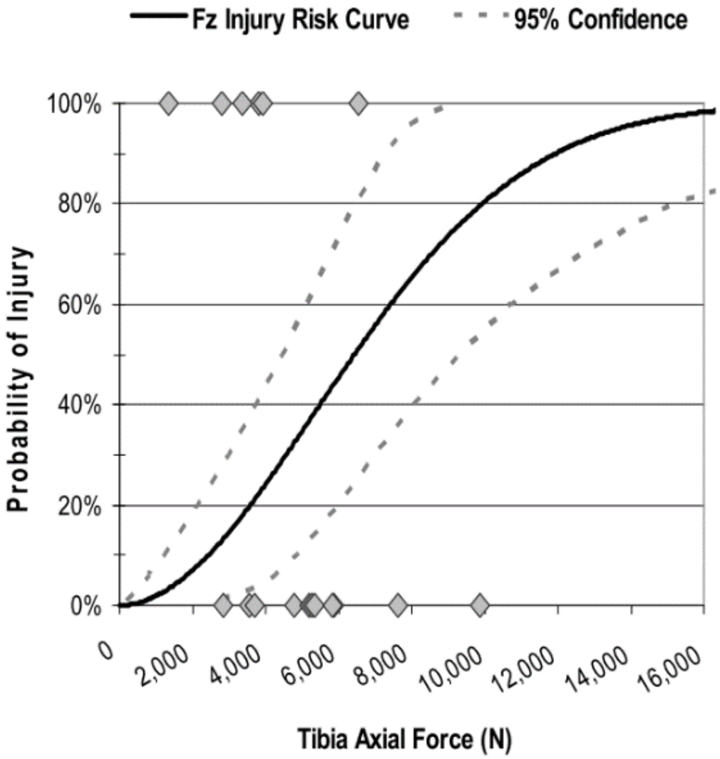

Figure 1.4: Tibia Axial Force Injury Risk Curve, McKay Model
The probability of injury during a military underblast event based on tibia axial force from (McKay and Bir 2009). A 10% risk of injury corresponds to a force of 2.4 kN.

delivered purely axial loading. A light projectile mass of 3.9 kg and a heavy projectile mass of 6.8 kg were used to impact the specimens. Results showed there were no significant differences in fracture forces between the two masses. Kinetic energy was not found to be significantly different between the two masses; however, momentum was. Projectile mass, projectile velocity, momentum, impact kinetic energy, impact duration, impulse, axial force, donor age, donor height, and body mass were the factors used to determine the most appropriate injury equation. A probability relationship was also developed based on impact force, since this is the most common factor measured in the literature, and a 7.9 kN force was found to be associated with a 10% risk of tibial fracture.

The objective of the study by Yoganandan *et al.* (2014) was to develop injury probability curves to define injury tolerance of the human lower leg using data from a previous study (Yoganandan *et al.* 1996) but using a more detailed parametric survival analysis that distinguished between non-injurious tests, injurious tests, and repeated impacts. This involved using peak tibial force as the main variable and age as a co-variable. Similarly to the previous study, an injury probability curve was developed based on the Weibull risk function for the 25-, 45-, and 65-year-old age groups (Figure 1.5). The probability of fracture for a 45-year-old male corresponded to an axial fracture force of 6.8 kN.

The goal of the study conducted by Bailey *et al.* (2015) was to minimize inaccuracies that exist with previous injury risk functions due to inertial effects by considering injury location statistics and loading rate from data collected during previous

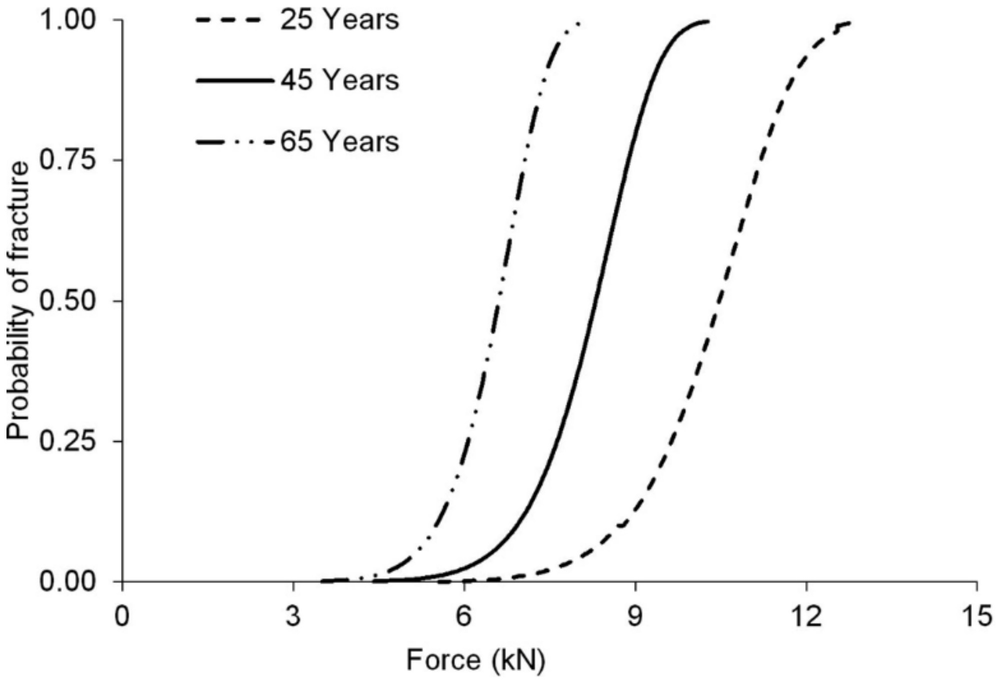

Figure 1.5: Injury Probability Curves, Yoganandan Model
Injury probability curves as a function of age and force from Yoganandan *et al.* (2014). A 10% risk of injury corresponded to an axial tibia force of 6.8 kN for a 45-year-old male.

studies (Yoganandan *et al.* 1996, Klopp *et al.* 1997, Funk *et al.* 2002, Smith *et al.* 2005, Gallenberger *et al.* 2013, Henderson *et al.* 2013). Since calcaneus fractures were seen to be the most often reported in these studies, force measured at the footplate was chosen as the location of analysis due to its proximity to the injurious regions. A survival analysis was conducted to create injury risk functions for the lower leg, which found axial force and dorsiflexion angle to be significant predictors of injury. Their statistical analysis suggested that the results from previous injury criteria are only applicable to the specific loading rates and boundary conditions used in the study. The statistical model from this study predicts a 10% probability of injury for a plantar force of 6.2 kN during axial loading for a 75 kg occupant with a neutral ankle position.

1.5.2 Anthropomorphic Test Device (ATD) Studies

ATDs are commonly used in industry to evaluate a vehicle's safety mechanisms during impacts. The Hybrid III is the most commonly used ATD during frontal automotive collisions. In order to quantify this ATD's ability to predict injury, the Hybrid III lower leg has been tested during axial loading experimentally by comparing to results from established human response corridors. Quenneville *et al.* (2011) found that the forces measured in the Hybrid III lower leg were between 1.8 and 2.8 times as much as those measured during cadaveric testing. Bir *et al.* (2008) also found the forces measured at the Hybrid III's lower tibia load cell were 2.8 times those of PMHS tests during high-rate impacts simulating floor intrusions due to anti-vehicular land mines.

Table 1.1: Summary of Previous Injury Tolerance Studies
The loading scenario replicated through testing, significant factors that contribute to injury prediction, force that corresponds to a 10% probability of injury, and locations of injury are summarized for previous cadaveric lower leg axial impact studies.

Study	Loading Scenario	Significant Injury Risk Factors	10% Injury Risk Force	Injury Locations
Yoganandan *et al.* (1996, 1997)	Automotive	Axial force, age	5.4 kN	Foot/ankle complex
Griffin *et al.* (2001)	Military	Load rate, impulse, axial force, body weight	2.1 kN	Calcaneus, cuboid, navicular, talus, and distal tibia
Seipel *et al.* (2001)	Automotive	Axial force	2.5 kN	Calcaneus
Funk *et al.* (2002)	Automotive	Axial force, gender, age, body weight, Achilles tension	5.8 kN	Foot/ankle complex
McKay and Bir (2009)	Military	Axial force, impactor velocity	2.4 kN	Calcaneus, cuboid, fibula, tibia, talus
Quenneville *et al.* (2011)	Military	Projectile mass, velocity, momentum, kinetic energy, impact duration, impulse, axial force, age, height, body mass	7.9 kN	Distal tibia
Yoganandan *et al.* (2014)	Automotive	Axial force, age	6.8 kN	Foot/ankle complex
Bailey *et al.* (2015)	Both	Axial force, dorsiflexion angle	6.2 kN	-

The MIL-LX lower leg was developed due to concerns with the Hybrid III's stiffness and biofidelity. This surrogate was designed specifically to analyze the effectiveness of land mine protective measures installed in military vehicles. The MIL-LX lower leg has been found to be less stiff than the Hybrid III (Quenneville and Dunning 2012), and has reasonable agreement when compared to cadaveric corridors with respect to peak tibia axial force, loading rate and loading duration (Pandelani *et al.* 2015). The MIL-LX is yet to be adopted by the automotive industry but due to its improvements in geometry and decreased stiffness, the MIL-LX may be an appropriate surrogate for this application. However, the range of investigation that has been conducted to date on the biofidelity is still limited, and there is still a need to conduct impacts over a greater range of loading rates.

1.6 Review of Previous Finite Element Models of the Lower Leg

The majority of the finite elements models of the lower leg have been developed for the purpose of examining automotive and defense applications. These studies involve similar boundary conditions to those investigated in experimental works; however, several simplifications are required due to the complex nature of the geometries and materials under analysis. The methodologies and key findings for these studies are summarized in this section.

Quenneville & Dunning (2011) used FE modelling to simulate loading of the isolated tibia during high-force axial impacts. The mesh for this model includes the cortical bone in the tibia and the components of their experimental configuration, including a bracket at the proximal end of the tibia and an artificial talus, load cell, and impacting bracket at the distal end (Figure 1.6). The mesh geometry was created using a CT scan of a right-sided male tibia specimen from a 49-year-old donor. The material density, elastic modulus, yield stress, and tangent modulus for both cortical and cancellous bone were determined using values from literature. The model response was validated with comparison to results from cadaveric testing (Quenneville *et al.* 2011) where male isolated tibia specimens stripped of all soft tissue were subjected to short-duration axial impacts using a pneumatic impacting apparatus (Quenneville *et al.* 2010).

Shin *et al.* (2012) developed a FE model of the foot and leg to increase the understanding of injury mechanisms during automotive impacts. The geometry of a male close to the anthropometry of the 50th percentile obtained using CT and Magnetic Resonance Imaging (MRI) was used to develop the model. The model included all bones below the knee, skin, flesh, major ankle ligaments, and the Achilles tendon. Since the focus of the model was on the injury response of the ankle region, the tibia, fibula, talus, and calcaneus were modelled as elastoplastic deformable parts, while the metatarsals and phalanges were modelled as rigid bodies. The tibia and fibula were meshed using hexahedral elements in the diaphyseal regions, with shell elements in the epiphyseal regions, while the talus and calcaneus were also meshed using hexahedral meshes. Material properties for the talus and calcaneus were estimated since they are seldom reported in literature, while material properties for the tibia and fibula were obtained from literature. The material properties of the major ankle ligaments were defined in tension

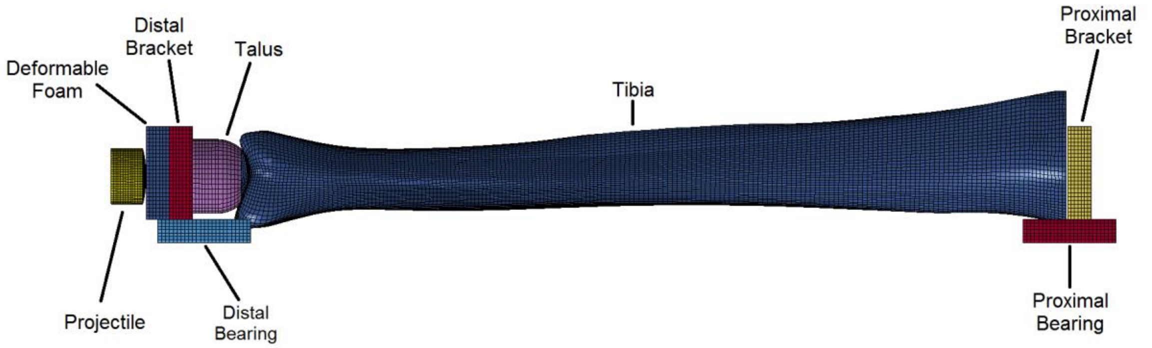

Figure 1.6: Previously Developed Isolated Tibia Model
The isolated tibia model previously developed by Quenneville (2011) formed the basis of the work in this thesis. The model includes the isolated tibia and components of the experimental setup. The model is shown in its horizontal testing orientation.

using values obtained from literature. The model was validated in terms of biomechanical response and injury prediction by comparing to low-energy axial forefoot impact testing of cadaveric human specimens using a pendulum of 1.25 kg mass at a velocity of 6 m/s and also in dorsiflexion, axial rotation, and combined loading. The acceleration time history of an accelerometer placed at the forefoot was used to compare to the model. The model's acceleration values were within the acceleration corridors established experimentally and predicted no injuries, as occurred in testing.

Dong *et al.* (2013) developed a FE model to investigate the effect of blast loading on the lower extremity based on a previously developed and validated full body human model of the 50th percentile male (Belwadi *et al.* 2012). The tibia, fibula, calcaneus, and talus were modelled using linear elastic-plastic material defined using values obtained from literature. To incorporate the strain rate effects on bone's material properties, the Cowper-Symonds formulation was used to model cortical bone in the femur, tibia, calcaneus, and talus. Bone fracture was simulated by deleting elements once they had reached critical tensile stress values. The tibia axial force response was validated by comparing to McKay and Bir's (2009) experimental tests where cadaveric legs were implanted with a triaxial load cell at the midshaft of the tibia and a 36.7 kg impactor was used to impact the leg at 7.2, 9.9, and 11.6 m/s velocities. At the two highest velocities, force time history data were fairly scattered, and as such, corridors could not be developed. At the lowest velocity, the numerical simulation captured the characteristics of the experimental response fairly well both in terms of peak force and impact duration.

The model also accurately predicted fracture locations during loading, which were established experimentally in X-ray images of the cadaveric specimens.

One of the most detailed finite element models of the lower leg during frontal automotive collisions was presented by Untaroiu *et al.* (2013). The geometry for the model was acquired from a male volunteer with anthropometric characteristics close to the 50th percentile male using CT images for the bony structures and MRI for soft tissues. Structures of the lower extremity were modelled, including flesh, bones (femur, tibia, fibula, and patella), knee ligaments (anterior cruciate ligament, posterior cruciate ligament, medial collateral ligament and lateral collateral ligament), knee tendons (femoral and tibial), and menisci (medial and lateral). Hexadral elementts were used to mesh femur and patella due to its efficiency when modelling complex geometries. Shell elements were used to mesh the thin layers of cortical bone in the epiphysis regions to keep simulation time reasonable. LS-DYNA® (Livermore Software Technology Corp., Livermore, CA, USA) was used as the FE solver. The cortical and cancellous bone regions were modeled as isotropic elastic-plastic materials. The model was validated by comparing the results of the FE simulation to experimental tests on PMHS specimens from three-point bending and bending and compression studies. Validation of the tibia involved comparing to a study that subjected 20 PMHS under normal and bending stresses where an axial compression force was applied along the longitudinal axis of the tibia and an impactor loaded the leg at the centre of the distal third of the tibia in the anterior-posterior direction (Untaroiu *et al.* 2008). Results of the model showed that fractures most commonly occurred within the distal third of the tibia, similarly to fracture locations seen clinically.

1.7 Study Rationale and Overview

Most of the cadaveric studies that have investigated the axial fracture tolerance of the lower leg have been conducted with a focus on automotive collisions. In order to design suitable protective measures for these injuries, the fracture tolerance of the lower leg must be well understood. Due to the viscoelastic properties of bone, it remains unclear whether results from lower-rate (automotive) impacts are applicable to higher-rate (blast) scenarios. The majority of these previous studies have also used specimens that include the foot, ankle, and soft tissues. While this configuration may be more realistic, the majority of fractures produced in these studies tend to be in the calcaneus, which is less frequently injured than the tibia in frontal collisions (Taylor *et al.* 1997). The use of whole lower legs also adds a number of degrees of freedom, which may lead to a larger requirement for the number of specimens, and makes alignment more complicated during testing. Axial tolerance thresholds determined in previous studies vary greatly and have been shows to be dependent on the boundary conditions and loading rate used in the specific study (Bailey *et al.* 2015). Therefore, there is still a need to experimentally study the fracture tolerance of the tibia directly over a range of loading rates to determine if the fracture thresholds implemented for the design of automobiles are also applicable in the design of military protective systems.

In order to analyze the effects of an impact on a lower leg specimen, the experimental loads that are delivered to specimens need to be quantified. To do this, a load cell, accelerometers, photoelectric sensors used as velocity sensors, and strain gauges were incorporated into the pneumatic test apparatus in the Injury Biomechanics Laboratory at McMaster University. A program was created that would synchronize the data acquisition across all these sensors and would also trigger the test apparatus and a high-speed camera in the laboratory.

In this work, 12 (six pairs) isolated tibia specimens were subjected to axial impacts in two different conditions. The velocity and duration of the impacts were controlled to match those reported in literature for frontal automotive collisions and military underbody blasts. One specimen from each pair was tested at the lower rate automotive condition, while the contralateral was impacted at the higher-rate military condition. This allowed for a direct analysis and comparison of the injury tolerance of the tibia under these conditions. Isolated tibias were used as specimens to decrease the number of degrees of freedom during testing and to directly investigate the effect of load rate on the fracture tolerance of the tibia with the hope that results from this work could be extrapolated to other bones in the body, mainly the talus and calcaneus.

Two lower leg ATDs (Hybrid III and MIL-LX) were subjected to analogous impact conditions as the cadaveric specimens. Since ATDs are commonly used in industry to evaluate the loads applied to occupants during potentially injurious events, the cadaveric risk equations developed experimentally needed to be transferred into equivalent values for ATDs that can be used by industry.

A previously developed FE model of the isolated tibia was updated to include the experimental configuration used during cadaveric impact testing. The model was subjected to the same impact conditions as the cadaveric testing, and validated against comparing these results. The goal of this model was to provide an accurate and cost-efficient supplementary tool that can be used to determine the risk of injury of the lower leg by industry.

Ultimately, the goal of this work was to determine the fracture tolerance of the tibia over different impact durations. Investigating the effect of temporal impact parameters on tibia injury response will allow for the design of suitable protective systems than can be implemented in vehicles.

1.7.1 Objectives and Hypotheses

The objectives of this thesis were:

1. To design, validate, and implement the instrumentation required to collect impact data during testing using the pneumatic apparatus in the McMaster Injury Biomechanics Laboratory and to create a data acquisition program that was capable of synchronizing the data acquisition and triggering of all external devices.
2. To investigate the effect of impact duration and impulse on the injury tolerance of the tibia under axial dynamic loading through cadaveric impact testing.
3. To assess the biofidelity of the Hybrid III and MIL-LX lower leg ATDs under these loading conditions.

4. To improve and validate a FE model of the tibia that can be used to predict injury under these loading conditions.

The corresponding hypotheses were:

1. Due to the viscoelastic properties of bone, impacts applied to the tibia at varying loading rates have different fracture force limits. Impacts applied at higher loading rates require greater forces than those with lower loading rates.
2. The Hybrid III ATD predicts loads at the distal load cell that are greater than those seen in cadaveric testing, but due to the compressive element in the shaft, the MIL-LX leg produces loads at the proximal load cell that are more closely matched to those seen in cadaveric impact testing.
3. The results from the finite element model are in reasonable agreement with the cadaveric testing in terms of the axial force detected at the distal end of the tibia and critical maximum principal strain and Von Mises stress values.

CHAPTER 2 – INSTRUMENTATION AND DATA ACQUISITION

> ***Overview:*** *This chapter details the development and validation of the instrumentation and software used to collect data for the experimental study found in Chapter 3. Instrumentation was necessary to quantify the impacts that were applied to lower leg specimens using a pneumatic impacting apparatus.*

2.1 Motivation

Numerous studies have quantified the injury tolerance of the lower leg during axial loading events. These works have subjected cadaveric and anthropomorphic test device (ATD) lower leg specimens to axial loads using either pendulum (Yoganandan *et al.* 1996, 1997, Crandall *et al.* 1998, Seipel *et al.* 2001, Funk *et al.* 2002, Gallenberger *et al.* 2013), drop tower (Henderson *et al.* 2013), or pneumatic test devices (Quenneville *et al.* 2010). The impacts that were applied to the specimens in these studies were quantified to analyze their severity, and related to the effects of these impacts on the specimens. This resulted in injury thresholds that rely mostly on the axial force to determine the risk of injury during on impact, but can also use impact variables such as velocity, kinetic energy, loading rate, or impulse. A range of sensors have been implemented into the aforementioned testing devices to quantify these variables, mainly load cells, but have also included strain gauges attached to the specimen (Wang *et al.* 2001, Quenneville *et al.* 2011), velocity sensors to quantify the speed of the impactor (McKay and Bir 2009), or accelerometers attached to the impacting plate (Yoganandan *et al.* 1996, Gallenberger *et al.* 2013).

To conduct impact testing on specimens at the Injury Biomechanics Laboratory at McMaster University, a pneumatic impact apparatus was designed and constructed. This apparatus drives a projectile of variable mass using compressed air stored in a tank to impact a specimen that hangs in a test chamber. This chapter details the development of the instrumentation and data acquisition program to be implemented with this pneumatic test apparatus. This instrumentation was used to quantify the impacts that were applied to lower leg specimens in Chapter 3.

2.1.1 Design Objectives

The objectives in terms of instrumentation and data acquisition were:

1. To implement a load cell, velocity sensor, strain gauges, and accelerometers into the testing configuration used at the Injury Biomechanics Laboratory at McMaster University.
2. To design a fixture to align the uniaxial accelerometer and dual-axis accelerometer to create a tri-axial accelerometer that can be fixed to the irregular geometry and unique surface properties of bone specimens during impact testing.
3. To create a LabVIEW® program that will activate the pneumatic impactor test device, trigger the high-speed camera to begin collecting video, and collect synchronized data from all instrumentation.

2.2 Electronic Components

2.2.1 Pneumatic Impact Apparatus

Impact testing in the Injury Biomechanics Laboratory at McMaster University was conducted using a custom designed pneumatic apparatus (see Chapter 3 for more details of apparatus and testing). Briefly, this apparatus used compressed air stored in a tank to propel a projectile through an acceleration tube to strike specimens. The projectile traveled through an acceleration tube before entering the test chamber where it struck an impact plate and transmitted a load to a lower leg specimen. The air inside the tank was released through a solenoid valve, which required a 5 V signal to trigger the valve opening. The electrical panel that controlled the solenoid valve was connected to the data acquisition system via an analog output module (NI PXIe-6356, National Instruments, Austin, TX, USA) that was programmed to generate this trigger signal.

2.2.2 Load Cell

Axial force is the main variable that has been used as a predictor of injury in lower leg injury studies (*e.g.,* Yoganandan *et al.* 1996, 1997). As such, load cells have been used in all studies to quantify the forces applied to the specimens during impacts. Most load cells used measured forces and moments in three directions. The location of the load cell within the testing configuration varied among studies, as load cells have been placed at the proximal end of the leg (Yoganandan *et al.* 1996, Seipel *et al.* 2001) or between the impactor and the plantar surface of the foot (Funk *et al.* 2002). Load cells placed at the distal end directly quantify the load delivered by the impact, and this has been established as the location for injury prediction using ATD legs by the automotive field (Carpanen *et al.* 2016).

A six-axis femur load cell (IF-625, Humanetics, Plymouth, MI, USA) designed for impact measurement purposes was used to measure the force of the projectile applied to the distal end of the specimen. The load cell was aligned to measure forces in-line with the impact, and had six outputs, corresponding to forces along three axes and moments about three axes. The load cell's six outputs were wired as analog inputs into a terminal block (NI TB 4330, National Instruments, Austin, TX, USA) that interfaced with the data acquisition system (PXIe-1082, National Instruments, Austin, TX, USA) in a full bridge configuration. Relevant parameters were inputted based on a factory calibration report from the supplier.

2.2.3 Accelerometers

Accelerometers are sensors that detect the acceleration of an object relative to freefall (considered as '1 g'). Accelerometers have the benefits of being of relatively low mass, inexpensive, and reusable. Accelerometers are designed and calibrated for specific ranges and are typically available in uniaxial, dual-axis and triaxial configurations. In lower leg axial impact studies, uniaxial accelerometers have historically been attached to the impacting plate to quantify the accelerations experienced during loading (Yoganandan *et al.* 1996, Owen and Lowne 2001, Gallenberger *et al.* 2013) or to calculate the impact plate velocity by integrating the acceleration data (McKay and Bir 2009). Tri-axial accelerometers have also been used (Funk *et al.* 2002), but to date no known lower leg studies have used acceleration as a predictor of injury risk. A previous study that conducted impacts to the upper limb investigated the effectiveness of accelerometers for predicting strains in bone during loading (Burkhart *et al.* 2012). This study glued two accelerometers directly to cadaveric radius specimens, a dual-axis accelerometer at the distal end of the bone where the impacts were applied and a uniaxial accelerometer at the proximal end. Impacts were applied to the specimens using a pneumatic impactor with the bones constrained in the sagittal plane, so accelerations in the medial-lateral plane were deemed negligible and therefore not measured. The data from this study indicated that acceleration was a valid predictor of the probability of bone injury, but the fracture patterns suggested that there may be a significant medial-lateral acceleration that contributed to fracture, even when specimens were constrained in this axis.

Accelerometers were incorporated into the present experimental setup with the objective of quantifying the specimen's acceleration during impact. A uniaxial capacitive accelerometer (MMA1200KEG, Freescale Semiconductor, Ottawa, ON, Canada) was attached to the impact plate to quantify the applied axial acceleration. Another objective was to measure accelerations in all three axes directly on the specimen, at distal and proximal locations. This would require a tri-axial accelerometer that could be attached directly to the bone. Several challenges arose when looking for a suitable accelerometer model, including cost, as most tri-axial accelerometers are very expensive and outside of the budget available for this project, and range as almost all tri-axial accelerometers available on the market are designed for low-acceleration applications, like those used in cellphones. In order to measure accelerations of the specimen in all three axes, two dual-axis and two uniaxial sensors (MMA3202KEG and MMA2202KEG, Freescale Semiconductor, Ottawa, ON, Canada) were chosen to measure orthogonal accelerations at both distal and proximal locations. Table 2.1 lists the accelerometer models used for this study and their locations. The accelerometers used in this work were chosen based on the range of their measurements and low cost. Subjects in military scenarios can experience lower leg axial accelerations up to 100 g during vehicle underbody blasts (Wang *et al.* 2001), so the sensors used in this work were required to be capable of measurements within this range. The accelerometer models selected were all less than $15 each to remain within the budget available for this project.

Since the tri-axial measurement must be taken directly on the specimen, a fixture that could be attached to the bone was created to secure and align both accelerometers. The fixture allowed for the orthogonal alignment of the MMA2202KEG uniaxial and the MMA3202KEG dual-axis accelerometers to create the tri-axial sensing unit (Figure 2.1a). The fixture was constructed using polymethyl methacrylate (PMMA) of 3 mm thickness cut using a laser cutter. The fixture had two faces that were aligned perpendicular to one another to create a 90° angle between the accelerometers. The PMMA faces were fixed together using an acrylic solvent glue and gusset pieces were created to provide support and ensure rigidity of the structure. The accelerometers were attached to the faces using screws. Attaching sensors to bone can be complicated due the irregular curvature of the tibias and their wet surface. To try and make this process more effective, the tri-axial fixture was designed to be as compact and lightweight as possible, while remaining

Table 2.1: Accelerometers Used for Experimental Testing

A uniaxial accelerometer was attached to the impact plate to acquire the acceleration during impact, while a uniaxial and a dual-axis accelerometer were combined and used to capture tri-axial accelerations on the tibia specimens.

Product Code	Number of Sensors Used	Axes	Acceleration Range (g)	Mounting Location
MMA1200KEG	1	Uniaxial (z)	± 250	Impact Plate
MMA2202KEG	2	Uniaxial (x)	± 50	Medial/Lateral Measurement on Specimen
MMA3202KEG	2	Dual axis (x and y)	± 100/50	Axial and Anterior/Posterior Measurement on Specimen

structurally robust. The two faces were constructed perpendicular to one anther in a 'T' arrangement that provided two surfaces to glue to bone and minimized the offset distance from the surface of the bone to ensure the fixture was compact. The dual axis accelerometer was placed to acquire data in the axial (± 100 g) and anterior/posterior directions (± 50 g), while the uniaxial accelerometer acquired data in the medial/lateral direction (± 50 g) (Figure 2.1b). The fixture was glued to each tibia using the same procedure that was used to glue strain gauges to bone (see Appendix B for gluing procedure), as this method was used previously in the literature (Burkhart *et al.* 2012), and zip ties were placed around the fixture and the bone to provide added support. Additional drawings for the accelerometer fixture are included in Appendix C.

All accelerometers required a 5 V power supply (LS25-5, TDK-Lambda Americas Inc., San Diego, CA, USA) connected to a wall outlet. The accelerometers outputs were connected to the data acquisition system based on the recommended circuits from the manufacturer (see Appendix D for circuit diagrams). The output signals from each sensor were connected as analog inputs to the data acquisition module (NI PXIe-6356, National Instruments, Austin, TX, USA).

2.2.3.1 Accelerometer Validation

The accelerometers implemented in this work were calibrated in-factory before being shipped. The datasheets for these sensors stated the typical output signal characteristics that were used to convert the voltage output signal of the sensor to the corresponding acceleration. The datasheets also listed typical minimum and maximum

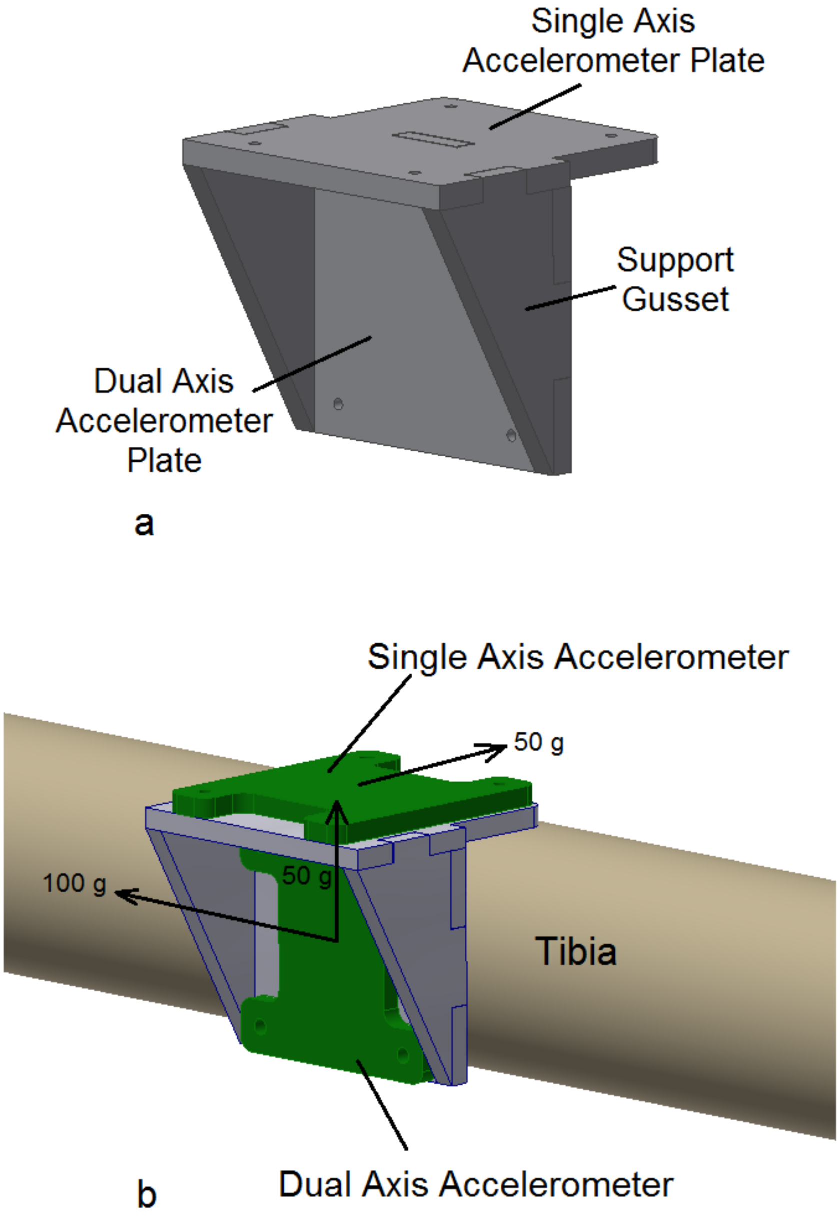

Figure 2.1: Tri-Axial Accelerometer Fixture
a) The alignment fixture created to align the MMA2202KEG uniaxial accelerometer and the MMA 3202KEG dual axis accelerometer to create a tri-axial sensing unit, made of acrylic cut using a laser cutter. The accelerometers were fixed perpendicular to each other to create a 90° alignment. **b)** The accelerometers were attached to the fixture using screws, and the fixture was glued to the bone using the same procedure used to glue strain gauges to bone and zip ties were used for extra support.

output characteristics, which can be used to find the relative error of the sensors. To ensure accuracy of measurements, and since the accelerometers were going to be used in a custom-built alignment system to create a tri-axial accelerometer, it was necessary to validate the output characteristics of all accelerometers. The purpose of this procedure was to validate the typical characteristics listed in the sensor datasheets to ensure that the measured accelerations were accurate. The measured signals were deemed acceptable if they were within the typical 5% relative error listed for the sensors, and therefore the listed characteristics could be used to convert the output voltage to the corresponding acceleration values. If the measured signals did not lie within the relative error of the sensors, this procedure would provide a new calibration and offset for the accelerometer's measurements.

The accelerometer signals were investigated using an ElectroPuls E1000 (Instron® Engineering Corporation, Norwood, MA, USA) materials testing machine. A section of threaded rod was cut and adapted to fit the ElectroPuls E1000 actuator's attachment point. On one end, a hole was drilled and tapped down the centre to accommodate a machine screw (Figure 2.2). The tri-axial accelerometer fixture was attached to the surface of the screw head using cyanoacrylate glue in an orientation parallel to the axis of one of the accelerometers. As such, the outputs from the other two sensors should be negligible. By attaching the entire tri-axial accelerometer fixture, and not just a single accelerometer individually, not only could the accelerations along the axis that is being tested be quantified, but the readings in the other two axes could be evaluated. After testing was

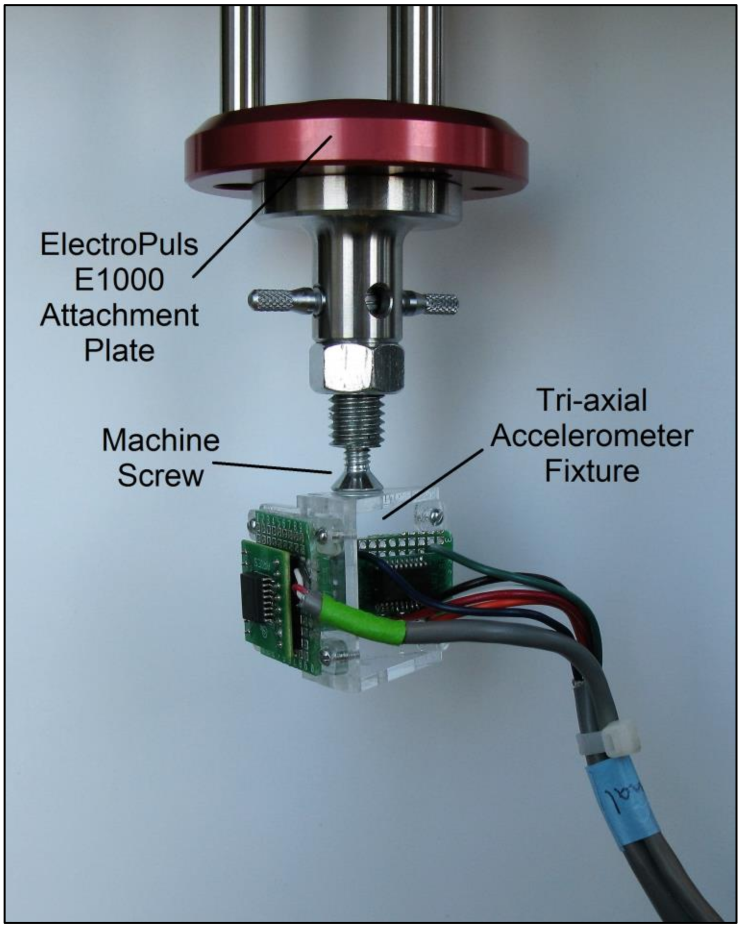

Figure 2.2: Accelerometer Validation Using an Instron® Machine
The tri-axial accelerometer was attached to the Instron® ElectroPuls E1000 materials testing machine. The acceleration measurements were compared to the acceleration of the actuator as it was subjected to a sinusoidal protocol of known acceleration.

completed along one orientation, the tri-axial accelerometer fixture was rotated to a new orientation and tested. This process was repeated until testing had occurred along all three orthogonal axes.

The materials testing machine specifications list a maximum acceleration of 10 g and a maximum velocity of 1.7 m/s. The machine was programmed to oscillate following a sinusoidal wave pattern at a frequency of 10 Hz and an amplitude of 25 mm for a duration of 1 second. The position of the actuator, in metres, with respect to time, *t*, with amplitude A and frequency f could therefore be modelled using the formula for a sinusoidal wave:

$$\begin{aligned} Position &= A\sin(2\pi f t) \\ &= 0.025\sin(2\pi 10 t) \end{aligned} \qquad \textbf{(Eq. 2.1)}$$

Using the amplitude and frequency values specified, the velocity, in metres per second, of the actuator was calculated by differentiating the equation for position:

$$Velocity = 0.5\pi\cos(20\pi t) \qquad \textbf{(Eq. 2.2)}$$

This equation was differentiated once again to calculate the acceleration, measured in m/s^2, of the actuator with respect to time, as given below:

$$Acceleration = -10\pi^2\sin(20\pi t) \qquad \textbf{(Eq. 2.3)}$$

Using this equation, the theoretical maximum acceleration of the actuator under the specified profile was found to be 98.7 m/s^2, or 10.1 g. The peak accelerometer readings were compared to this value to determine the percent error.

The output signals from the accelerometers were collected using a data acquisition system (PXIe-1082, National Instruments, Austin, TX, USA) and custom-written LabVIEW® (National Instruments, Austin, TX, USA) program at a sampling rate of 1 kHz. The accelerometers were zeroed by recording signals while stationary and placed with their measurement axis aligned along the horizontal axis. The maximum measured acceleration was compared to the maximum theoretical value (based on the inputs to the Instron® machine) using the following equation for percent error:

$$\%\,Error = \left|\frac{Measured\,Value - Theoretical\,Value}{Theoretical\,Value}\right| \times 100 \qquad \textbf{(Eq. 2.4)}$$

Table 2.2 shows the calculated percent error values for all accelerometers. For four of the seven accelerometers, percent errors were below 5% and factory calibration values were maintained, while the remaining three produced percent error values between 5 and 10% and as such, the acceleration measurements were calibrated based on the measurements taken during this procedure.

2.2.4 Strain Gauges

Strain gauges are more rarely used in lower leg axial impact studies than load cells and accelerometers; however, their implementation has been proven to be beneficial for a variety of applications. While maximum strain or strain rate is typically not used as a predictor of injury, strain gauges can be used to calculate the compression of the lower limb during impacts and to detect the initiation of skeletal injury (McKay and Bir 2009),

Table 2.2: Accelerometer Errors Obtained During Calibration
The percent error in the values measured in the accelerometers, compared to the 10.1 g theoretical acceleration of the actuator. All accelerometers showed percent errors less than 10%. Four of the accelerometers produced percent errors within the manufacturer's rating of 5%, while 3 produced values greater than this but less than 10%. The blue cells represent the accelerometer models that produced percent errors greater than 5%.

Accelerometer		Max Measured Acceleration (g)	Percent Error (%)
Foot Plate	1200	9.8	-2.1
Distal	3202x	9.2	-8.7
	3202y	10.3	+2.7
	2202	10.2	+1.2
Proximal	3202x	9.4	-6.5
	3202y	9.5	-5.3
	2202	10.2	+1.4

but are even more useful for the development of FE models. Strains are used in FE models to define the material and viscoelastic properties of bone to accurately model the strain rate dependency of bone (Untaroiu *et al.* 2005) or to compare strain values from a model to those measured experimentally (Quenneville and Dunning 2011a). The implementation of strain gauges in experimental studies is of great benefit for the future development of FE models.

Strain gauge rosettes (UFRA-5-350-23-3LT, Tokyo Sokki Kenkyujo, Tokyo, Japan) were used to characterize the strain patterns during impact (see Appendix B for application protocol). The strain gauges were connected to a high-speed bridge input module (NI PXIe-4331, National Instruments, Austin, TX, USA) in a quarter bridge configuration. Since strain gauges are only capable of measuring strain in one direction, strain gauge rosettes have three independent strain gauges positioned at angles to one another. The measurement of strain in three directions allows for the calculation of two plane strains and one shear strain.

2.2.5 Velocity Sensors

Two photoelectric sensors (PZ-V31P, Keyence Corporation, Osaka, Japan) were used to create a velocity sensor. The sensitivity of the photoelectric sensors was adjusted following the manufacturer’s recommendations to output a constant 0 V until an object crosses their field of view (up to a distance of 300 mm), at which point their output becomes 10 V. The sensors were mounted to a plate adjacent to one another to the end of the acceleration tube where the projectile travels before striking the impact plate

(Figure 2.3). The sensors were mounted such that their light-emitting diode (LED) sources were 17.0 mm apart, allowing the difference in time between activation of the first sensor and the second to be used to calculate the velocity of the projectile. A high sampling rate for the data acquisition program of 50 kHz was used to ensure that the sensitivity of the velocity measurements would be adequate at high velocities. At a velocity of 12 m/s, the velocity sensors were calculated to have a sensitivity of 0.2 m/s, while at a velocity of 6 m/s the sensitivity was calculated as 0.05 m/s. The photoelectric sensors were powered using a 24 V power supply (LS35-24, TDK-Lambda Americas Inc., San Diego, CA, USA) (see Appendix D for circuit diagrams). The signals from the photoelectric sensors were connected into an analog input module (NI PXIe-4492, National Instruments, Austin, TX, USA) using BNC connectors. The photoelectric sensors have LED indicators that indicate their current operation status, based on their calibration. When a target has not crossed the sensor's optical axis, the indicator displayed an green light. The indicators switched to an orange LED when a target is in front of the sensor's optical axis and the sensor is in a triggered state.

2.2.6 High Speed Camera

A high-speed camera (IL3-100L, Fastec Imaging, San Diego, CA, USA) was placed directly across from the test chamber to capture slow-motion video footage of all impacts. The camera provided 800 x 600 pixel resolution and recorded footage at rates of up to 1,250 frames per second. The camera's 4 GB image memory meant that videos

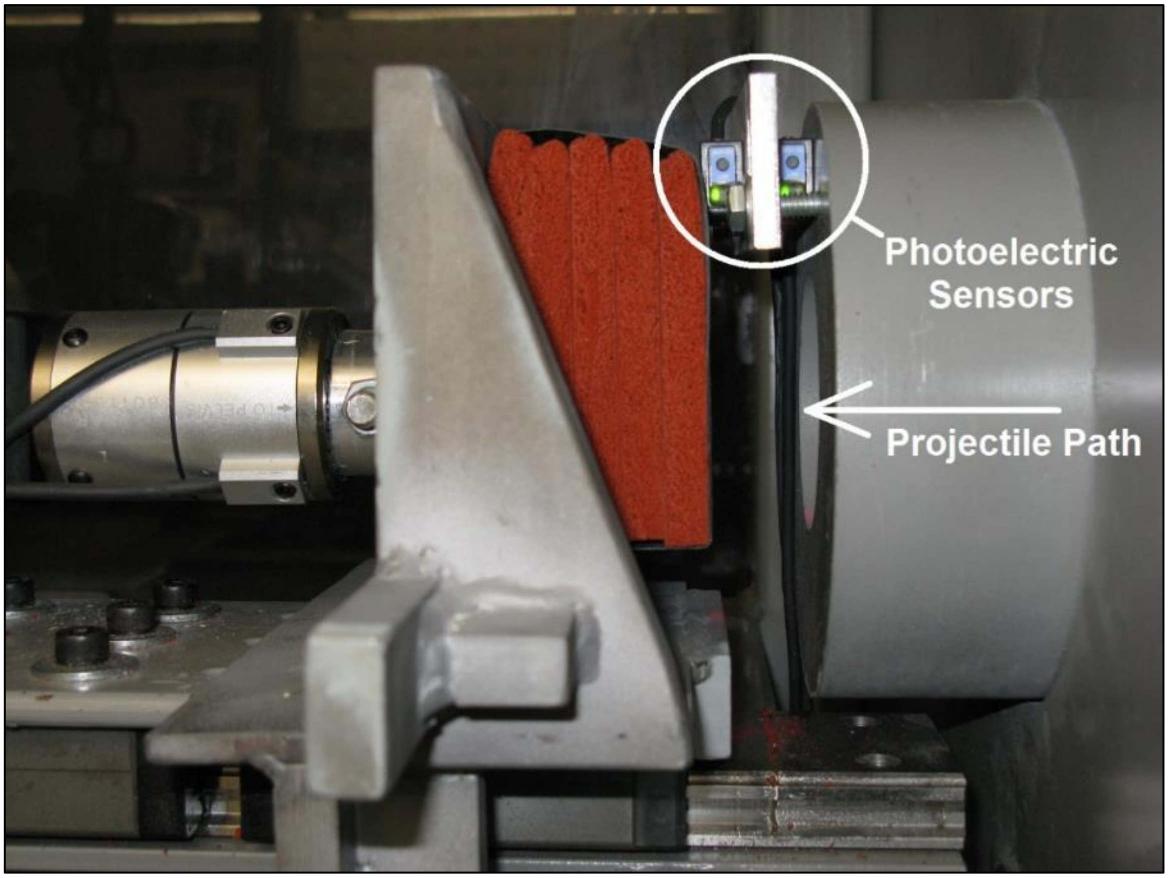

Figure 2.3: Photoelectric Sensors
Two photoelectric sensors were attached adjacent to one another to the end of the acceleration tube. The sensors were calibrated so as the projectile crossed the field of view of the sensors, it triggered their signal prior to striking the deformable sponge. The difference in time between the triggering of the sensors was used to calculate the projectile impact velocity.

were limited to durations of four seconds, which made the synchronization of video recording with the impact and data acquisition even more important. The camera was connected to an analog output channel (NI PXIe-6356, National Instruments, Austin, TX, USA) that was programmed to produce the 3.3 V required to trigger recording using a BNC cable.

2.2.7 Data Acquisition Program

All modules used for data inputs and outputs were connected to a data acquisition system (PXIe-1082, National Instruments, Austin, TX, USA) controlled using LabVIEW® software. A LabVIEW® program was written to synchronize data acquisition across all three modules and trigger the external devices (solenoid valve and high-speed camera) (see Appendix E for LabVIEW® programs). To accomplish this, the program designated the NI PXIe-4492 analog input module as the master device and used the onboard clock from this module to control all data acquisition. The NI PXIe-6356 data acquisition module and NI PXIe-4331 bridge input devices were set as slave devices. Data acquisition was set to collect at a sampling rate of 50 kHz. The sampling rate was verified in the LabVIEW® program using a timing property node that calculates the sampling rate based on the samples written by the program, not the rate specified by the user. The program used the analog output channels on the NI PXIe-6356 module to output the signals required to trigger the solenoid valve and high-speed camera. The program also executed some of the data processing that was required, including calculating the projectile velocity, calculating the maximum axial force, incorporating the accelerometer zero offset values obtained during the accelerometer calibration, and converting the accelerometer signals from volts to acceleration values. All data were displayed in graphs on the front panel and key values including actual sampling rate, projectile velocity, and maximum axial force were displayed using indicators (Figure 2.4). During operation, the user was required to indicate a file path and file name for the data to be saved into spreadsheet format.

2.3 Discussion

This work developed the instrumentation required to operate the pneumatic impact apparatus at McMaster University's Injury Biomechanics Laboratory and to collect the necessary data during the impacts. Due to the dynamic nature of the high-rate loads that the pneumatic apparatus was designed to deliver, data must be acquired at a high sampling rate, and must be synchronized across all sensors for analysis. The electronic system developed acquires data from a load cell, strain gauges, accelerometers, and velocity sensors, high-speed video, while simultaneously triggering the test apparatus.

The modules used to acquire data from the instrumentation have the capacity to expand in terms of the analog inputs that are connected to them if necessary in the future. The NI PXIe-4492 analog input module and NI TB 4330 terminal block have remaining channels that are not in use in the current configuration, so additional load cells, strain gauges, or accelerometers could be added. The LabVIEW® program was created so that the user simply indicates to which channel any new sensor is connected to and the

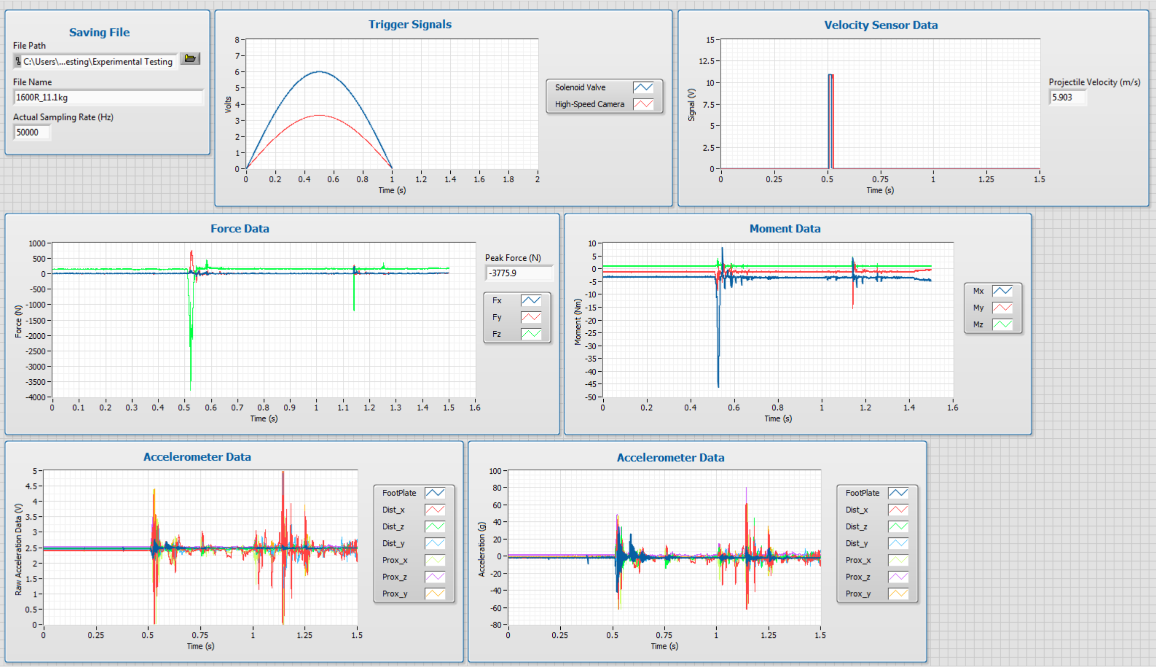

Saving File

File Path: C:\Users\...esting\Experimental Testing

File Name: 1600R_11.1kg

Actual Sampling Rate (Hz): 50000

Projectile Velocity (m/s): 5.903

Peak Force (N): -3775.9

Figure 2.4: LabVIEW® Program Front Panel
The program front panel included locations to enter the file path and file name to save all data into a spreadsheet, and displayed the trigger signals for the apparatus and camera, the projectile velocity, and all force, moment, and accelerometer data.

program will acquire the data. The circuits used to provide the 5 V power for the accelerometers and 24 V power supply to the photoelectric sensors were also left with free connections in case the need to power additional sensors arises.

The accelerometer validation procedure revealed that four of the seven accelerometers produced error values less than the 5% specified by the manufacturer. The remaining accelerometers produced errors greater than 5% but less than 10%. For these sensors, an offset was applied to their measurement by acquiring stationary data that ensured their measurements were within the manufacturer's acceptable error. While the accelerometer validation procedure ensured that accelerometer signals were reliable, there are several limitations with this process that must be acknowledged. The accelerometers were validated by subjecting them to 10 g of acceleration using the materials testing machine; however, during experiments, the accelerometers may be subjected to accelerations much greater than this (up to 250 g for the impact plate accelerometer, greater than 100 g for the specimen accelerometers). The sensors may produce percent errors that are greater than those measured at 10 g, but this was the maximum acceleration that the ElectroPuls E1000 materials testing machine could produce. Another limitation of this method is that the materials testing machine may not have actually produced the 10.1 g acceleration values that it was programmed to create. The apparatus creates a position-time curve during its use, which was subsequently differentiated twice to create an acceleration-time curve. This revealed that the actuator did not reach the peak 10.1 g in all of its oscillations, but only during cycles towards the middle of its run time. Therefore, measurements taken with the accelerometers at midway during the runtime were used to calculate percent errors. Repeated measurements were not taken of all the accelerometers during cyclic loading in the materials testing machine. However, the actuator was programmed to oscillate for several cycles during each test, which produced consistent maximum acceleration readings at its peaks. Finally, the accelerometer measurements were only verified using the maximum acceleration measured during testing with the Instron® machine, as such, the linearity of the measurements or slope of the acceleration curves were not verified.

A velocity sensor was created using two photoelectric sensors to provide projectile velocity measurements. The fact that this velocity sensor was not fully validated must be stated. While the use of the ElectroPulse E1000 to validate their measurements was considered, this apparatus is only capable of a maximum velocity of 1.7 m/s, much less than the velocities that will be produced during impact testing. Instead, the velocity sensor's triggering was corroborated using the high-speed video. In the video, you can identify the moment when the photoelectric sensor is triggered, indicated by a change in colour in its LED. The photoelectric sensors being triggered the moment the projectile crossed their field of view could be verified using the high-speed video captured during testing.

Previous impact studies have developed injury thresholds for the lower leg that are used by the automotive and military industries in their vehicle and protective systems design. The majority of these studies have relied on load cells and accelerometers to collect data during their experiments. The electronic system that was developed in this work is capable of acquiring high-rate load, projectile velocity, strain, acceleration, and video data. Through the acquisition of data from several different sensors, this system can be used to generate more comprehensive injury criteria than have previously been developed. This system's capabilities to be expanded and easily modified also means that it will serve the pneumatic impact apparatus at McMaster University's Injury Biomechanics Laboratory for future studies.

CHAPTER 3 – AXIAL FRACTURE TOLERANCE OF THE TIBIA

Overview: *This chapter details the experimental testing that was conducted to quantify the axial fracture tolerance of the isolated tibia during loading events of various rates. Impact testing was performed using cadaveric specimens to investigate the effects of impact duration and impulse. Additionally, ATD testing was performed to transfer the fracture risk functions that were developed into functional values that can be used by industry.*

3.1 Introduction

Axial impacts to the lower leg, such as during frontal automotive collisions and military under body blasts (UBBs) in combat zones, can cause significant injuries (Ramasamy *et al.* 2011b). Although damage to this region is typically not life threatening, it can result in disability or impairment, which leads to emotional distress to the injured person and decrease in workplace productivity (Owen and Lowne 2001, Dischinger *et al.* 2004, McKay and Bir 2009). In order to reduce these negative outcomes and design suitable protective measures, the injury tolerance of the lower leg must be well understood.

Injuries to this region of the body during frontal automotive collisions and UBBs are caused by an analogous injury mechanism, whereby axial loads are transferred along the long axis of the lower leg due to floor intrusion or interaction with the vehicle's pedals (Figure 3.1) (Gallenberger *et al.* 2013). However, the magnitude of velocity and duration of the impact vary between the two scenarios. Automotive floor pan impacts typically have velocities between 2 and 6 m/s (Crandall *et al.* 1998, McKay and Bir 2009), and impacts lasting between 15 and 45 ms (McKay and Bir 2009). Meanwhile, floor plate velocities during UBBs have been reported to exceed 12 m/s (Wang *et al.* 2001), with load durations less than 10 ms (North Atlantic Treaty Organization HFM-090 Task Group 25 2007). With the introduction of novel protective devices such as energy attenuating floor mats (Quenneville and Dunning 2011b), the durations of these impacts may also vary outside of previously reported ranges.

Previous studies have conducted axial impact tests to determine the injury limits of the cadaveric lower leg (*e.g.*, Quenneville *et al.* 2011, Gallenberger *et al.* 2013, Bailey *et al.* 2015), with the majority of this research being carried out with an automotive focus. These studies suggested a peak axial force between 2.4 kN (Seipel *et al.* 2001) and 7.9 kN (Quenneville *et al.* 2011) is associated with a 10% risk of fracture; however, these force values give little indication of impact duration and correspondingly, impulse. To date, no known study has varied the duration of impact to determine its effect on fracture tolerance. Due to the viscoelastic properties of bone, it remains unclear whether results from automotive experiments can be successfully applied to higher loading rate military blasts. It is possible that varying the duration of loading may have an effect on the risk of injury of the lower leg.

Cadaveric testing is not typically used in industry to determine the risk of injury

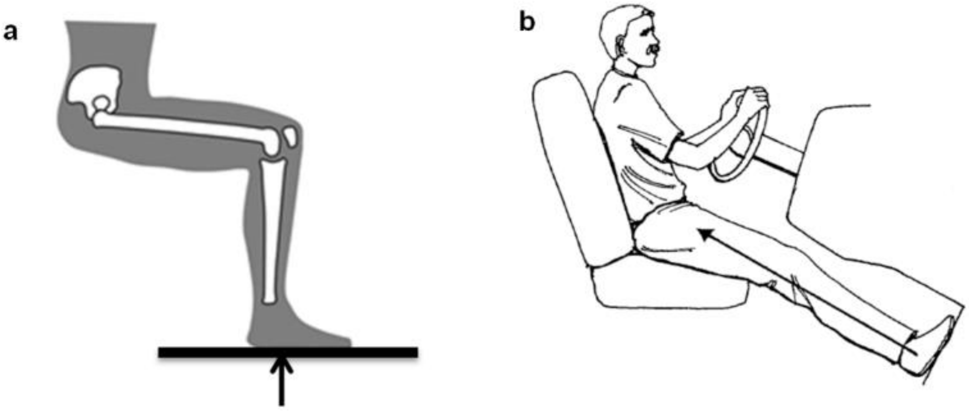

Figure 3.1: Axial Loading Events of the Lower Leg
Impact loading of the lower leg due to **a)** military underbody blast (Quenneville 2016); **b)** contact with the floor pan during a frontal automotive collision (Whiting and Zernicke 1998).

during loading to the human body (*e.g.* in crash testing). Instead, anthropomorphic test devices (ATDs) are placed in vehicles for collision or blast testing to record their response during a simulated impact event. Injury thresholds have been established for each model of ATD, usually load thresholds for a specific implanted load cell, that have been developed through experimental testing and comparison to cadaveric testing. These human surrogates are designed to match the size and mass of a human population, and the Hybrid III 50th Male ATD (Humanetics Innovative Solutions, Plymouth, MI, USA) is currently the most widely used surrogate to evaluate injury during frontal collisions (Humanetics Innovative Solutions 2015b). Despite being originally designed for automotive collisions, the Hybrid III leg has been used to assess injury during military loading (McKay and Bir 2009). Concern over the Hybrid III lower leg's ability to predict injury in higher-rate scenarios led to the development of the MIL-LX lower leg (Humanetics Innovative Solutions, Plymouth, MI, USA), to be used specifically to analyze anti-vehicular land mine protective systems. In order to determine an ATD's ability to predict injury, its response needs to be compared to actual cadaveric human response during loading.

Therefore, the purpose of this study was to investigate the effects of loading rate on the fracture tolerance of the tibia during automotive and military impacts. The injury tolerance established during cadaveric testing was compared to the response of two lower leg ATDs, the Hybrid III and the MIL-LX, to assess their injury prediction abilities.

3.2 Methods

3.2.1 Specimens

Twelve (*i.e.,* six pairs) male fresh-frozen isolated cadaveric tibias (age 62 ± 8 years, no previous history of ankle trauma or surgery) stripped of all soft tissues were obtained for impact testing. Male specimens were chosen to be representative of the military population being studied as one condition in this study. Isolated tibias were chosen to eliminate the number of degrees of freedom associated with the numerous joints and tissues in intact limbs and for the direct investigation of the effect of impact duration and loading rate on bone fracture tolerance, with the hope that observations from this work could be extrapolated to other bones of the body, such as the talus and calcaneus.

The proximal end of each tibia was potted in dental cement to provide a consistent method of support during testing and to ensure proper axial alignment. A custom-designed frame that supported each tibia vertically (proximal end down, in a section of 4" diameter PVC pipe), while allowing adjustment in its alignment in all directions using threaded rods (Figure 3.2) was used for potting. Consistent alignment was ensured using laser levels, with the laser being projected along the anterior ridge of the tibia at mid-shaft in the frontal plane, and aligned with the centre of the medial malleolus in the medial plane. The bone was embedded in cement to the full depth of the PVC pipe (3") and allowed to cure. The PVC pot was then flipped and the void in the cement beneath the

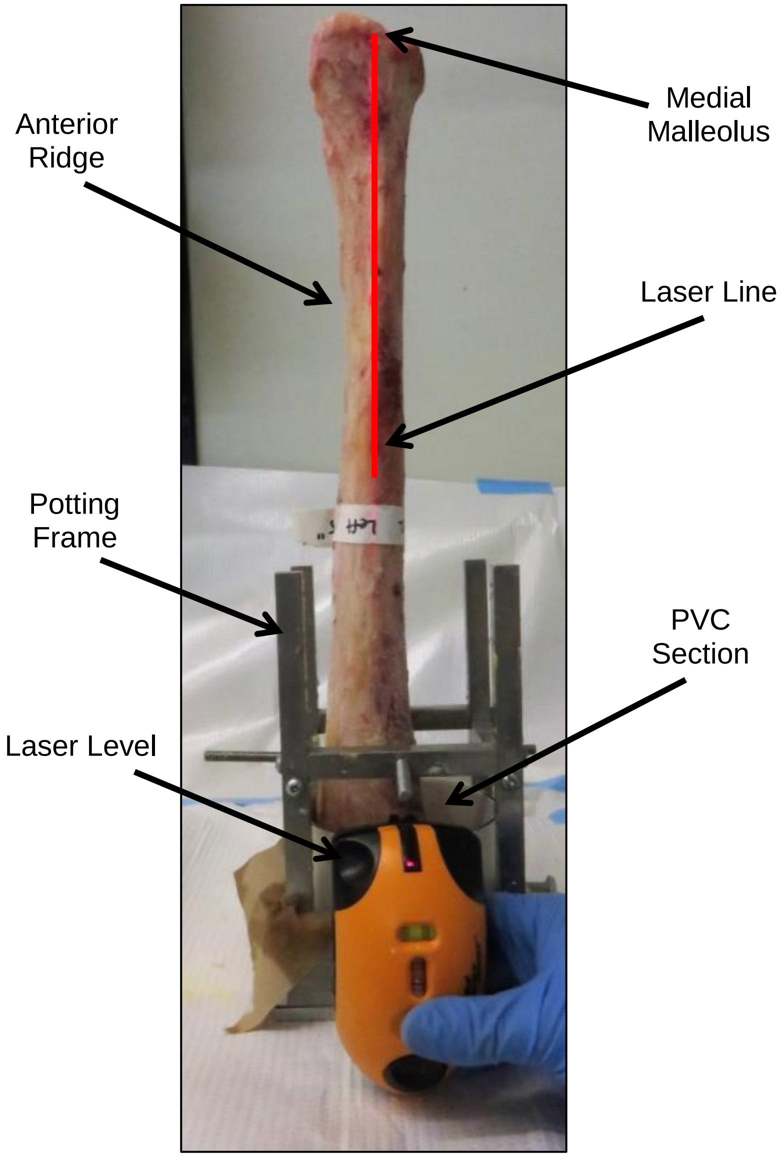

Figure 3.2: Specimen Potting and Alignment
Tibias were supported using the potting frame (proximal end down), and aligned based on anatomical landmarks using a laser level, after which they were embedded in PVC pipe using dental cement. The image shows a medial view of a tibia placed in the potting fixture.

specimen was filled in and levelled with more cement. Each potted specimen was weighed so the required ballast mass could be added to the mounting frame before impact testing to ensure consistent kinematic behaviour across all tests. All specimens were thawed for a minimum of four hours before testing.

3.2.2 Testing Apparatus

Impacts were applied via an apparatus that uses a pneumatic system to propel a projectile of variable mass to impact a specimen placed in a test chamber (Figure 3.3a). The pressure released from the pneumatic tank causes the projectile to travel along an acceleration tube before impacting a specimen via a footplate covered with extra firm density closed cell silicone sponge. The test specimen hung from adjustable chains on a rail and bearing system in the test chamber that allowed the position and angle of the specimen to be easily altered as well as free motion following the impact. The specimen was positioned using a level measured at mid-diaphysis so that the applied load was in line with the long axis of the tibia, producing a primarily axial load. For inertial purposes, ballast mass was added to the frame that holds the specimens to bring the total mass of the specimen and mounting frame to 12.9 kg, which is representative of the mass of the 50th percentile male upper leg, lower leg, and foot (Huston 2009).

Efforts were made to ensure the load from the projectile was applied to the articular surface of the distal tibia specimen in a realistic manner. An artificial talus was created to minimize any stress concentrations when transferring the load (Figure 3.3b).

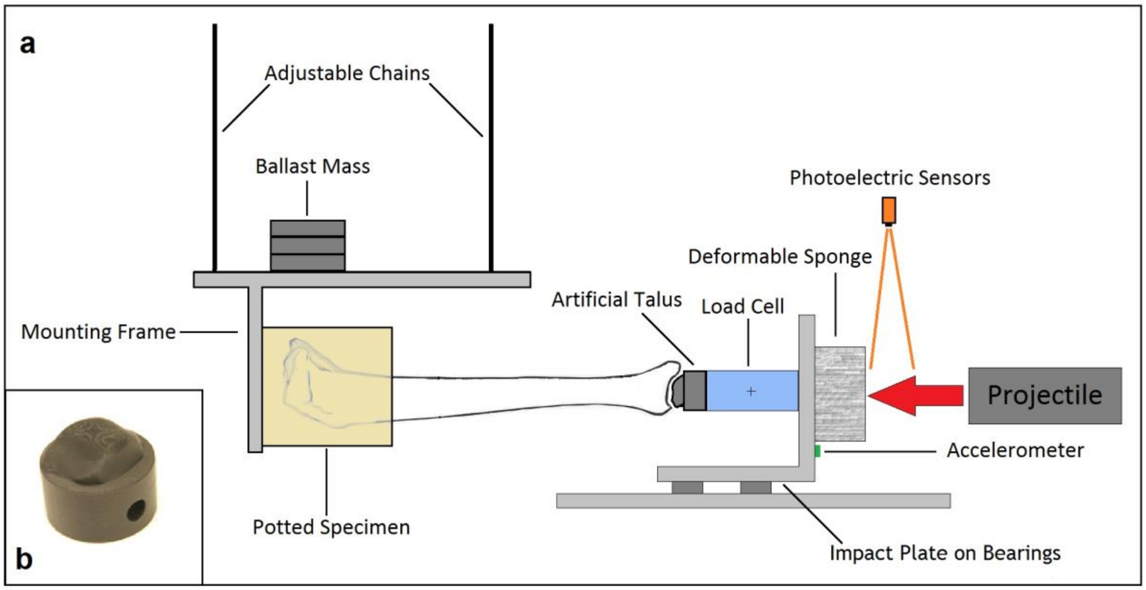

Figure 3.3: Experimental Test Setup
a) Schematic of the experimental setup showing the specimen and instrumentation; **b)** the artificial talus used to transmit the impact loads to the specimen.

The artificial talus was rapid prototyped based on a Computed Tomography (CT) scan taken of a male lower leg, and made of high density acrylonitrile butadiene styrene (ABS) to withstand the loads applied during testing.

The velocity of the projectile was controlled by varying the pressure released by the pneumatic system. A calibration of the testing apparatus was required to determine the input pressures needed to achieve the target impact velocities for the projectile masses that were used for testing. This was conducted by operating the apparatus to impact a potted section of wood, used as a lower leg substitute, placed in the test chamber over a range of input pressures. The results from this testing were used to develop pressure-velocity curves for the apparatus prior to experimental testing (Appendix F).

3.2.3 Instrumentation

Several components of instrumentation were required to quantify the magnitude of the impact and its effects on the specimens during testing. All signals from the instrumentation were collected using a data acquisition system (PXIe-1082, National Instruments, Austin, TX, USA) and custom-written LabVIEW® (National Instruments, Austin, TX, USA) program at a sampling rate of 50 kHz. The development of the instrumentation system was previously detailed in Chapter 2.

A six-axis load cell (IF-625, Humanetics, Plymouth, MI, USA) was used to measure the forces and moments applied to the specimens. The load cell was fastened to the impacting plate, and the artificial talus was attached to the other end, where the load was transferred to the specimen. Two tri-axial strain gauge rosettes (UFRA-5-350-23-

3LT, Tokyo Sokki Kenkyujo, Tokyo, Japan) were glued to each bone specimen to characterize the strain patterns during impact (see Appendix B for application protocol). The rosettes were attached to the anterior surface of the specimen, with one rosette placed at the proximal end of the bone and another at the distal end. The proximal rosette was located 5 cm from the surface of the cement at the proximal end of the potted sample, to ensure sufficient distance from areas of stress concentrations. The distal strain rosette was placed 3 cm from the tibial plafond of the bone specimen. The centre gauge of each rosette was aligned with a laser from potting. A uniaxial accelerometer (MMA1200KEG, Freescale Semiconductor, Ottawa, ON, Canada) with a range of ± 250 g was attached to the impact plate to quantify the input acceleration. A dual-axis and a uniaxial accelerometer (MMA3202KEG and MMA2202KEG, Freescale Semiconductor, Ottawa, ON, Canada) were mounted to an alignment fixture to create a triaxial acceleration measurement system (see Chapter 2 for triaxial mount development). Two of these alignment fixtures were attached to the tibia specimen, on the posterior surface of the bone at locations along the length of the bone that corresponded with the strain gauge rosettes' location. The velocity of the projectile was calculated using two photoelectric sensors (PZ-V31P, Keyence Corporation, Osaka, Japan) mounted to the end of the acceleration tube adjacent to one other.

3.2.4 Cadaveric Test Protocol

Two different experimental conditions were simulated in the impact testing of isolated tibias: a higher-rate military underbody blast and a lower-rate automotive crash.

The UBB condition had a target velocity of 12 m/s (Wang, 2001) and a target impact duration of 5 ms (North Atlantic Treaty Organization HFM-090 Task Group 25 2007). The testing condition representative of a frontal automotive crash was constrained to target a lower velocity of 6 m/s (McKay and Bir 2009) but longer impact duration of 20 ms (North Atlantic Treaty Organization HFM-090 Task Group 25 2007). One specimen from each pair was tested at the lower-rate condition, while the contralateral was impacted at the higher-rate condition, with right-left selection randomized. In order to keep the velocity and duration values constant throughout the trials, mass was added to the projectile to increase the intensity level of each successive impact until fracture occurred, defined as the distal end of the tibia being separated into at least two distinct sections. The duration of the impact was controlled using silicone sponge attached to the impact plate on the projectile side of the plate. An iterative approach was used to determine the sponge thicknesses required to achieve the required impact durations. Larger thicknesses of silicone sponge were found to extend the duration of the impacts, and a thickness of 50 mm was chosen to control the duration of the impacts in both testing conditions. Due to the different velocities and projectile masses of the two testing conditions, the thickness of the sponge required to achieve the target impact duration was the same for both conditions. The silicone sponge material was chosen to regulate the duration of the impact due to its firm density and ability to withstand multiple impacts without visible damage. The sponge was replaced after testing was completed for four specimens to minimize any accumulated damage. To minimize any cumulative damage to the specimen, two impacts were targeted for each specimen, an initial non-fracture test followed by a fracture test. The pre-fracture test was used to provide information on the load response of the specimen, while the fracture test allowed more precise identification of the injury threshold.

A best subset regression analysis was performed on data collected during the impact tests to identify the factors that contribute to injury risk. Donor age, projectile mass, projectile velocity, impact force, impact duration, projectile kinetic energy, projectile momentum, impact impulse (defined as the integral of the force-time curve), and load rate were considered, with the response set to 1 for fracture tests and 0 for non-fracture tests. Paired t-tests ($\alpha = 0.05$) were used to determine whether there was a statistically significant difference between the two test conditions for the aforementioned factors. A Weibull analysis was used to develop probability of injury curves based on the best subset of fracture predictors, as well as for peak axial force.

3.2.5 ATD Test Protocol

In order to compare the fracture tolerances obtained from cadaveric testing to values that can be functionally used in industry, both the Hybrid III and the MIL-LX 50th percentile male legforms were tested. The goal of this testing was to compare the forces measured by the ATDs internal load cells under similar impact conditions to the cadaveric results. These loads were used to determine appropriate injury thresholds under loading of various rates.

The Hybrid III and MIL-LX ATDs’ lower leg portions (knee clevis to ankle joint) were subjected to similar testing conditions as the cadaveric specimens. These included a lower rate condition simulating an automotive frontal collision and a condition with higher load rate simulating a military underbody blast. As was done for the isolated tibia testing, target velocities were set for each test condition and impact severity was raised by increasing the mass of the projectile. For the lower-rate condition, impacts that had velocities of 6 ± 0.5 m/s were accepted, and for the higher-rate condition velocities of 11.5 ± 0.5 m/s were accepted. The same thickness of sponge that was used during cadaveric testing was attached to the impact plate, to ensure that the impact conditions were analogous. Due to the higher stiffness of the ATDs when compared to bone (Quenneville and Dunning 2012), the masses that were used for ATD testing were less than cadaveric testing to ensure that the 11.1 kN limits of the load cells were not exceeded. The ballast mass was adjusted to maintain the total mass of the specimen and components at 12.9 ± 0.3 kg. The ATD legs were placed in the impacting apparatus and aligned using a level so the tibia was in line with the impact, producing a primarily axial load.

For each mass that was tested, five impacts were performed to assess repeatability and the forces measured were averaged. Force-mass curves were produced for each legform under each of the test conditions. The force measured at the distal load cell was used for analysis for the Hybrid III leg since this is where the current injury limits are measured according to industry standards (Carpanen *et al.* 2016). Due to the location of the compliant element, the MIL-LX leg uses the force measurement taken at the upper tibia load cell for predictions of risk of leg injuries (Carpanen *et al.* 2016), so the proximal load cell was used in the assessment of the MIL-LX. A Weibull analysis was completed for the cadaveric testing based on the fracture masses for each test condition to determine the mass that represents a 10% risk of fracture in each condition. The force-mass curves created for each ATD were then used to determine the force to which this 10% fracture mass corresponded, based on linear extrapolation due to the different range of masses that were used for cadaveric testing compared to ATD testing. This allowed for the comparison of risk of injury from values determined from cadaveric testing to values from ATD testing.

3.3 Results

3.3.1 Cadaveric Testing

There were issues that occurred with the instrumentation during experimental testing. Due to the natural curvature of bone, the triaxial accelerometer fixture proved to be extremely challenging to attach to bone, and would often fall during an impact. Also, in the process of handling the specimens to prepare them for testing, several of the strain gauge wires were detached. As such, acceleration and strain data was not collected for all impacts, and this data were not used in the data analysis.

In each test, intra-articular damage occurred at the distal end of the tibia (Figure 3.4). It took an average of 4.2 (± 1.8) impacts to achieve fracture in all specimens, 4.6 ± 2.1 impacts for the lower rate test condition and 3.7 ± 1.8 impacts for the higher-rate condition, which was not significantly different (p = 0.704). The higher-rate tests had an

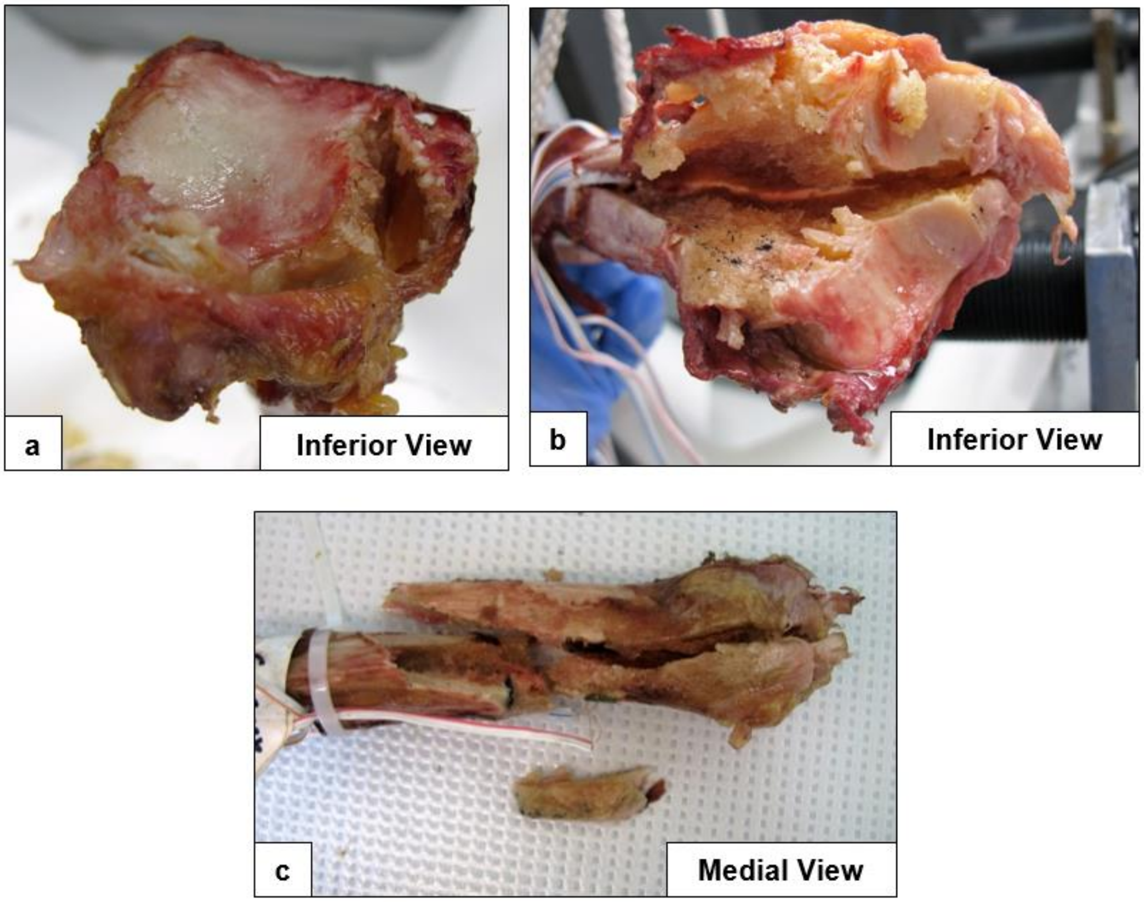

Figure 3.4: Typical Specimen Fracture Patterns
Fractures occurred at the distal end of the tibia for all specimens. Specimens **a)** 1536R, **b)** 1541R, and **c)** 1567R are shown.

average velocity of 11.4 (± 0.7) m/s and average impact duration of 6.2 (± 1.1) ms, compared to a velocity of 5.7 (± 0.5) m/s and impact duration of 18.5 (± 6.0) ms for the lower-rate condition. Figure 3.5 shows the fracture force-time curves for a representative donor for both the lower-rate and higher-rate conditions. The higher-rate test condition consistently achieved larger peak force values than the lower rate test condition, but the impact duration was much shorter. Even though the peak force was less for the lower rate condition, the impulse values were greater as a result of the longer impact duration.

For some of the specimens (3 of 12), the greatest force and impulse occurred at the second-last impact, prior to the impact that caused fracture, while the greatest projectile mass and kinetic energy occurred during the final fracture tests. Therefore, peak values for each factor did not correspond to the same impact in all specimens; however, for statistical analysis the peak value from any test was used, since the peak value for each factor should best represent the specimen's maximum injury tolerance. Detailed information regarding the impact data for both the second-last pre-fracture impact (for those specimens that had higher force and impulse values in these impacts) and final fracture impacts is included in Appendix G. Forces in the mediolateral (average 0.6 ± 0.3 kN, range 0.2 – 1.0 kN) and anteroposterior (2.3 ± 1.5 kN, range 0.3 – 5.3 kN) directions were considerably lower than the axial direction and were not used for injury analysis.

Based on the value of the adjusted R-squared from the best subsets regression analysis, the best model for predicting fracture included projectile velocity, kinetic energy, impulse, and loading rate (adjusted $R^2 = 30.3$) (Eq. 3.1). The peak values for all

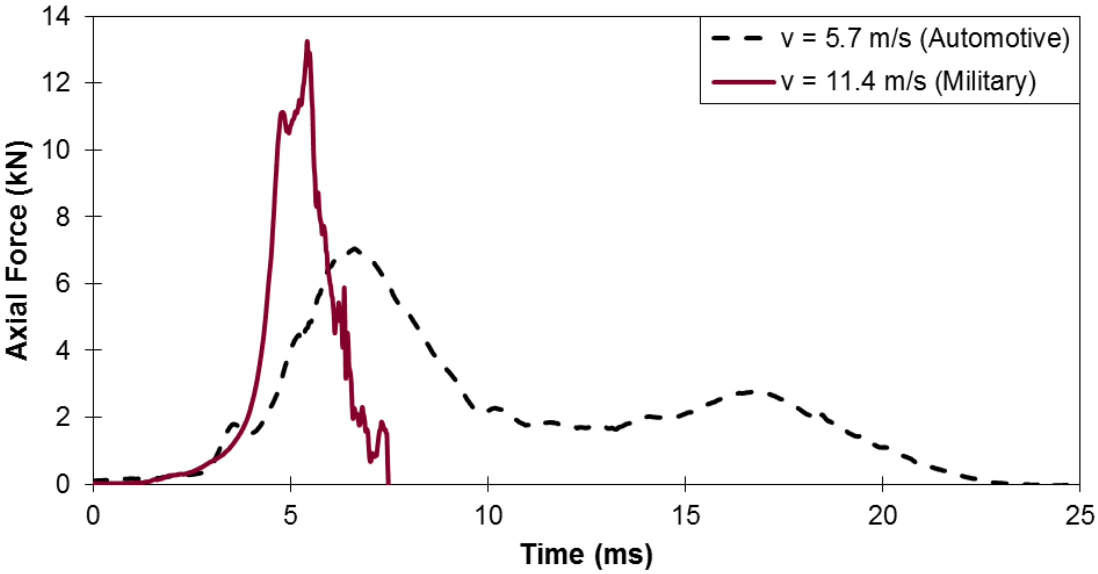

Figure 3.5: Representative Fracture Force-Time Curves for Both Test Conditions
The higher-rate military condition had a larger peak force but shorter duration (13.5 kN, 6.2 ms) than the lower-rate condition (10.9 kN, 18.5 ms). Impulse was calculated as the integral of each force-time curve. Impulse for the higher-rate condition was 30.3 Ns, compared to 57.1 Ns for the lower-rate condition.

factors found to be significant are shown in Table 3.1 for both test conditions. The model to predict fracture from the linear regression analysis was:

$$\begin{aligned} Fracture\ Risk = 1.139 - 0.0848 \cdot V + 0.000981 \cdot KE \\ -0.02219 \cdot I + 0.0566 \cdot R \end{aligned} \qquad \textbf{(Eq. 3.1)}$$

Where *V* is the velocity of the projectile (in metres per second), KE is the kinetic energy of the projectile (in joules), *I* is the impulse (in newton seconds), and R is the loading rate (in kilonewtons per millisecond).

There was a statistically significant difference in peak force (p = 0.023) (Figure 3.6), impulse (p = 0.009) (Figure 3.7), and load rate (p = 0.025) (Figure 3.8) between the lower-rate and higher-rate test conditions, but not kinetic energy (p = 0.785) (Figure 3.9).

A probability of fracture curve was developed using a Weibull analysis based on the risk equation (Figure 3.10). Force is typically used as the main factor for predicting injury (Yoganandan *et al.* 1996, 1997, 2014, Kuppa *et al.* 2001, Funk *et al.* 2002, McKay and Bir 2009, Quenneville *et al.* 2011, Gallenberger *et al.* 2013, Bailey *et al.* 2015); therefore, a second Weibull analysis was performed to develop an injury risk curve based on axial force only for comparison purposes (Figure 3.11). This indicated that a 10% chance of fracture corresponded to an axial load of 9.0 kN for the lower-rate condition and 12.2 kN for the higher-rate condition. Previous injury risk equations based on axial force were graphed along with the newly developed injury risk curves in this work for comparison (Figure 3.12).

Table 3.1: Specimen Fracture Information
Results for both the **a)** lower-rate impact condition and **b)** higher-rate condition showing peak values for each factor that were used for statistical analysis. The values for projectile mass, kinetic energy, and loading rate corresponded to the fracture impact, while force and impulse corresponded to the impact (pre-fracture or fracture) that achieved peak forces. Detailed specimen information (age, potted mass, length) is provided in Appendix H.

a)	**Lower-Rate (Automotive) Impact Condition**				
Specimen	**Projectile Mass (kg)**	**Force (kN)**	**Kinetic Energy (J)**	**Impulse (Ns)**	**Load Rate (kN/ms)**
1494R	31.6	10.6	435	53.8	2.3
1536R	31.6	10.8	442	57.1	1.2
1538L	21.0	9.1	449	26.1	1.3
1541L	34.6	12.8	603	62.7	2.5
1567L	34.6	11.3	666	45.0	2.3
1600R	21.0	11.0	564	48.4	3.7
Average (±S.D.)	29.1 (6.4)	10.9 (1.2)	526 (98.2)	48.9 (12.8)	2.2 (0.9)

b)	**Higher-Rate (Military) Blast Condition**				
Specimen	**Projectile Mass (kg)**	**Force (kN)**	**Kinetic Energy (J)**	**Impulse (Ns)**	**Load Rate (kN/ms)**
1494L	6.9	13.3	443	22.1	4.6
1536L	8.3	14.3	594	30.3	9.2
1538R	8.3	13.5	533	27.3	4.7
1541R	6.5	11.8	429	27.3	3.7
1567R	6.9	13.3	443	27.3	6.2
1600L	7.6	14.5	612	25.9	4.8
Average (±S.D.)	7.4 (0.8)	13.5 (1.0)	509 (82)	26.7 (2.7)	5.5 (2.0)

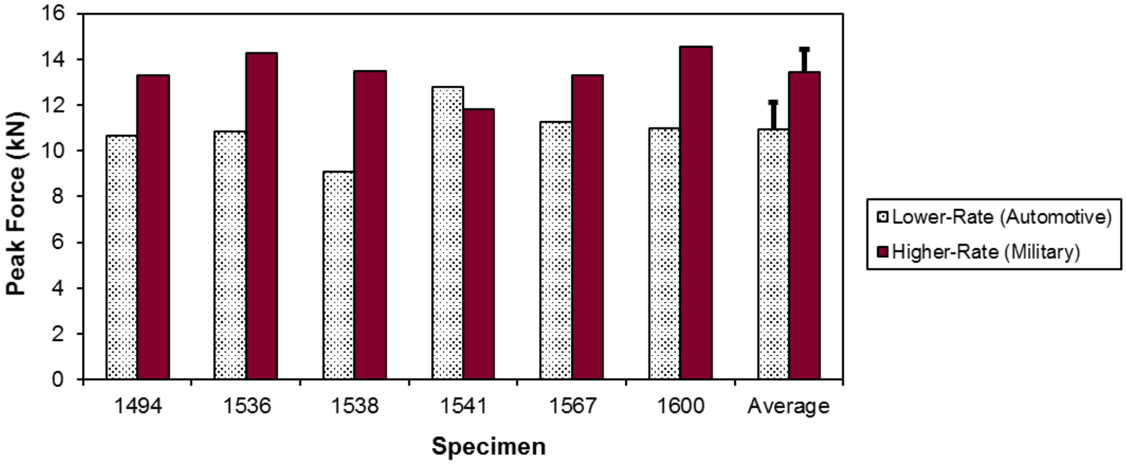

Figure 3.6: Peak Axial Force
The peak axial force was significantly lower in the lower-rate case. The peak force values were averaged across all specimens and standard deviations are shown with error bars.

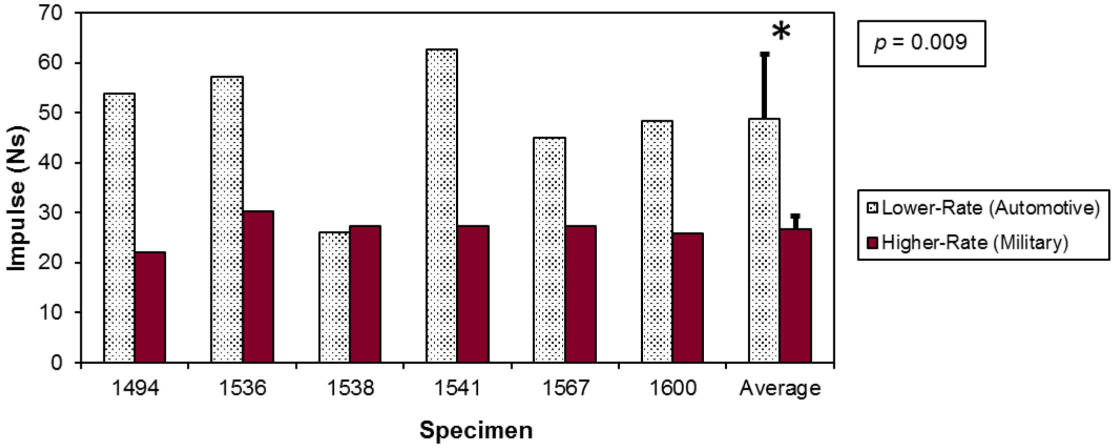

Figure 3.7: Peak Impulse
While the lower-rate case had lower peak force values, the longer impact durations in this case resulted in the peak impulse values being significantly lower for the higher-rate test condition**.**

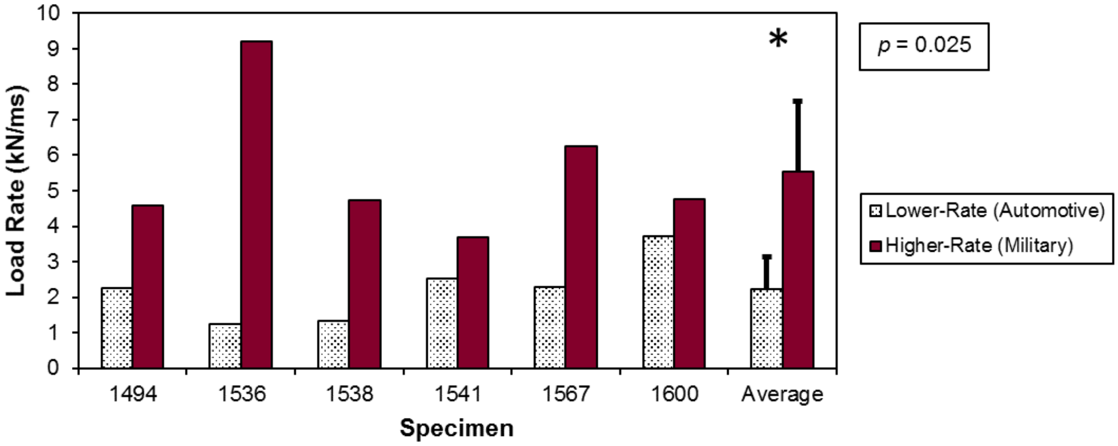

Figure 3.8: Peak Load Rate
Peak loading rates were averaged for all specimens. Due to the higher axial forces and shorter impact durations, the peak load rate values were significantly greater for the condition simulating a military blast.

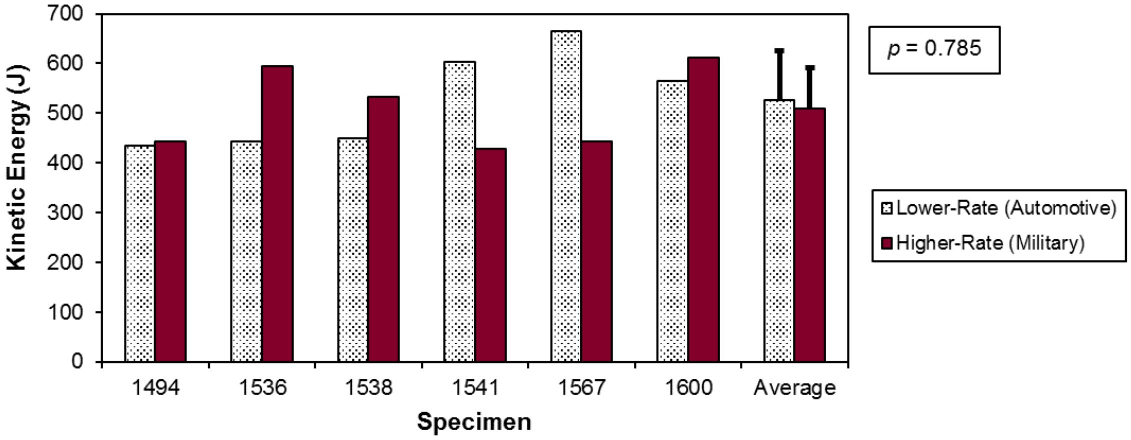

Figure 3.9: Peak Kinetic Energy
The kinetic energy of the projectile was calculated for all specimens. There was no significant difference found in the peak kinetic energy required between the two test conditions.

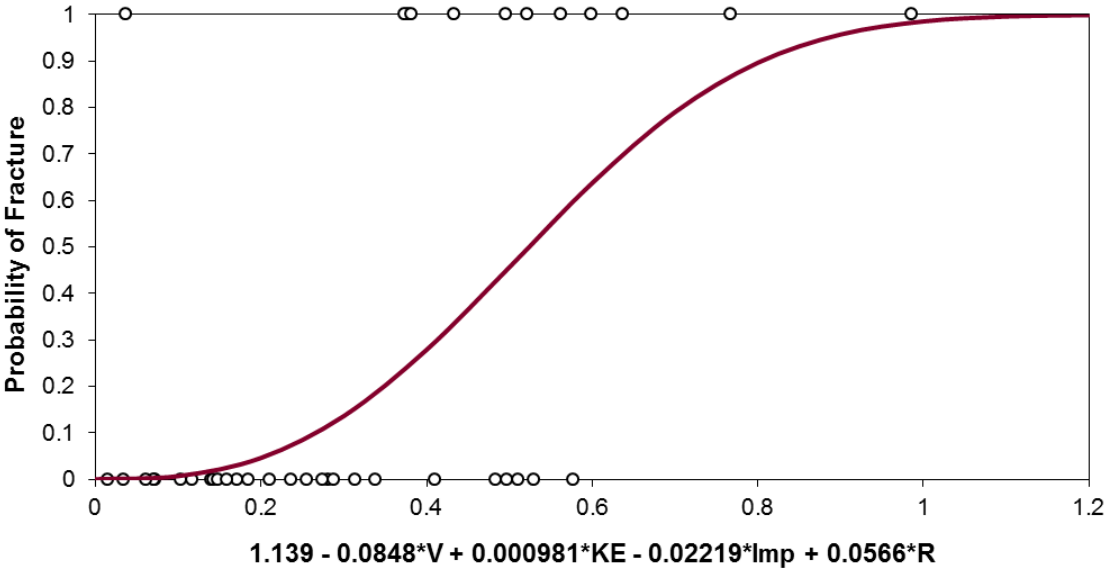

Figure 3.10: Probability Distribution for Fracture
Probability of fracture as a linear function of the impact velocity (*V*) (in metres per second), kinetic energy (*KE*) (in joules), impulse (*Imp*) (in newton seconds), and load rate (*R*) (in kilonewtons per millisecond). A probability of fracture of 0 indicates no risk, while a value of 1 indicates guaranteed risk. The points represent the impact data obtained from testing.

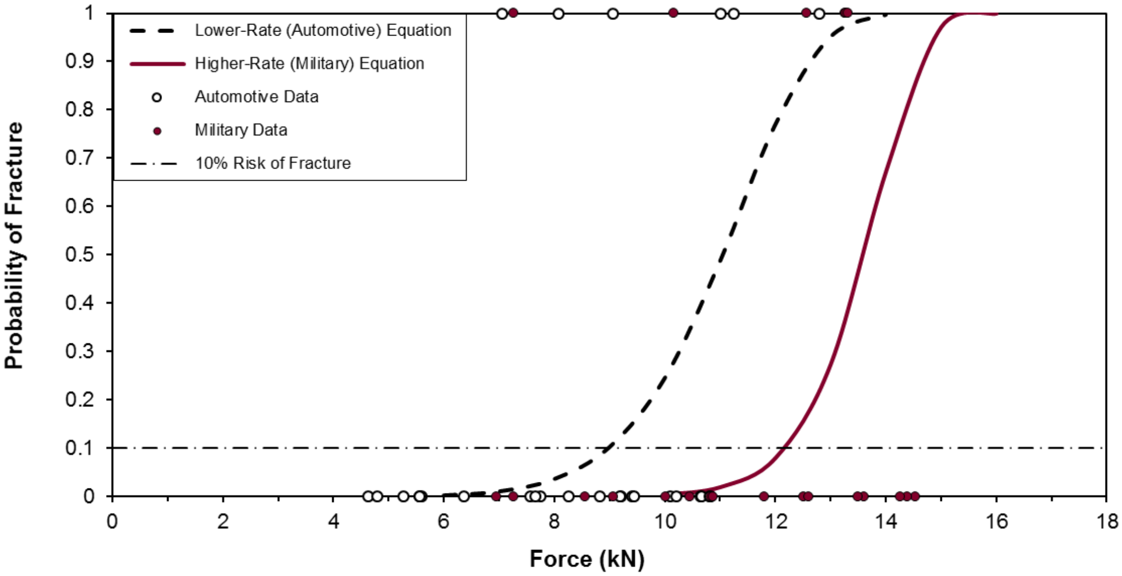

Figure 3.11: Probability Distribution for Fracture Based on Axial Force
Separate equations were developed for each test condition, since the axial force required for fracture was found to be significantly different between the two. A 10% risk of injury line is also shown. The points represent the impact data.

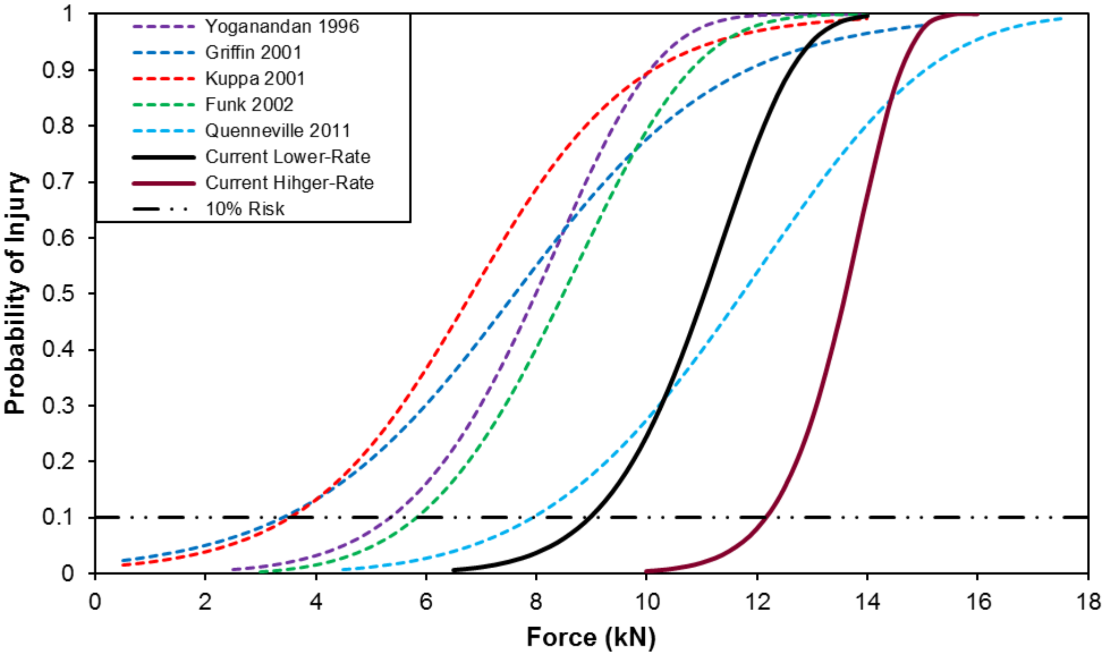

Figure 3.12: Comparison of Injury Risk Equations
The current injury probability curves developed for the lower-rate and higher-rate test conditions are shown, along with injury probability curves from previous studies and a 10% risk of injury line.

3.3.2 ATD Testing

Average velocities for ATD testing were 6.0 (± 0.2) m/s for the lower-rate automotive condition and 11.4 (± 0.1) m/s for the higher-rate military condition. Only the MIL-LX leg was tested at the higher velocity military condition since this condition produced forces beyond the capacity of the Hybrid III leg's load cell. Therefore, three force-mass curves were produced for analysis: the Hybrid III and the MIL-LX legs under the lower-rate test condition, and only for the MIL-LX in the higher-rate military test condition (Figure 3.13). Linear regression analysis was used to estimate the relationship between mass and force measured by the ATDs. The force-mass curves for the ATDs exhibited high coefficients of determination ($R^2 = 0.96$ for the Hybrid III leg in the lower-rate condition; $R^2 = 0.95$ and $R^2 = 0.99$ for the MIL-LX leg in the lower-rate and higher-rate conditions, respectively). The Weibull analysis based on impact masses from the cadaveric testing revealed that a 15.5 kg mass and a 5.8 kg mass corresponds to a 10% risk of fracture for the lower-rate and higher-rate conditions, respectively. For the lower-rate condition, this 15.5 kg limit would have resulted in a load of 19.9 kN measured with the Hybrid III leg and 2.8 kN measured with the MIL-LX, based on a linear extrapolation based on the force-mass curves. For the higher-rate condition, the 5.8 kg limit would have caused loads of 3.1 kN to be measured with the MIL-LX leg, again, based on linear extrapolation based on the force-mass curve for the MIL-LX leg.

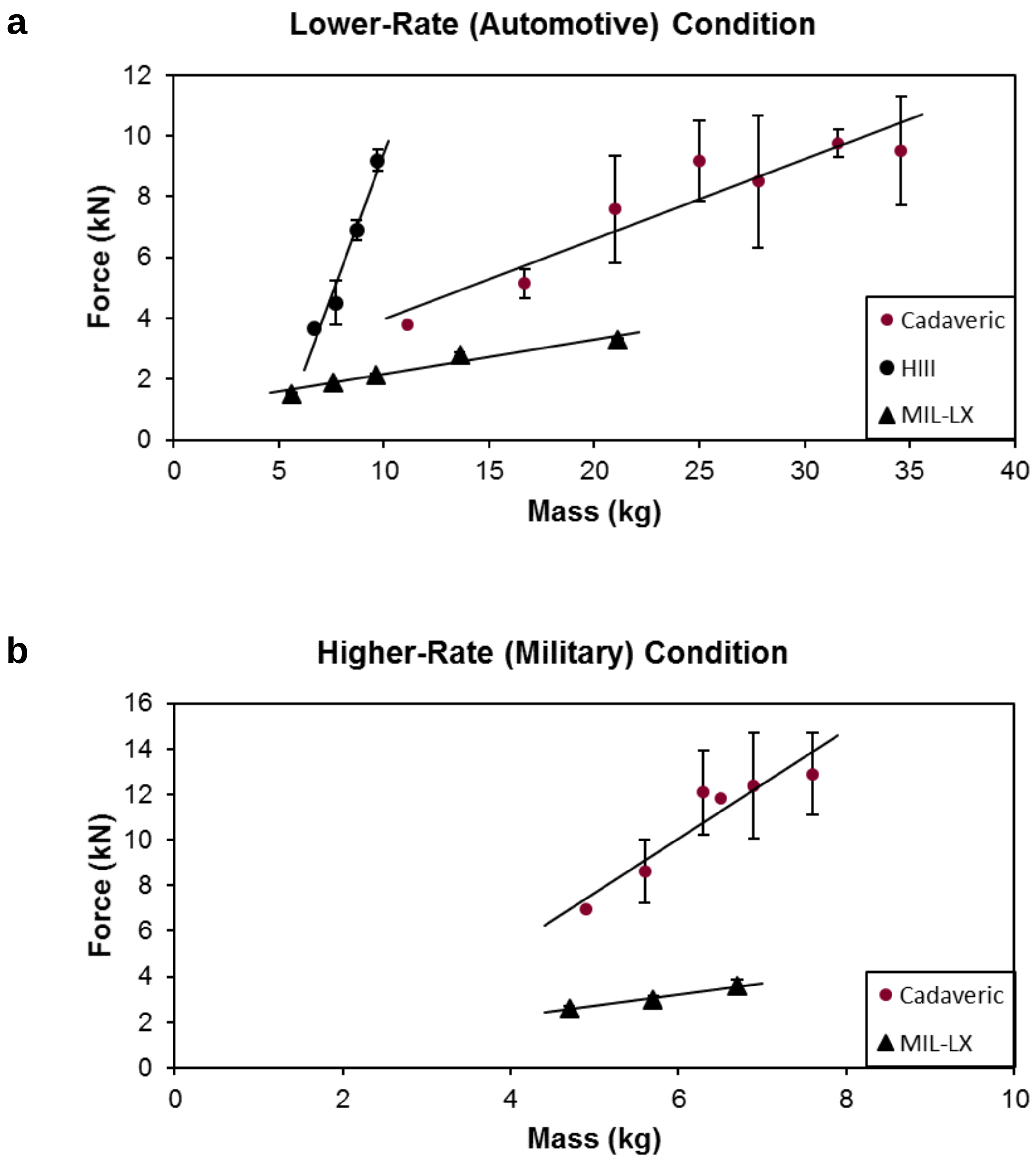

Figure 3.13: Mass-Force Curves for Cadaveric and ATD Tibias
Impact testing of the Hybrid III and MIL-LX legs at the **a)** lower-rate automotive and **b)** higher-rate military impact conditions was used to assess their ability to predict fracture. Non-injurious tests from cadaveric testing were used to compare to ATD testing, since the ATDs do not fracture and absorb energy during fracture like natural bone does. Standard deviation values are shown as error bars. The small standard deviation values in the force prediction of the ATDs make them difficult to see in the figure.

3.4 Discussion

This study examined the fracture tolerance of the tibia and the effect of impulse and load duration on injury risk during automotive and military axial impacts. While there have been several studies that have conducted experimental testing on the lower leg (*e.g.*, Quenneville *et al.* 2011, Yoganandan *et al.* 2014, Bailey *et al.* 2015), the effect of varying impact duration has not been seen previously in the literature. Since most of the prior research has focused on automotive injuries, understanding the effect of impulse is critical in determining whether automotive results can be successfully applied to military blast scenarios.

While the tri-axial accelerometer fixture that was designed provided an inexpensive method to measure high magnitude accelerations in three axes, there were issues with the fixture during preliminary testing using isolated tibia specimens. Due to the curvature of the bones, the flat surface of the fixture proved difficult to glue to the specimens. To try and fix this issue, zip ties were wrapped around the fixtures to provide added support when attaching to the bone, but this method did not totally eliminate the issue. Testing using the pneumatic impact apparatus revealed that forces in the medial/lateral direction were very small during axial loading of the tibia. For future measurements using bone specimens, simply using a dual-axis accelerometer may suffice. This would eliminate the need for a tri-axial fixture and would reduce the mass of the accelerometer, making it much easier to glue to bones.

All strain gauges were attached to the tibia specimens several days before the testing process began so that the specimens were already instrumented and simply had to be thawed on the day of testing and so CT scans of the instrumented bones could be obtained. In the process of moving the specimens in and out of the freezer for storage, several of the strain gauge wires detached. Zip ties were added to the specimens, wrapped around the strain gauge cables to provide strain relief. This step was added to the specimen attachment procedure to prevent this from happening in future studies.

The results from impact testing showed that the greatest force and impulse values occurred prior to the fracture test in three of the twelve specimens. During this "pre-fracture" test, a crack often became visible in the cartilage on the articular surface of the tibia, suggesting that forces were very close to the failure level and that the pre-fracture and fracture tests very narrowly identified the tolerance level of the tibia. The pre-fracture tests had the greatest forces and impulses due to the absorption of energy during the fracture test. The peak force was used for statistical analysis since it is most indicative of the tolerance of the lower leg, as the body is not typically subjected to repeated impacts of this magnitude. Peak values that were used for statistical analysis for the factors that were found to predict injury occasionally occurred in different tests, which may not be truly representative of the conditions that caused fracture. However, this method was believed to be acceptable since only choosing the test that had peak force values would neglect the fact that the specimen actually did withstand greater amounts of energy at another impact, and therefore it would be a misrepresentation to call this a failure test.

The best subset regression analysis revealed that several factors, including projectile velocity, kinetic energy, impulse, and loading rate, provide the most accurate method of injury prediction. The number of factors identified by the regression analysis suggests that fracture is not controlled by a single variable, but a combination of several. While it must be acknowledged that there is a degree of interdependence that exists among these factors, as kinetic energy, impulse, and loading rate are dependent on the velocity, several of these factors are not often measured experimentally in safety tests (*i.e.,* impulse and loading rate), and the data suggest that their measurement and consideration may lead to more accurate injury prediction. It is likely that this interdependence led to the low coefficient of determination obtained from the best subset regression analysis.

Specimens tested in the lower-rate automotive condition with longer impact durations required significantly smaller axial forces to achieve fracture when compared to the shorter duration military condition. As such, limits established for military situations could be higher than automotive limits if the same level of risk is acceptable. This could have great implications in terms of survivability aspects of military vehicle design. The data also indicated that specimens tested in the automotive condition require a significantly greater impulse to achieve fracture when compared to the military condition. Even though peak forces are lower in the automotive condition, the longer load duration means these impacts typically have higher impulse values. The results therefore show that impulse is not equivalent between the two test conditions, and therefore cannot be used as a single injury predictor. However, the kinetic energy was not found to be significantly different between test conditions. Kinetic energy has previously been identified as a significant factor that influences failure (Quenneville *et al.* 2011), which suggests that kinetic energy should be considered a contributing factor to injury risk, along with force, and therefore would be useful to measure in future impact testing. However, the kinetic energy values from Quenneville *et al.* (2011) did not match with the kinetic energy values from this work, so this factor might be dependent upon the testing configuration and could be a topic of further research. Impulse values have not been typically reported in other previous studies, but this could be of benefit when defining the fracture tolerance of bones, and should be included in future studies to allow for comparison. The axial loading rate in the present study ranged between 1.2 and 9.2 kN/ms, which was similar to loading rates that have been produced in previous studies simulating automotive axial tibia impacts (between 0.05 and 8.1 kN/ms) (Bailey *et al.* 2015). Previous military blast studies have identified loading rate as a predictor of fracture risk during axial loading and have also concluded that due to the viscoelastic properties of bone, impacts with larger loading rates and short duration can tolerate higher force magnitudes (Griffin *et al.* 2001), which is consistent with the results from this work.

While no other work has investigated the effect of impact duration on the fracture tolerance of the tibia, the average peak fracture force values of 10.9 – 13.5 kN lie within the range of expected values reported in previous work. Quenneville *et al.* (2011) conducted similar impact testing on isolated tibia specimens and reported average axial fracture forces of 12.6 kN. Several previous studies have conducted impact testing on intact lower leg specimens to identify the fracture tolerance of this region of the body, and proposed peak axial force criteria ranging from 2.4 kN (Seipel *et al.* 2001) to 7.9 kN (Quenneville *et al.* 2011), corresponding to a 10% risk of injury.

The current North Atlantic Treaty Organization (NATO) standard for assessing lower leg injury from short-duration loading events corresponds to a 5.4 kN force. Since the axial force was found to be significantly different between the lower-rate test condition and the higher-rate condition, two injury risk curves based on axial force were developed for this study, one corresponding to each test condition. The probability curves based solely on force were used to compare with previous studies, to eliminate the interdependence that exists among the various factors used to predict fracture, and to compare to experiments on surrogate test devices, since force is the main output of an ATD. Based on these curves, a 10% risk of fracture corresponded to 9.0 kN for longer duration impacts, such as frontal automotive collisions and 12.2 kN for shorter duration impacts, such as military blasts. These values are greater than those established in previous literature. The greater fracture tolerance of the present work may be attributed to variations in the experimental configuration used when compared to previous studies, including the lack of foot, ankle, and soft tissue in specimens, load cell location at the distal tibia, the use of only male specimens, the lack of simulation of muscle tension prior to impact, and varying boundary conditions (*e.g.*, specimens fixed to linear rail systems compared to specimens hanging from chains). The large degree of variance in experimental configurations seen in studies highlights the need for a standard methodology for boundary conditions and variables to be included in fracture tolerance analysis. It is possible that due to the lack of foot and ankle in the specimens used in this study, the fracture tolerance of the lower leg may be overestimated, since previous lower leg axial impact tests frequently see fractures to the calcaneus. However, it is reasonable to assume that the trends noticed in this tibia study should translate to other bones of the body, and as such, load duration likely should consistently be included as a factor in future works. Due to the natural curvature of the tibia, significant forces were measured in the anterioposterior direction, meaning that a degree of bending is induced in the tibia, even when the specimen is aligned so the delivery of impact is axial. It is likely that the bending in the bone has a contribution to inducing fractures, and may be of interest to include in future injury tolerances, even when subjecting specimens to axial loads.

Impact testing of the Hybrid III lower leg simulating a frontal automotive collision revealed a 10% risk of fracture force of 19.9 kN when compared to the cadaveric testing. This value is much higher than 5.4 kN used as the standard for assessing injury risk (North Atlantic Treaty Organization HFM-090 Task Group 25 2007), which agrees with previous literature that has identified the overly stiff nature of this device. Testing of the Hybrid III under an impact simulating a military blast produced forces that exceeded the capacity of the load cell (even with the smallest projectile available), so the higher-rate military condition could not be tested for the Hybrid III. Based on this, it is likely that the Hybrid III lower leg is not suitable for these high rate impacts. Previous studies that have subjected the Hybrid III leg to axial impacts simulating a military blast have revealed that force measurements are higher by a factor of three (Bir *et al.* 2008, Quenneville and Dunning 2012). The results of the present work indicate that the Hybrid III overestimates force measurements by an even larger factor than that, approximately 3.7. The MIL-LX legform achieved much better results in terms of fracture prediction. The current injury limit of the MIL-LX for axial impacts is 2.6 kN measured at the upper tibia load cell

(North Atlantic Treaty Organization 2011). The load corresponding to the test conditions that would lead to a 10% risk of fracture in the cadaveric results was 2.8 kN for the lower-rate condition and 3.1 kN for the higher-rate condition. This study showed that the MIL-LX can be accurately used as an injury prediction tool for axial impacts with a range of load rates, which is in accordance with previous studies that evaluated the biofidelity of the MIL-LX (Quenneville and Dunning 2012). The ability of these ATDs to accurately predict the injury risk for humans subjected to the same input conditions is crucial when developing and evaluating appropriate protective systems.

There are several limitations of this work that must be acknowledged. The specimens tested had all soft tissue and the fibula, foot and ankle removed, and muscle tension in the specimens was not simulated. However, the inertial effects of the soft tissue were simulated via the ballast mass. Also, the use of an artificial talus to transmit loads to the cadaveric specimens may have introduced stress concentrations, however, this method ensured that fractures were localized to the tibia, rather than throughout the lower limb. Another limitation of this work was the number of impacts to which each specimen was subjected, and any damage that may have developed during repeated testing. However, one of the specimens from each of the test conditions (specimen 1538L for the lower-rate condition and specimen 1494L for the higher-rate condition) fractured at the very first impact delivered and exhibited fracture forces within the range of the other specimens, suggesting that repeated testing did not substantially affect the range of force tolerances identified herein. Subjecting specimens to fracture with a single impact would make it impossible to determine if a similar result could be achieved at impacts of lower magnitude. The repeated testing also allowed for the identification of other factors as predictors of fracture, not just force. The force that the specimens required to produce fracture was greater than was anticipated, which led to a high number of impacts for each specimen. Most fractures were achieved at the maximum limit of performance of the impacting apparatus.

The experimental work outlined in this chapter has led to a better understanding of the effect of impact duration of the fracture tolerance of the tibia. Due to the viscoelastic properties of bone, automotive impacts with longer durations and smaller loading rates required smaller forces to produce fracture than higher-rate impacts with shorter durations. It has also been shown herein that the most accurate functions to predict injury do not rely solely on impact force, as is seen in previous works, but should rely on other variables as well. Revised injury force standards were developed for impacts with longer durations, such as those seen in automotive impacts, and higher-rate impacts that occur in military underbody blasts. Finally, the biofidelity of two lower leg ATDs was investigated and new load limits were proposed. The Hybrid III leg overestimated forces in the tibia but the MIL-LX performed much better in terms of fracture limit prediction, and as such, the MIL-LX may be more appropriate for evaluating injury to this region of the body over varied impact conditions.

CHAPTER 4 – FINITE ELEMENT MODEL OF A TIBIA FOR IMPACT ANALYSIS

Overview: *This chapter details the development and validation of a finite element model of the tibia for impact analysis. The impact testing conducted in Chapter 3 was simulated using this model, and was investigated by comparing its ability to predict injury risk to the load data determined during experimental testing and failure criteria from the literature.*

4.1 Introduction

Experimental studies using post-mortem human subjects (PMHS) are used in academia to determine injury limits for areas of the body under specific loading conditions. However, the use of biological specimens is not common in industry, mainly due to their limitations in terms of cost, the inability to perform repeated testing, and the ethics and inconveniences of dealing with biological samples. Anthropomorphic test devices (ATDs), or crash test dummies, are commonly used, but these devices also have limitations since they typically have unrealistic ranges of motion, do not reproduce fractures, may be overly stiff, and impact tests (*e.g.*, full vehicle car crashes) are very costly. The automotive and military industries have adopted the use of finite element (FE) modelling as a complement to ATD tests, which allow for repeated testing under any user-specified conditions.

Several previous studies have developed FE models of the lower leg. Most of these studies have had a focus on either automotive loads (Shin *et al.* 2012, Untaroiu *et al.* 2013) or military blast loads (Dong *et al.* 2013). These FE models were developed based on medical imaging scans of a cadaveric limb to produce accurate tissue geometries. The material properties for biological tissues and the boundary conditions of the impact of interest were then assigned in the model. Models have been typically validated to ensure the accuracy of their responses by comparing their ability to predict injury with experimental data. Once a model is developed and validated, it becomes an extremely powerful tool in terms of risk of injury assessment, since the loading and boundary conditions can be easily adjusted and the model can be used for unlimited studies. Computer models also allow for protective systems to be evaluated and optimized earlier in the design process before fabrication occurs.

The goal of this study was to refine a FE model of the isolated tibia for varied impact loading simulations. This model was based on an isolated tibia mesh previously developed by Quenneville and Dunning (2011). Furthermore, Duffy (2015) developed a FE model of the experimental configuration and mechanical components that were used for the experimental testing in Chapter 3. In this work, the components of that model were adjusted and combined with the previously developed isolated tibia to create a model that replicates the impact testing conducted in Chapter 3, and was assessed against the data gathered from that work.

4.1.1 Previous Isolated Tibia Model

The FE model was largely based on a model previously developed by Quenneville & Dunning (2011). This previous model of an isolated tibia included the cortical bone, cancellous bone, and marrow in the tibia, and the components of their experimental configuration. The mesh geometry of the bone was created using a CT scan of a right-sided male tibia specimen from a 49-year-old donor. The donor used to serve as the basis of the model was chosen as it had the most average response (based on donor age, weight, height, and impact force). The model response was verified through comparison to results from this representative specimen. This specimen had been subjected to four impacts with increasing levels of energy in the experimental testing, three non-injurious impacts and a final fracture impact. These four impact conditions were simulated in the model, and axial force, impact duration, impulse, and strain used to evaluate the response of the model. Results showed that peak force was within 10% of the experimental values for all tests except the fracture test. Impact duration values were between one and two times as much in the experimental testing when compared to the simulation, and impulses were 1 – 1.4 times as much experimentally when compared to the model. Von Mises stress and maximum principal strain were used to evaluate regions of bone failure in the model by plotting both the non-fracture and fracture tests, and only Von Mises stress in the cortical bone appeared to be a good indicator of fracture.

4.1.2 Previous Model of Experimental Components

For the model's response to best match the results from the experimental testing, the experimental configuration needed to be replicated as closely as possible within the model. The apparatus used to conduct impact testing of the isolated tibia differs from that of Quenneville & Dunning (2011), therefore the new experimental components needed to be modelled. Duffy (2015) developed a finite element model that included the testing components at the Injury Biomechanics Laboratory at McMaster University to conduct impact testing on bones (Figure 4.1). The components added by Duffy (2015) included a ballast mass that was affixed to the proximal end of the tibia, a back plate and top plate to hold the specimen, two chains to suspend the specimen and a top rail to support all specimen components. The ballast was modelled as steel with elastic modulus of 200 GPa and Poisson's ratio of 0.3, and its density was adjusted to produce the required mass given its volume (total required mass = 12.9 kg). The bone pot, back plate, top plate, and top rails were modelled as rigid steel components. The chains that suspended the specimen in the test frame were modelled as 1D elements with the properties of steel.

4.2 Methods

4.2.1 Software Overview

The meshes for the tibia (including cortical bone, cancellous bone, and marrow) were imported from Quenneville and Dunning's (2011) model, while the meshes for the

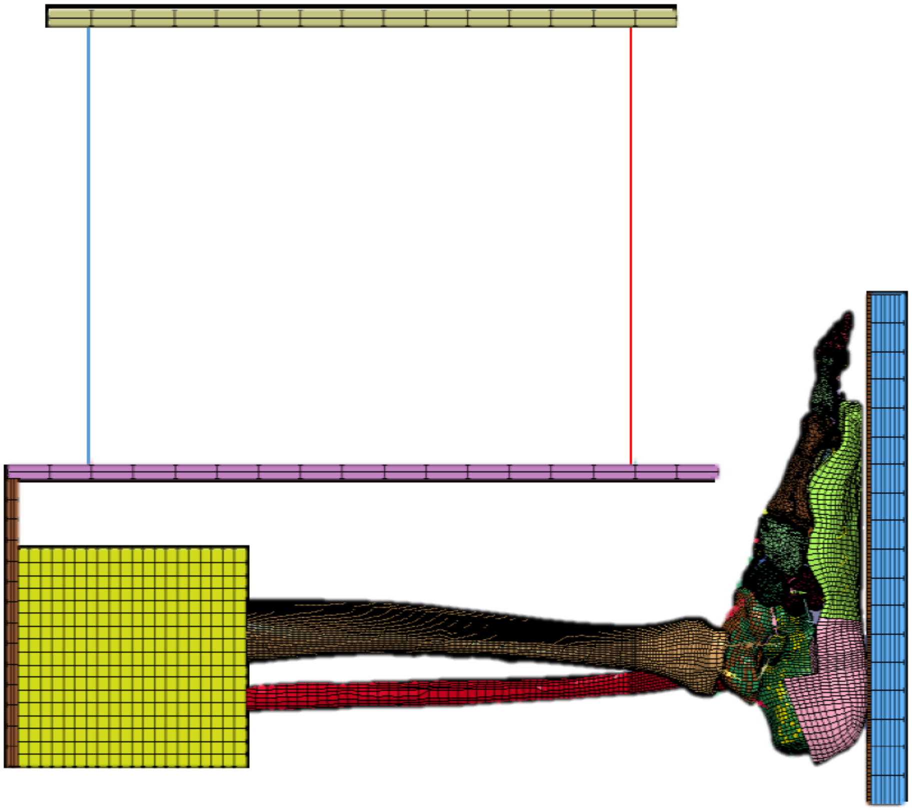

Figure 4.1: Previously-Developed Lower Leg Model
The lower leg model previously developed by Duffy (2015) included components of the experimental configuration used at the McMaster Injury Biomechanics Laboratory. The suspending chains, back plate, top plate, and rails from which the specimen hung were incorporated into the current isolated tibia model.

top rail, steel chains, top plate, and back plate were imported from Duffy (2015). All meshed components were imported into LS-PrePost®, the preprocessor for LS-DYNA® (LSTC, Livermore, CA, USA) finite element analysis software. LS-DYNA® is an explicit finite element solver that is used extensively by the automotive and military industries due to its ability to model simulations of large deformations. LS-PrePost® was then used to mesh additional components not previously created, and also for pre-processing of the model, including the application of boundary conditions, definition of contact between parts, and assignment of material properties. LS-PrePost® was also used to post-process the results of the simulation for generation of load curves and stress/strain fringe plots.

4.2.2 Experimental Components and Material Properties

The finite element model consisted of the tibia, which includes cortical bone, cancellous bone, and bone marrow, and components of the experimental setup that were used in Chapter 3 subject the tibia specimens to impacts. The setup included a top rail that holds the specimen in the test chamber, two chains that suspended the specimen, a top plate and back plate that held the specimen, a pot that consisted of dental cement in a section of PVC to which the bone is attached, the artificial talus used to transmit the loads to the distal surface of the bone, an impacting plate, the deformable sponge that is attached to the impact bracket, the projectile, and the rail that the impact bracket travelled on through bearings. All of these components were represented in the model as different parts with separate meshes (Figure 4.2). All units in the model were selected to be consistent with mm, ms, kg, and kN.

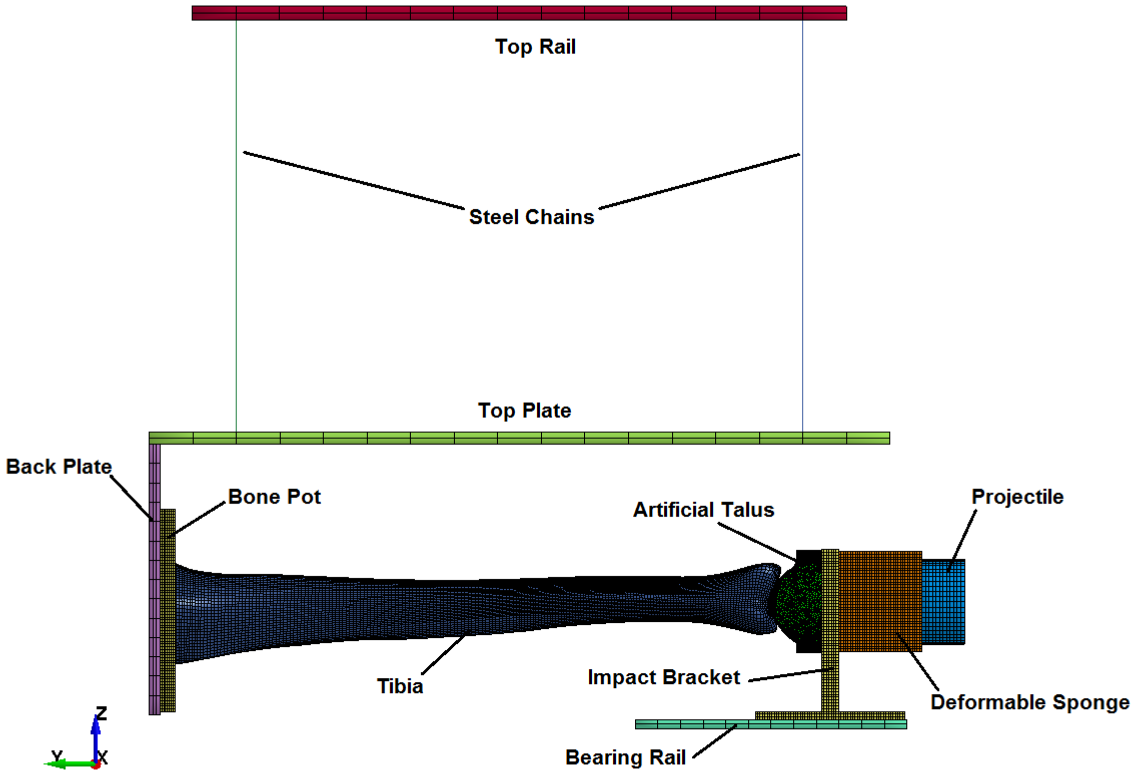

Figure 4.2: Complete Tibia Model for Impact Analysis
The final tibia model is composed of the tibia mesh and the components of the experimental setup including the top rail, two chains, top plate, back plate, bone pot, bone specimen, artificial talus, impact bracket, bearing rail, deformable sponge, and projectile.

4.2.2.1 Rigid Components

Several of the components in the model, including the top rail, top plate, back plate, bone pot, bearing rail, and projectile were made of steel. These components were modelled as rigid materials (LS-Dyna® material model MAT 20) since they experience negligible deformations during impact testing when compared to the deformable bone and sponge. The top rail, top plate, back plate, and bearing rail were assigned material properties corresponding to steel (ρ = 8,000 kg/m^3; E = 210 GPa; ν = 0.3). All of the rigid components were modelled using a constant stress solid element formulation (ELFORM 1) to increase analysis speed, since this is the least computationally expensive element type.

LS-DYNA® documentation recommended that the mesh defining a rigid body be as fine as any deformable body that contacts it, in order for contact force to be realistically distributed (LSTC 2015). For this reason, the bone pot was meshed to be as fine as the proximal region of the tibia based on the characteristic length of the elements. Since the bone pot was rigid and only there for inertial purposes, the mesh was created to only be a few elements thick, to limit the number of elements in the model and save computational costs. The projectile was meshed to match the geometry of the head of the projectile that impacts the deformable sponge during experimental testing. Density values for the bone pot, top rail, and projectile were assigned by measuring the volume of the parts using LS-PrePost® and assigning the necessary density to generate the mass of those components as used during experiments. In the experimental testing, a ballast mass was attached on top of the top rail that hung from chains. To mimic the experimental distribution, the model's top rail that hangs from the steel chains was given a density value that included this additional ballast mass. The modulus and Poisson's ratio values for the bone pot, top rail, and projectile were the same as the other steel components.

4.2.2.2 Steel Chains

In the experimental setup, the specimen was attached to a mounting frame that was suspended from steel chains in the test chamber. The chains were maintained as 1D beam elements attached to nodes at the top rail and nodes at the top plate to allow the swinging motion of the specimen to occur. The chains were assigned material properties that correspond to steel (ρ = 8,000 kg/m^3; E = 210 GPa; ν = 0.3) and modelled using the fully integrated element formulation (ELFORM 3).

4.2.2.3 Impact Bracket

In the experimental configuration, a steel impact bracket was secured onto two bearings on a rail system that allow it to move forward and transfer loads to the specimen. The large forces that were applied to the impacting plate induced a bending moment and corresponding friction on the bearing as it travelled along the rails. To accurately represent the friction and associated motion of loading, the geometry of the impact bracket was meshed. The impact bracket was modelled as an elastic body to allow it to bend and apply a force against the bearing rail, and assigned material properties of steel.

4.2.2.4 Deformable Silicone Sponge

The large deformations that the silicone sponge experienced during impacts made it a challenging material to model. The silicone sponge was meshed in LS-PrePost® to match the dimensions of the sponge used during experimental testing. A low-density foam (LS-Dyna® material model MAT 57) was used to model this component. This material model is typically used to simulate seat cushions and other highly compressible, low density foams (LSTC 2015). A compression test using an Instron® materials testing machine (ElectroPuls E1000, Instron® Engineering Corporation, Norwood, MA, USA) was used to determine the modulus and generate a stress-strain curve for the sponge, which were required to define its material properties. The sponge was tested to 0.7 strain at a rate of 50 mm/min. To ensure repeatable results, testing was repeated three times and an average stress-strain curve was produced. This part was modelled using the constant stress solid element formulation (ELFORM 1).

4.2.2.5 Artificial Talus

The geometry of the artificial talus used to impart the impact load to the tibia was extracted from its 3D CAD file and imported into Mimics® medical imaging software (Materialise, Leuven, Belgium) for tetrahedral meshing (Mimics® software is not capable of hexahedral meshing). The talus could not be modelled as a rigid material since rigid materials do not provide force outputs in LS-Dyna®, and the interface between the talus and bone is a major area of interest in terms of force measurement since it corresponded to the location of the load cell in the experimental tests. This part was instead modelled using an elastic material model (LS-Dyna® material model MAT 1) with material properties of acrylonitrile butadiene styrene (ABS) plastic. The constant stress solid element formulation (ELFORM 1) was used to model the talus.

4.2.2.6 Tibia

The tibia model used in this work was previously developed by Quenneville and Dunning (2011). This model of the tibia was potted, similar to the method used in the testing conducted in Chapter 3, and included cortical bone, cancellous bone, and bone marrow. All bone components were modelled using the ELFORM 1 constant stress element formulation.

The material properties in the present study were kept the same as were used in Quenneville and Dunning (2011). The cortical bone was modelled as an elastic-plastic material (LS-Dyna® material model MAT 24), which is defined using material and strain rate dependency properties. The properties of cortical bone were taken from the literature. These included a density of 1,850 kg/m^3, an elastic modulus of 17 GPa, a Poisson's ratio of 0.3, a yield stress of 0.125 GPa, and a tangent modulus of 1 GPa. The strain rate dependency of bone was modelled using a family of curves method obtained from Untaroiu *et al.* (2004). This method uses stress versus strain curves defined at several different strain rates to determine the material's strain rate dependency.

Similarly, the cancellous bone was also modelled using an elastic-plastic material model, with material properties obtained from the literature: density of 1,000 kg/m^3, elastic modulus of 0.4 GPa, Poisson's ratio of 0.3, yield stress of 10 MPa, and tangent modulus of 0.025 GPa. Since a family of curves could not be found in the literature for cancellous bone, a Cowper-Symonds method was used to accounts for strain rate effects. This model scales the yield stress by the factor:

$$1 + \left(\frac{\dot{\varepsilon}}{C}\right)^{1/p} \quad \textbf{(Eq. 4.1)}$$

where $\dot{\varepsilon}$ is the strain rate, C = 360.7 and p = 4.605 (Iwamoto *et al.* 2005).

The marrow was simply modelled as an elastic material (LS-Dyna® material model MAT 1) with a density of 1000 kg/m^3, a modulus of 200 MPa, and a Poisson's ratio of 0.35.

4.2.3 Contact and Boundary Conditions

Accurate modelling of contact interfaces is essential to the predictive capability of a finite element model. Contact parameters among all the model parts needed to be defined so the model recognizes how they should interact with each other. In LS-DYNA®, contact defines (via parts, part sets, segment sets, and/or node sets) which locations should be checked for potential penetrations of another part. The program checks for penetrations by the slave nodes into the master segments at every time step, and if penetration is detected, a restoring correction is applied to resist and eliminate the penetration. Determining which location to assign as the slave segment and which to assign as the master segment depends on a variety of factors, including the coarseness of the mesh and how deformable each part is.

The contact card *CONTACT_TIED_NODES_TO_SURFACE_OFFSET was used to define the contacts between the top plate and the back plate, and the back plate and the bone pot. All of these components were rigid, which means that constraint-based contacts could not be used with these materials (LSTC 2015). The OFFSET option turns a constraint-based contact into penalty-based, which can be used with rigid parts. In the case of the contact between the top plate and the back plate, a slave node set was created at the back plate that was tied to a master segment set on the top plate. In the case of the contact between the back plate with the pot, a slave node set was created at the bone pot that was tied to a master segment set on the back plate.

The contact card *CONTACT_TIED_SURFACE_TO_SURFACE_OFFSET was used to define contact between deformable components of the apparatus using segment sets (the proximal end of the tibia with the bone pot, the base of the talus with the impact bracket, and the impact bracket with the deformable sponge). This contact type allowed for the surface of the talus and surface of the deformable sponge to be tied to the elastic impact bracket as it translated forward.

Contact between the surface of the talus and the distal articular surface of the bone was defined using the *CONTACT_AUTOMATIC_SURFACE_TO_SURFACE card. Segment sets were defined at the interfacing surfaces and this two-way treatment of contact checks for penetrations by both surfaces in the contact. Due to the presence of cartilage on the articular surface of the tibia, a very low frictional coefficient was assigned to this contact (0.01) for both static and kinetic friction (Hamill and Knutzen 2003). To ensure accurate placement of the talus against the distal articular surface of the tibia, the talus was positioned against the distal surface of the tibia using automatic contact detection. The talus and tibia were both aligned in the anteroposterior and mediolateral axes when they were imported into LS-PrePost®. The talus was then moved axially towards the tibia until it was just making contact with the articular surface, without any initial penetrations.

Contact between the impact bracket and bearing rail was also defined using the CONTACT_AUTOMATIC_SURFACE_TO_SURFACE card, again with segment sets defined at the interfacing surfaces. To model the frictional forces of the impact bracket as it moved along the bearing rail, an iterative process was used to determine the frictional coefficients to assign to this contact. This involved independently varying the values of the static and kinetic frictional coefficients from values between 0 and 0.1 by increments of 0.05. The frictional coefficients were adjusted in an attempt to match the peak axial force from the non-fracture experimental tests. The values that reduced the peak force error between the two non-fracture test were then used for all simulation trials.

The contact between the projectile and the deformable sponge was also defined using automatic surface to surface contact, except the entire parts were used to define the contact instead of segment sets, due to the large deformation the sponge experienced during impacts. For this same reason, interior contact was defined for the sponge to prevent its nodes from penetrating its own faces.

The top rail and bearing rail were constrained in all directions to remain stationary during impact. The bone specimen, bone pot, back plate, and top plate were left unconstrained and free to move in any direction, similar to the movement of the specimen during experimental testing. The talus, impact bracket, deformable sponge, and projectile were constrained to move only in the y-direction (the direction of impact), to produce purely axial movement.

To accurately model the swinging movement of the specimen after impact, gravity was included in the model to act in the negative z-direction. Impacts were modelled using an initial velocity in the positive y-direction for the projectile, in accordance with the experimental testing conditions.

4.2.4 Comparison to Experimental Results

Of the six donors that were tested experimentally, one was selected to use for validation of the finite element model. Selection was based on an evaluation of the age and fracture force for both test conditions. In order to choose the most representative data, each donor was ranked on its proximity to the average value for each factor, and the donor with the 'most average' overall rank was selected, which was donor 1567 (Table 4.1). The force curves from both tibias from this donor were compared to those of the model, in order to assess the model's ability to predict fracture forces from impacts.

The model was subjected to four scenarios in order to assess its validity in predicting response during dynamic impacts. Both the lower-rate automotive and higher-rate military experimental conditions were replicated in the model for non-fracture and fracture tests, to assess its performance at varying loading rates. Since donor 1567 was deemed to have the most representative specimens, the model was subjected to the same test conditions as those bones. The projectile mass and projectile velocities from non-fracture and fracture tests from donor 1567 were therefore the inputs for the model (Table 4.2).

Table 4.1: Selection of Most Representative Donor

Donors were ranked according to their age and fracture forces in both the lower-rate and higher-rate test conditions being closest to the average of all specimens tested. Donor 1567 was deemed the most representative of the sample population.

Donor	Age (years)	Age Rank	Low-Rate Force (N)	F_A Rank	High-Rate Force (N)	F_M Rank	Sum	Overall Rank
1494	50	6	10,672	3	13,275	3	12	5
1536	55	4	10,826	2	14,258	4	10	3
1538	66	2	9,063	6	13,500	1	9	2
1541	68	3	12,802	5	11,812	6	14	6
1567	61	1	11,257	4	13,311	2	7	1
1600	74	5	11,002	1	14,542	5	11	4
Average	62.3		10,937		13,450			

Table 4.2: Model Testing Conditions

The model was validated using four testing conditions. Both a fracture test and a non-fracture test were simulated under both experimental conditions to investigate the model's ability to predict tibia response at varying dynamic loading rates. The corresponding projectile mass and projectile velocity for the experimental tests were inputs for the model.

Test	Projectile Mass (kg)	Projectile Velocity (m/s)
Lower-Rate Non-Fracture	21.0	6.2
Lower-Rate Fracture	34.6	6.2
Higher-Rate Non-Fracture	6.3	11.3
Higher-Rate Fracture	6.9	11.3

Several outputs of the FE simulation were compared to the results from experimental testing, including force-time curves, peak axial force, impact duration, and impulse. Force time curves between the simulation and the corresponding experimental test were plotted together for visualization by matching their time of peak force. Axial force was measured in the model between the contact of the base of the talus and impact bracket, as this corresponded to the location of the load cell that was used to measure loads experimentally. Impact duration was calculated using the force-time curves from the simulation, and these curves were integrated to find the area under the graphs, which represents the impulse delivered to the specimen. The simulation's values were compared to the values from cadaveric testing for each test condition by dividing the simulation value by the experimental value.

The model's ability to distinguish between a fracture test and a non-fracture test was evaluated using critical maximum principal strain and Von Mises stress values from literature. Areas with maximum principal strain values exceeding critical strain values of 0.016 for cortical bone (Untaroiu *et al.* 2005) and 0.134 for cancellous bone (Takahashi *et al.* 2000) were deemed as fracture points, while critical Von Mises stress values of 5.3 MPa for cancellous bone and 134 MPa for the cortical region were used (Untaroiu *et al.* 2005). Fringe plots were used to visualize regions that exceeded these critical values during all testing conditions.

Solid elements that are modelled with a constant stress formulations (ELFORM 1) can undergo hourglassing. Hourglassing is an artificial deformation mode that produces zero strain and no stress (LSTC 2015). This occurs in elements with a constant stress formulation due to the fact that they have a single integration point through each element, and the integration will misleadingly not record a stress if it remains unchanged at this location during a simulation (as would happen in a trapezoid-shaped deformation). To ensure that artificial deformation modes were not present in the model, the simulation's hourglass energy was evaluated. This was done by measuring the model's hourglass energy to determine if it remained below a threshold value of the simulation's total internal energy. An acceptable range of 10% or less of the total internal energy was used since this has been used in previous studies (Quenneville and Dunning 2011a).

4.3 Results

Modelling the impact bracket as an elastic component with the material properties of steel caused the impact bracket to experience bending during impact and exert a force against the bearing rail (Figure 4.3). Using peak force values from the non-fracture experimental testing, values of 0.1 for the static friction coefficient and 0.05 for the kinetic friction coefficient were chosen to model the frictional forces that occurred between the impact bracket and the bearing rail. Generally, a greater value for the coefficient of static friction decreased the peak force produced by the model, while a greater value for the coefficient of kinetic friction decreased the time to peak force.

Peak axial force during the lower-rate test condition was 7.9 kN (90% of experimental value) for the non-fracture condition (Figure 4.4) and 8.3 kN (73% of experimental value) for the fracture test (Figure 4.5). The peak force values for the

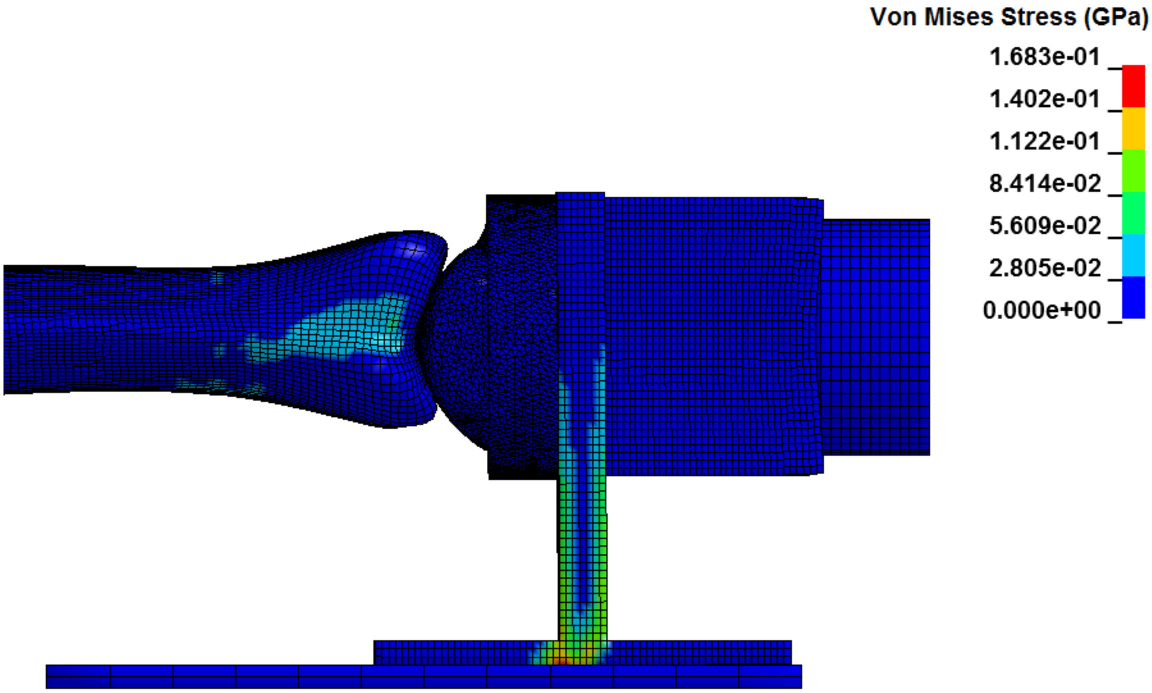

Figure 4.3: Impact Bracket Loading
The impact of the projectile striking the deformable sponge that was attached to the impact bracket caused a frictional force at the interface between the impact bracket and the bearing rail. The coefficients of friction between the impact bracket and the bearing rail were optimized to minimize errors in peak axial forces from non-fracture experiments. A static coefficient of friction of 0.1 and a kinetic coefficient of friction of 0.05 resulted in peak forces within 20% of those seen experimentally.

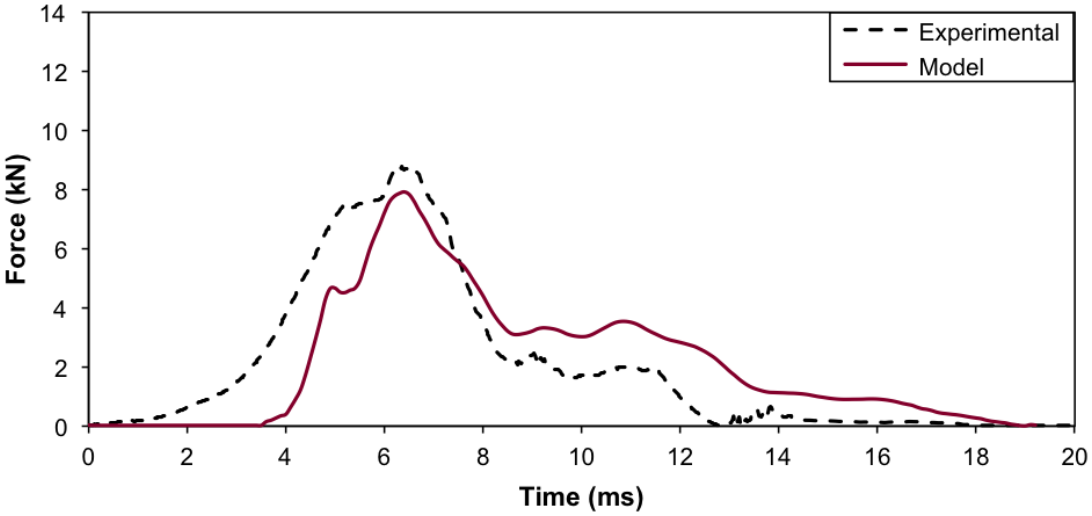

Figure 4.4: Force Curves for Lower-Rate Non-Fracture Tests
The peak force of the model was 90% of the experimental force, whereas impact duration was 127% as much. The model curve was represented in red, while the dashed black line represented the experimental curve.

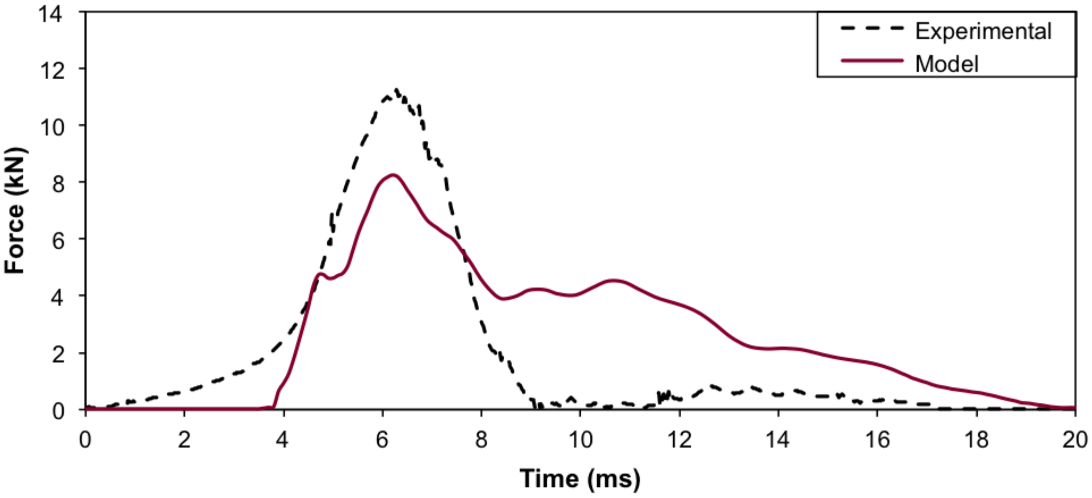

Figure 4.5: Force Curves for Lower-Rate Fracture Tests
For the lower-rate fracture test, the simulation achieved 73% of the experimental axial force, while duration was 133% as much.

higher-rate condition were 12.4 kN (118% of experimental value) for the non-fracture test (Figure 4.6) and 12.8 kN (96% of experimental value) for the fracture test (Figure 4.7).

A comparison of the peak force, impact duration, and impulse values between the simulation and experimental results is shown in Table 4.3a. The model values were presented as a fraction of the experimental values for these factors in order to compare the two (Table 4.3b). Impact duration values were larger in the FE simulation than the experimental values for all four test conditions. For the automotive tests, the duration was 15.2 ms (127% of experimental) in the non-fracture test, while duration was 16.1 ms (133% of experimental) in the fracture test. In the higher-rate condition, non-fracture duration was 8.4 ms (118% of experimental) while the fracture duration was 8.5 ms (185% of experimental). Impulse values were also larger in the simulation than in experiments.

Established thresholds from the literature for Von Mises stress and maximum principal strain were used as criteria to determine fracture in the model. Fringe plots were created for all four test conditions that showed regions of the distal surface of the tibia that exceeded the corresponding critical values, highlighted in red. For the lower-rate automotive test condition, maximum principal strain values that exceeded the established thresholds were not seen in cancellous bone in either the non-fracture or fracture tests, but miniscule regions were seen in the cortical bone in both the non-injurious and injurious tests (Figure 4.8). In terms of Von Mises stress, regions of fracture were seen in the cancellous bone, but in both the non-injurious and injurious tests; fracture was not seen in

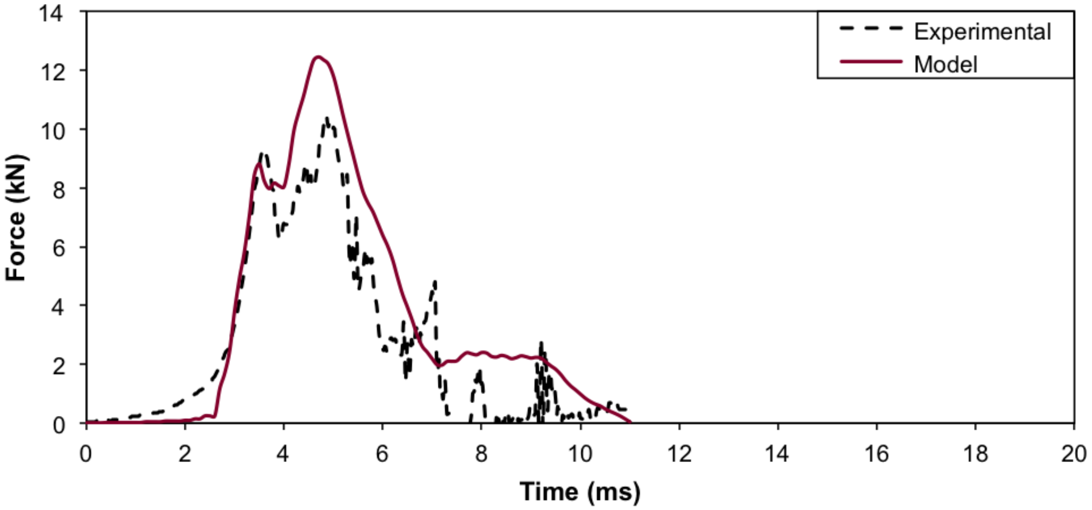

Figure 4.6: Force Curves for the Higher-Rate Non-Fracture Tests
Peak force of the simulation was 118% of the force from the experimental test, while duration was also 118% of the experimental value in the higher-rate non-fracture tests.

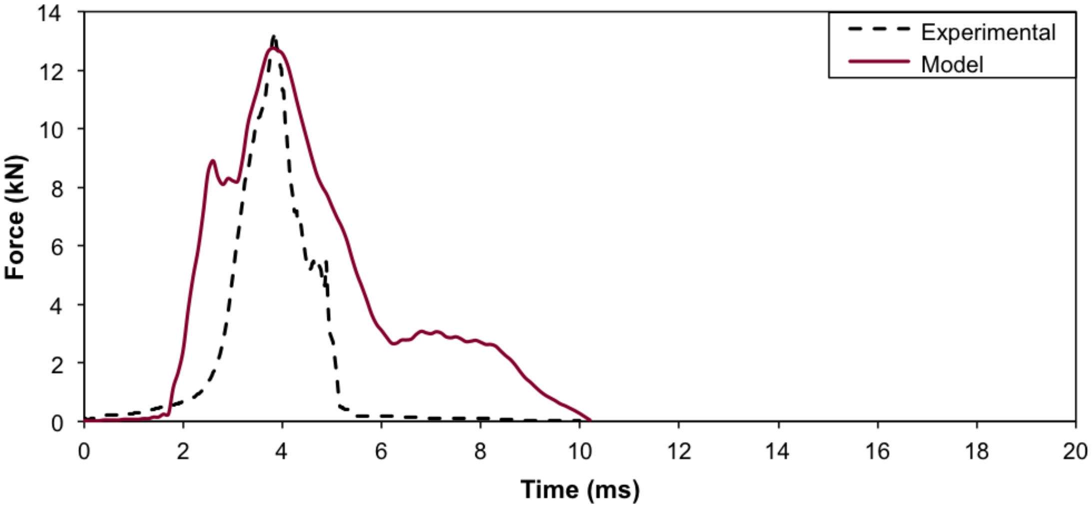

Figure 4.7: Force Curves for Higher-Rate Fracture Tests
Peak force of the simulation matched was 96% of the experimental value in the higher-rate fracture test, while duration was 185% of the experimental value.

Table 4.3: Summary of Model Validation Results
a) The values for peak axial force, impact duration, and impulse values for the four test conditions in the experimental and computational testing. **b)** These values were compared between the four simulation tests and the corresponding experimental tests by providing the ration between model values and experimental values.

a)

	Auto Non-Fracture		Low-Rate Fracture		High-Rate Non-Fracture		Military Fracture	
	Model	**Experiment**	**Model**	**Experiment**	**Model**	**Experiment**	**Model**	**Experiment**
Peak Force (kN)	7.9	8.8	8.3	11.3	12.4	10.5	12.8	13.3
Duration (ms)	15.2	12.0	16.1	12.1	8.4	7.1	8.5	4.6
Impulse (Ns)	41.0	39.2	51.3	37.5	38.7	27.3	41.9	18.2

b)

	Low-Rate Non-Fracture			Low-Rate Fracture			High-Rate Non-Fracture			High-Rate Fracture		
	F	**D**	**I**	**F**	**D**	**I**	**F**	**D**	**I**	**F**	**D**	**I**
Model/Experimental	0.90	1.27	1.05	0.73	1.33	1.37	1.18	1.18	1.42	0.96	1.85	2.30

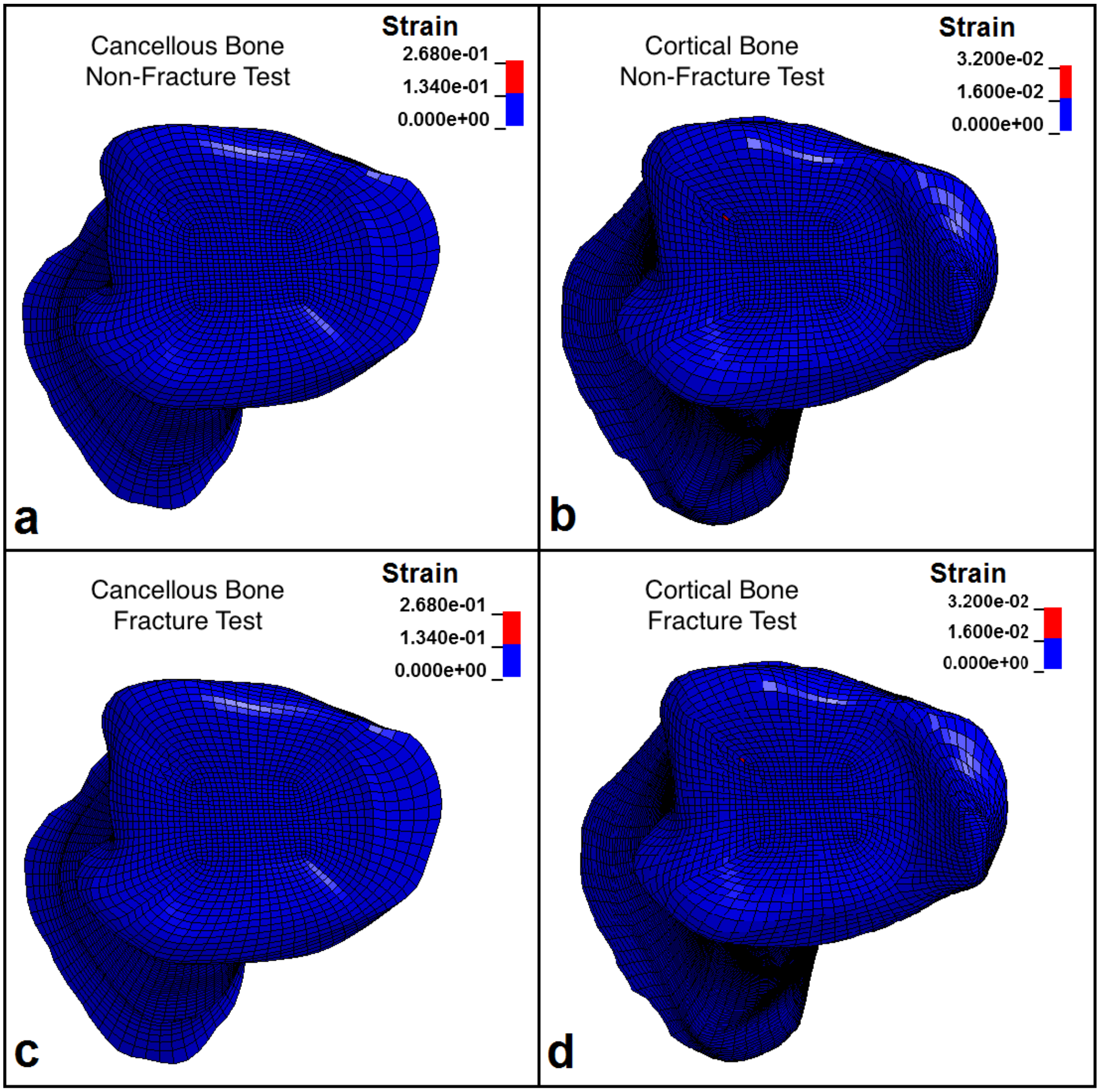

Figure 4.8: Maximum Principal Strain in the Lower-Rate Tests
The maximum principal strain shown for the two lower-rate tests in the **a)** cancellous bone for the non-fracture test; **b)** cortical bone for the non-fracture tests; **c)** cancellous bone for the fracture test; **d)** cortical bone for the fracture tests. The threshold for fracture was 0.134 for cancellous bone and 0.016 for cortical bone (elements exceeding these thresholds are shown in red).

the cortical bone (Figure 4.9). For the higher-rate military tests, maximum principal strains only predicted fracture in a very small region in the cortical bone in both the non-fracture and fracture tests (Figure 4.10). Von Mises stress during the military tests also only predicted fracture in the cortical bone and in both injurious and non-injurious tests (Figure 4.11).

The hourglassing that occurred in the model throughout each simulation was evaluated by comparing to the total internal energy of the model. Hourglass energy was between 2.0% and 3.0% of the total internal energy for all tests, and as such was deemed to be acceptable.

4.4 Discussion

Finite element simulations are extremely useful tools for determining the probability of injury of various areas of the body during loading. Due to their repeatability and versatility in the number of loading conditions that can be studied, these models are often used to assess injury risk by the automotive and defence industries. Several previous studies have developed models of the lower leg (Quenneville and Dunning 2011a, Shin *et al.* 2012, Dong *et al.* 2013, Untaroiu *et al.* 2013). These models have been validated by comparing their results to outcomes from cadaveric impact testing. Impact testing of the isolated cadaveric tibia was conducted in Chapter 3 to study the effect of loading rate on the fracture tolerance of the tibia by simulating automotive and military impacts. In this work, a model that was previously developed for short

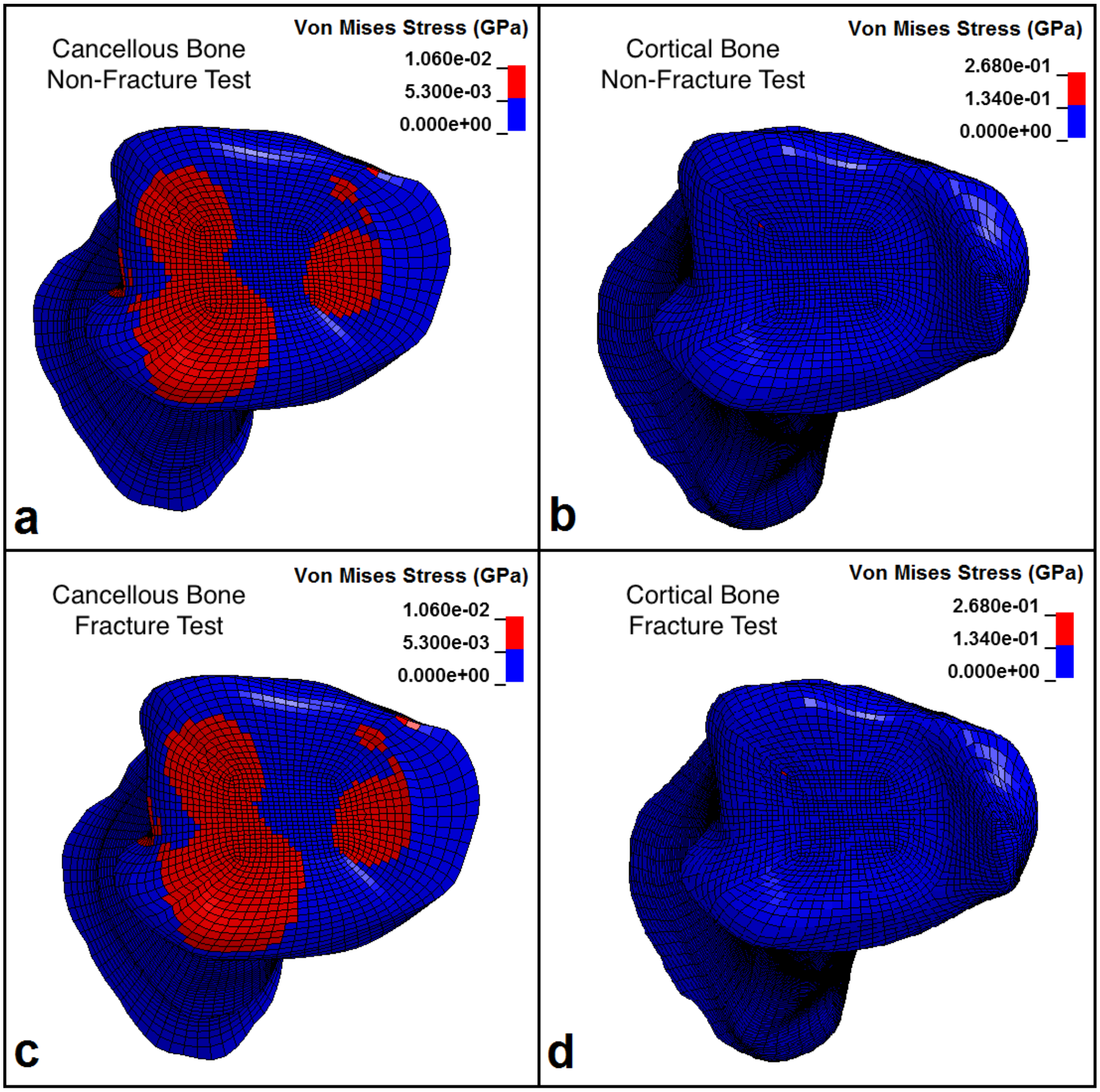

Figure 4.9: Von Mises Stress in the Lower-Rate Tests
The Von Mises stress shown for both the lower-rate tests in the **a)** cancellous bone for the non-fracture test; **b)** cortical bone for the non-fracture tests; **c)** cancellous bone for the fracture test; **d)** cortical bone for the fracture tests. The threshold for fracture was 5.3 MPa for cancellous bone and 134 MPa for cortical bone, with elements exceeding these values shown in red.

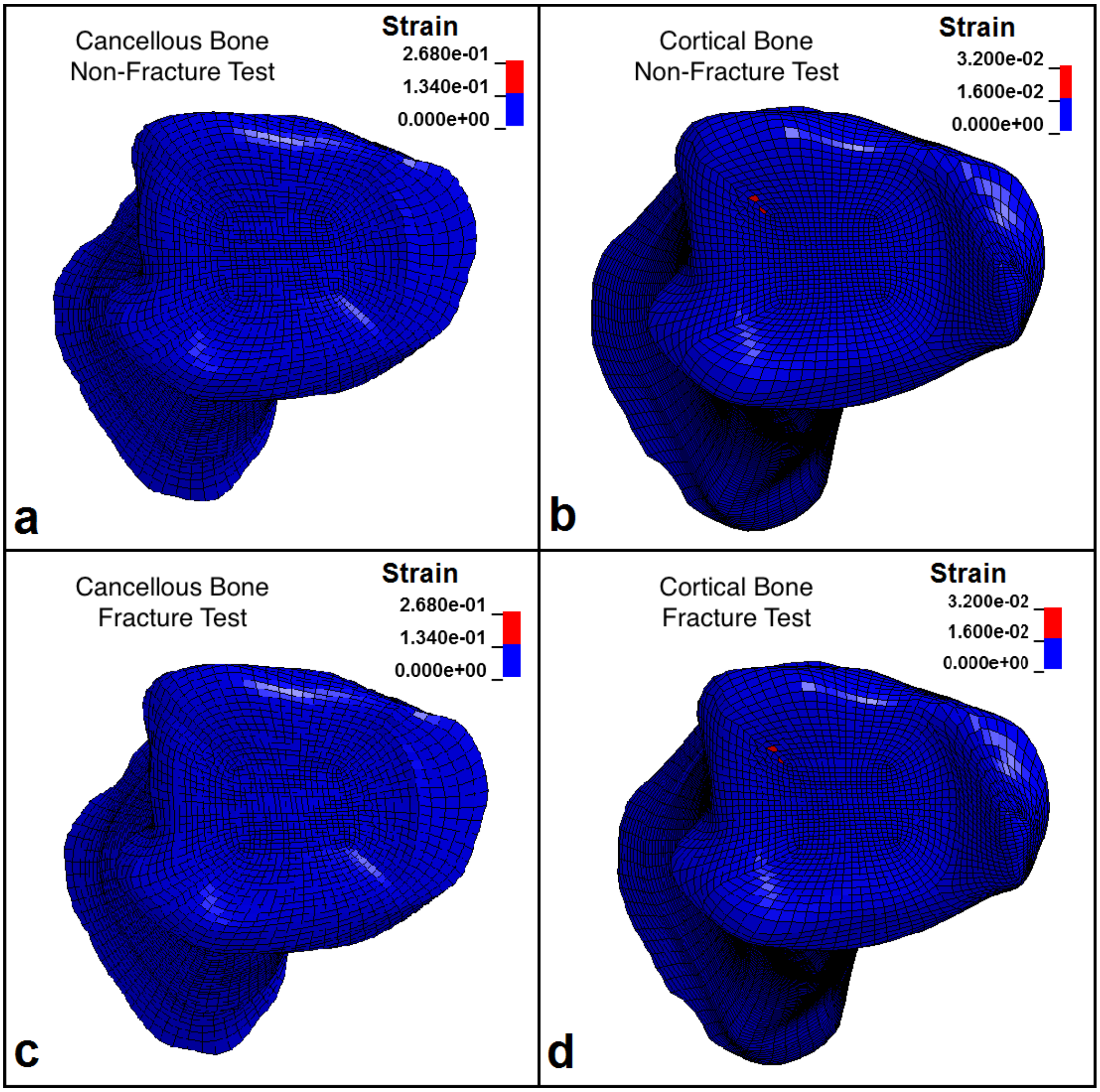

Figure 4.10: Maximum Principal Strain in the Higher-Rate Tests
The maximum principal strain shown for the two higher-rate tests in the **a)** cancellous bone for the non-fracture test; **b)** cortical bone for the non-fracture tests; **c)** cancellous bone for the fracture test; **d)** cortical bone for the fracture tests. The threshold for fracture was 0.134 for cancellous bone and 0.16 for cortical bone, with elements exceeding these values shown in red.

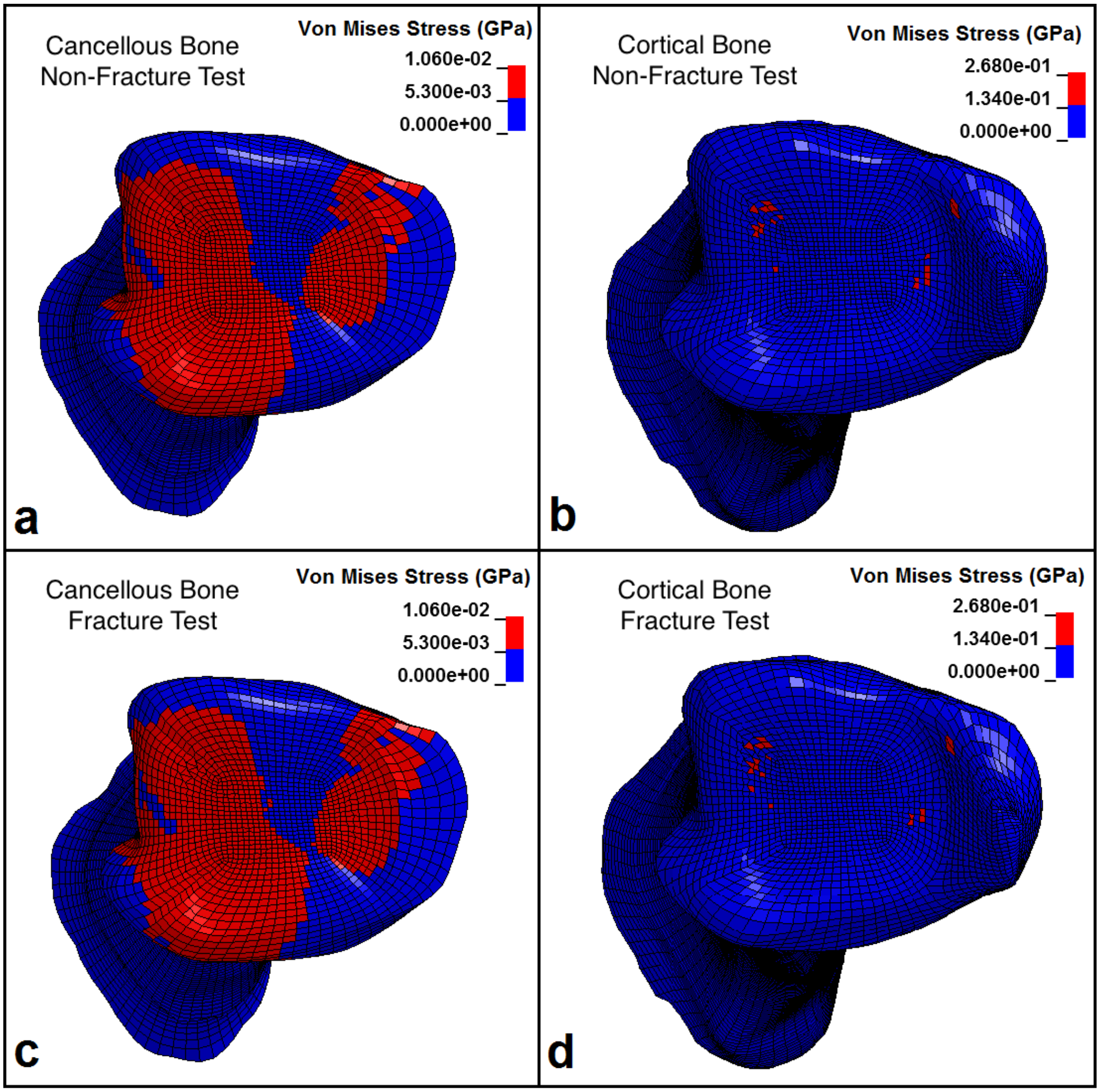

Figure 4.11: Von Mises Stress in the Higher-Rate Tests
The Von Mises stress shown for both the higher-rate tests in the **a)** cancellous bone for the non-fracture test; **b)** cortical bone for the non-fracture tests; **c)** cancellous bone for the fracture test; **d)** cortical bone for the fracture tests. The threshold for fracture was 5.3 MPa for cancellous bone and 134 MPa for cortical bone, with elements exceeding these values shown in red.

duration impacts was altered to represent impact loading of the tibia under different experimental conditions and events of varying durations.

In this study, load data from the FE model were compared to the results from cadaveric testing from a single donor. Due to the large degree of variability in terms of time to peak, duration, and general shape of the force-time curves seen across the donors used for cadaveric testing, force corridors and an averaged force-time curve to represent all donors could not be developed. As such, the most average donor was selected to verify the results of the computational model.

Accurate modelling of geometry is crucial to a FE model's success. The geometry and mass distribution of the components used for cadaveric testing in Chapter 3 were incorporated into this finite element model. Accurate representation of the physical contacts in the model is also crucial to its results. The contact friction that occurred at the interface between the impact bracket and the bearing rail was modelled through an iterative process using peak force values from the non-fracture tests for both the lower-rate and higher-rate test conditions. The peak force values from the fracture tests were not used since a FE model does not simulate the energy lost due to cracking during a fracture. The values used for frictional coefficients resulted in a static coefficient of friction that is greater than the kinetic coefficient of friction. Coefficient of friction values are often less for kinetic friction (Gross *et al.* 2013), so it is likely that this would also be the case during the experimental testing.

The peak force values achieved by the computational model were more aligned with cadaveric results in the non-injurious simulations (within 20% of experimental forces) than the injurious simulations (96% of fracture force was achieved in the higher-rate fracture test but only 73% was achieved in the lower-rate fracture test). It was expected that the results would be less consistent when evaluating injurious tests since the model does not simulate failure occurring in the tibia and its associated loss of energy due to fracture. However, these peak force relationships correspond to the model being compared to a single donor that was selected as being most representative of the six donors tested. When the peak force values were compared to the average peak force values across all donors from cadaveric testing, the model's results actually fell within the range of these values. Previous finite element studies corroborate their models by developing acceptable corridors for validation parameters such as peak force based on cadaveric testing, analogous in this work to the average peak fore across all donors. While the model had some degree of error when verifying its results to a specific donor, its results actually represented the average population tested experimentally in Chapter 3 quite well. Since the model was meant to represent the response of an average population, its ability to predict peak force during impact loading was considered to be successful. The previous study that developed the model of the isolated tibia (Quenneville and Dunning 2011a) showed that peak force was within 10% of the experimental values for all tests except the fracture test. However, the higher level of agreement in that study was expected since the computational results were evaluated against the results of the corresponding specimen in cadaveric testing.

The impact durations seen in the results of the simulation were larger than those seen experimentally. It is interesting to note that impact durations were better aligned in the non-fracture tests (27% for the lower-rate condition and 18% for the higher-rate condition) than for the fracture tests (33% for the lower-rate condition and 85% for the higher-rate condition). Impact durations were fairly inconsistent during injurious cadaveric tests since the deformation of the bone would lead to a sudden lack of contact against the talus. Since the model does not simulate bone fractures, these inconsistencies with injurious tests were expected. Impulse values were greater in the simulation than those seen experimentally for all four test conditions (between 5% and 130% greater). This was likely caused by the longer impact durations that the model showed.

The inaccuracies in terms of impact duration and peak force may be attributed to the modelling of the deformable sponge. The material properties of the sponge were determined through compressive testing using a material testing machine. Due to the limitations of this apparatus, the compression tests were conducted at a rate of 50 mm/min. This is magnitudes smaller than the loading rate of the deformable sponge during impact testing. It is likely that the stiffness of the sponge would vary depending on loading rate, and in reality, the sponge may be much stiffer when subjected to the load rates observed in cadaveric testing, as deformable sponges and foams typically have material properties that are strain-rate dependent (Saha *et al.* 2005). Since the deformable sponge was used to control the impact duration, and therefore the loading rate, accurate modelling of its material properties may have a great effect on the overall results of the FE model. While a rigorous investigation of the material properties of the deformable sponge was not within the scope of this work, better characterization may lead to a more accurate model, and could be a beneficial topic of future investigation.

The simulation's ability to predict fracture based on critical values for maximum principal strain and Von Mises stress was limited. Several tests resulted in failure being predicted in the non-fracture tests (Von Mises stress for both the lower-rate and higher-rate non-fracture tests in cancellous bone and Von Mises stress in the cortical bone region for the military non-fracture test). Overall, the fringe plots were indistinguishable between non-injurious and injurious tests. As such, the peak forces established by the model were determined to be as the best predictors of fracture based on injury risk curves produced in the previous cadaveric work. Also, in the previous model of the isolated tibia that used in this study (Quenneville and Dunning 2011a), maximum principal strain values were not capable of predicting areas of fracture, while the values for Von Mises stress were limited in their ability to predict fracture. The results of this model were therefore in agreement with those of the previous paper that developed the model of the isolated tibia.

A limitation of this work is the fact that the model was validated using experimental results from a bone that do not correspond to the tibia used in the simulation, and the material properties of this bone were taken from values from literature. The varied geometry and material properties within a given population can lead to a great range in injury tolerance. However, this previously validated model of the tibia was created with the intention of being representative of an average male, and its material properties correspond to values representative of an average male population. The donor that was selected to validate the model was also deemed the most average in terms of age and fracture forces for the sample of specimens available from cadaveric testing. Since the model was created with the purpose of being representative of an average male tibia and meant as a general tool that can respond within the natural range of this population, the use of the previously validated tibia mesh and its material properties was deemed acceptable. Another limitation of this work is that the frictional coefficients used to model the contact between the impact bracket and the bearing rail were determined through an iterative process in which values were only ranged by increments of 0.05. The frictional coefficients were also only varied up to values of 0.1 for both static and kinetic friction. Smaller increments and values greater than 0.1 for the fractional coefficients may lead to more accurate results in terms of the model's ability to match the peak forces seen in experimental testing.

There were several other limitations of this work, many of which are common in finite element models of bone. For computational purposes, the material properties of bone were simplified. The cancellous bone, cortical bone, and marrow were modelled as isotropic and homogeneous materials. In reality, these biological tissues are anisotropic and heterogeneous. The effects of strain rate on the material properties of cortical bone were modelled using a family of curves approach established by Untaroiu *et al.* (2004). This method provided stress-strain curves for cortical bone up to a strain rate of 1 s^{-1}. Any strain rates above this maximum rate defined used this curve. During dynamic loading, the bone was subjected to strain rates much larger than this (maximum strain rates seen in the FE model were 32.1 s^{-1} for the lower-rate automotive condition and 40.2 s^{-1} for the higher-rate military condition) and as such, providing the stress-strain curves beyond this strain rate would improve the cortical bone's response. In addition, the strain rate effects of cancellous bone were modelled using the Cowper-Symonds approach, which scales the yield stress of a material depending on the strain rate. The elastic modulus of the material however, does not get scaled in this approach. For these high-strain simulations, it is likely that the strain rate has a significant effect on the modulus of the material. The computational simulation in this work was subjected to a range of impact velocities greater than the previous work conducted to create the tibia model. For this reason, it is likely that the effects of strain rate on the tibia may be greater in this study. It would be of interest for future work to investigate the ability of the family of curves and Cowper-Symonds methods of modelling bone's strain rate dependencies under such a large difference of impact severities. This further investigation may improve the model's ability to predict fracture in the tibia under axial loading.

The work conducted in this chapter produced a FE model of the isolated tibia's response to dynamic axial loading at various rates. The computational model was subjected to varied impact severities (mainly in terms of impact velocity) that has not previously been seen in lower leg axial loading simulations. For this reason, the results of this work can be applied to impact scenarios of various loading rates, including both automotive and military loading conditions. While there are several challenges to simulating this type of loading that are apparent in this work, this model's prediction of force is promising. This model will serve as a beneficial general tool in future works to assess the tibia's risk of injury under automotive and military loading scenarios, and to evaluate the effect of protective systems on fracture risk.

CHAPTER 5 – GENERAL DISCUSSION AND CONCLUSIONS

Overview: *This chapter reviews the objectives and hypotheses established in Chapter 1, and a summary of the main outcomes of the experimental and computational work and their relevance to injury evaluations are provided. The overall limitations and strengths of this work are presented, and future directions are analyzed.*

5.1 Summary

The tibia is a frequent site of injury during frontal automotive collisions and military underbody blasts. During these scenarios, loads are transferred from the vehicle's floor or footplate to the occupant via the plantar surface and through the leg. While these two scenarios cause comparable injuries by means of a similar loading mechanism, the loading rate differs substantially between the two scenarios. The majority of experimental testing that has been previously done to determine the axial injury tolerance of the tibia has been conducted by the automotive industry. Less work has been done to determine the injury tolerance of the tibia during higher rate military loading events, and thus far, no known studies have varied the loading rate of axial impacts to directly study its effect. Prior to the current work, whether injury thresholds developed for automotive impacts could be applied to higher rate military blasts remained to be investigated.

The overall purpose of this study was to directly study the effect of loading rate on the axial fracture tolerance of the isolated tibia to develop injury thresholds that can be applied to the automotive and military loading scenarios investigated.

The first step to accomplish this was to design and implement the electronic instrumentation required to operate the pneumatic impacting apparatus at the Injury Biomechanics Laboratory at McMaster University, and to collect data during its use (*i.e.*, Objective 1, Chapter 2). The pneumatic impacting apparatus featured a solenoid valve, and the lab was equipped with a high-speed camera, both of which required synchronized triggering. In terms of sensors to quantify the impact and its effect on the bone specimen, a load cell, accelerometer, strain gauges, and photoelectric sensors were carefully selected and mounted to the specimen and test chamber. The data produced by these sensors needed to be acquired and synchronized into a single program. A LabVIEW® program was created that triggered the experiment apparatus, high-speed camera, and collected synchronized data across all instrumentation, and the necessary sensor circuits were organized into a single electronics box.

The pneumatic impactor was used to conduct impacts on six pairs of isolated tibia specimens to investigate the axial fracture tolerance of the tibia (*i.e.*, Objective 2, Chapter 3). Two impact conditions were simulated, a lower-rate automotive collision and a higher-rate military blast, based on velocity and impact duration values reported in literature for these loading incidents. The tibia was found to have a larger injury limit during impacts with higher velocities and shorter impact durations (*i.e.*, higher loading rate), like those seen in military blasts, than during lower rate impacts, like those that occur in frontal automotive collisions (*i.e.,* Hypothesis 1 accepted). The Hybrid III and MIL-LX lower leg anthropomorphic test devices (ATDs) were subjected to similar impact conditions (*i.e.,* Objective 3, Chapter 3) as the isolated tibia specimens, to identify limits that should be used during safety evaluations using these tools. Forces measured by the Hybrid III were much greater than those measured with cadaveric testing, due to the overly high stiffness of this surrogate. The MIL-LX's ability to measure forces corresponded much better with results from cadaveric testing. This work showed that the MIL-LX leg can be used for accurate injury prediction during impacts with ranging loading rates, while the Hybrid III leg cannot (*i.e.,* Hypothesis 2 accepted).

The results from cadaveric impact testing were used to create a finite element (FE) model of the lower leg. Using a previously developed model of the isolated tibia (Quenneville and Dunning 2011a), a model was created that simulated the experimental testing from Chapter 3 (*i.e.,* Objective 4, Chapter 4). By adjusting the projectile's initial velocity and mass to corresponding values from experimental testing, the model was subjected to four impacts: a non-fracture and a fracture test for each of the lower-rate automotive and higher-rate military test conditions. The model's ability to predict injury was assessed by comparing its force-time curves to those seen in an average specimen and using critical Von Mises stress and maximum principal strain thresholds from literature. The model's ability to predict regions of fracture was fairly limited, as fringe plots created based on Von Mises stress and maximum principal stress were difficult to differentiate between non-fracture and fracture tests (*i.e.,* Hypothesis 3 rejected). However, the simulations ability to match the cadaveric force-time curves was more promising. The model's peak force values were within 20% of experimental values for the non-fracture cases, and within 27% for the fracture cases. Results from future studies using this model can therefore be used as a general indicator of the force produced at the tibia during an axial impact, and the boundary conditions of the model can be easily altered to test a variety of impact conditions.

5.2 Limitations and Strengths

Specific strengths and limitations were discussed in detail in each chapter; however, some of these general remarks apply to the full scope of this work.

One of the limitations of this work was the lack of soft tissue, ankle, foot, and muscle tension in the specimens. This does not represent the conditions of a person in a real-life loading scenario and could have an effect on the load path through the lower leg. However, the fibula is not a major load bearing bone in the leg, and efforts were made to match the inertial characteristics of the missing components through the use of ballast mass and to match the loading pattern through the ankle with the artificial talus. While results are not representative of full lower leg injury risk, as the calcaneus or tibia may be more vulnerable, it is likely that the rate-dependence identified in the tibia could be equally applied to these bones. The lack of foot and ankle in the cadaveric testing also meant that testing of the ATDs had to occur without their corresponding foot and ankle parts, which would likely have an effect on their force measurements. Due to the limits of the load cells, ATD comparison had to be done through interpolation, which may not completely accurate. Only two conditions were tested with the ATDs (an automotive and military condition), meaning that extrapolation to other load rates (*e.g.,* a blast impact but with an energy attenuating floor mat) may be challenging to implement. Another limitation of this work was the use of repeated testing, which may have caused accumulated damage to the specimen. Repeated testing was required to determine the force required to achieve fracture with a higher degree of precision, and given that the two bones that fractured on their first impacts were within the force range of the other specimens, it is likely this didn't have a substantial influence on the outcomes of this work.

The donor that was used to create the geometry of the finite element model did not correspond to the donor that was used during experimental testing to validate the model. However, the donor that was used to create the bone mesh was representative of an average male, and was compared to data from the most average donor from the current experimental tests, and as such this was determined to be an appropriate representation of a general injury assessment model. Lastly, the results in terms of peak force and impact duration of the finite element model were heavily dependent on the mechanical behaviour of the deformable sponge in the simulation. The material properties of the sponge were determined during a compression test using a material's testing machine; however, due to that device's limitations, the sponge was tested at strain rates much smaller than those that were seen during experiments. A more rigorous evaluation of the sponge's material properties would certainly improve the finite element model's results.

While the lack of foot and ankle may have influenced the application of loading to the tibia, the use of isolated tibias was seen as an advantage since it eliminated the number of degrees of freedom and allowed for better control of the load application during testing. The rationale for using isolated bone specimens was that the results from this work could be extrapolated for use in injury risk prediction in other bones of the body. Using paired specimens from the same donor allowed for direct comparison of results between the two testing conditions, something that has not been done in previous studies. This eliminated the variability in both geometry and bone mechanical properties that are often seen in a population that can have a significant effect on material testing of bone specimens. Using the pneumatic testing apparatus and deformable sponge, the velocity and impact duration values matched those reported in the literature for frontal automotive collisions and military underbody blasts. This is the first study to directly target both of these values during impact testing. The same conditions (at lower severity levels due to the limits of the load cells in the ATDs) that were used during cadaveric testing were also replicated during testing of the ATD legs, which allowed for direct comparison of their response to that of the cadaveric tibia that led to appropriate injury limits being defined for these common yet overly stiff tools. While cadaveric testing was used to determine the injury limits of the tibia under these loading conditions, the development of a finite element model allows for future assessment of protective systems without having to conduct extensive experimental testing with biological tissues. One of the major strengths of this computational model and this work as a whole was the wide range in severity, mainly in terms of velocity, of the impact conditions used to evaluate the model, which is typically not seen in previous studies.

5.3 Future Directions

Great efforts were made to create a triaxial accelerometer and fixture to measure accelerations directly on the tibia specimens during dynamic loading with the goal of developing a new method for generating injury limits. While this system was successfully validated, there were several issues with the system once it was implemented during dynamic loading. Mainly due to its large geometry, the alignment fixture that was created proved complicated to mount onto bone, and the system failed mechanically after several impacts. Since forces in the mediolateral direction were negligible during loading, simply mounting a dual-axis accelerometer onto the bone might provide the adequate accelerometer measurements and would make the process much simpler. This would provide acceleration values in the anterior-posterior and proximal-distal directions in the tibia, which would be an interesting factor to study in terms of injury prediction that has not been seen previously in the literature and would provide a point of direct comparison to ATDs that measure acceleration values.

Previous studies of the lower leg have shown that the complex loading through the ankle plays a crucial part in injury risk in this area. Now that the effect of load rate of the fracture tolerance of the tibia has been identified and the differences between fracture tolerances between lower-rate and higher-rate loading scenarios have been shown, it would be interesting to conduct impact testing in these two conditions using full lower leg specimens. In doing so, the realistic load path through the foot and ankle can be replicated experimentally, and fractures that may have occurred at other bones in this area (*i.e.*, calcaneus and talus) can be documented.

One of the major challenges during the finite element (FE) model development was the accurate material modelling of the strain rate effects of cortical and cancellous bone. The model that was created included a previously-validated tibia, and maintained the properties previously used to define its strain rate dependence. However, one of the new developments of the FE model created in this work was the investigation of its response to varied impact severities. It would be of interest to study the family of curves and Cowper-Symonds methods for scaling the properties of bone throughout a range of strain rates over the severities employed. In order to create a FE model that truly matches the cadaveric conditions tested, further examination of the material properties of the deformable sponge is also required. One of issues with the FE model was the fact that it did not simulate bone fractures and its associated energy losses. The material models currently available to represent fracture are limited. As such, further investigation of a material model that simulates fracture would certainly improve the current model's response, especially in the fracture cases that were conducted.

5.4 Significance

This work represents the first study to directly investigate the effect of loading rate on the axial fracture tolerance of the lower leg and compare this fracture tolerance during an automotive collision and a military blast. The effect of loading rate on bone's fracture tolerance was shown, as well as the fact that the current single force limit being applied to these various events is not adequate. New force thresholds were developed for both of these scenarios. The same loading conditions were tested using ATDs to evaluate their injury prediction and produce limits that can be used by industry, giving real-world relevance to this study. The finite element model that was developed can be used to simulate high-rate loading and assess injury risk in future studies. It is hoped that the results from this work will be used to evaluate and design safety mechanisms in automotive and military vehicles, with the goal of reducing injuries to the lower leg. The work that was done in terms of electronics and instrumentation for the pneumatic apparatus will be used by future researchers conducting experiments at the Injury Biomechanics Laboratory at McMaster University.

References

Bailey, A.M., McMurry, T.L., Poplin, G.S., Salzar, R.S., and Crandall, J.R., 2015. Survival model for foot and leg high rate axial impact injury data. *Traffic Injury Prevention*, 16 Suppl 2, S96–S102.

Belwadi, A., Siegel, J.H., Singh, A., Smith, J.A., Yang, K.H., and King, A.I., 2012. Finite Element Aortic Injury Reconstruction of Near Side Lateral Impacts Using Real World Crash Data. *Journal of Biomechanical Engineering*, 134 (1), 11006.

Bir, C., Barbir, A., Dosquet, F., Wilhelm, M., van der Horst, M., and Wolfe, G., 2008. Validation of lower limb surrogates as injury assessment tools in floor impacts due to anti-vehicular land mines. *Military Medicine*, 173 (12), 1180–1184.

Burgess, A.R., Dischinger, P.C., O'Quinn, T.D., and Schmidhauser, C.B., 1995. Lower extremity injuries in drivers of airbag-equipped automobiles: Clinical and crash reconstruction correlations. *The Journal of Trauma: Injury, Infection, and Critical Care*, 38 (4), 509–516.

Burkhart, T.A., Dunning, C.E., and Andrews, D.M., 2012. Predicting distal radius bone strains and injury in response to impacts using multi-axial accelerometers. *Journal of Biomechanical Engineering*, 134 (10), 101007.

Carpanen, D., Masouros, S., and Newell, N., 2016. Surrogates of Human Injury. *In*: A.M.J. Bull, J.C. Clasper, and P.F. Mahoney, eds. *Blast Injury Science and Engineering*. Springer International Publishing, 189–198.

Crandall, J.R., Martin, P.G., Sieveka, E.M., Pilkey, W.D., Dischinger, P.C., Burgess, A.R., O'Quinn, T.D., and Schmidhauser, C.B., 1998. Lower limb response and injury in frontal crashes. *Accident Analysis and Prevention*, 30 (5), 667–677.

Dischinger, P.C., Read, K.M., Kufera, J.A., Kerns, T.J., Burch, C.A., Jawed, N., Ho, S.M., and Burgess, A.R., 2004. Consequences and costs of lower extremity injuries. *Annual Proceedings / Association for the Advancement of Automotive Medicine*, 48, 339–53.

Dong, L., Zhu, F., Jin, X., Suresh, M., Jiang, B., Sevagan, G., Cai, Y., Li, G., and Yang, K.H., 2013. Blast effect on the lower extremities and its mitigation: A computational study. *Journal of the Mechanical Behavior of Biomedical Materials*, 28, 111–124.

Duffy, C., 2015. Analysis of Dynamic Impact on the Foot / Ankle Complex During a Vehicular Collision Through Finite Element Modelling. McMaster University.

Freescale Semiconductor, 2009. *MMA2202 Surface Mount Micromachined Accelerometer*. Data Sheet: Technical Data.

Funk, J.R., Crandall, J.R., Tourret, L.J., MacMahon, C.B., Bass, C.R., Patrie, J.T., Khaewpong, N., and Eppinger, R.H., 2002. The axial injury tolerance of the human foot/ankle complex and the effect of Achilles tension. *Journal of Biomechanical Engineering*, 124 (6), 750–757.

Gallenberger, K., Yoganandan, N., and Pintar, F.A., 2013. Biomechanics of foot/ankle trauma with variable energy impacts. *Annals of Advances in Automotive Medicine. Scientific Conference*, 57, 123–32.

Griffin, L. V, Harris, R.M., Hayda, R.A., and Rountree, M.S., 2001. Loading rate and torsional moments predict pilon fractures for antipersonnel blast mine loading. *International IRCOBI Conference on the Biomechanics of Impacts, Isle of Man (UK)*, 115–131.

Gross, D., Hauger, W., Schröder, J., Wall, W.A., and Rajapakse, N., 2013. Static and Kinetic Friction. *In*: *Engineering Mechanics 1*. Berlin, Heidelberg: Springer, pp 259-283.

Hamill, J. and Knutzen, K.M., 2003. Articular Cartilage. *In*: P.J. Darcy, ed. *Biomechanical Basis of Human Movement*. Baltimore, MD: Lippincott Williams & Wilkins, 48–49.

Helfet, D.L., Koval, K., Pappas, J., Sanders, R.W., and DiPasquale, T., 1994. Intraarticular 'pilon' fracture of the tibia. *Clinical Orthopaedics and Related Research*, (298), 221–8.

Henderson, K.A., Bailey, A.M., Christopher, J.J., Brozoski, F., and Salzar, R.S., 2013. Biomechanical response of the lower leg under high rate loading. *IRCOBI Conference 2013*, 145–157.

Humanetics Innovative Solutions, 2015a. MIL-LX Legs [online]. *Aerospace & Military Crash Test Dummies*. Available from: http://www.humaneticsatd.com/crash-test-dummies/aerospace-military/mil-lx-legs [Accessed 7 Sep 2016].

Humanetics Innovative Solutions, 2015b. Hybrid III 50th Male Dummy [online]. *Frontal Impact Crash Test Dummies*. Available from: http://www.humaneticsatd.com/crash-test-dummies/frontal-impact/hybrid-iii-50th [Accessed 7 Sep 2016].

Huston, R.L., 2009. *Principles of Biomechanics*. 1st ed. Boca Raton, FL: CRC Press.

Iwamoto, M., Miki, K., and Tanaka, E., 2005. Ankle skeletal injury predictions using anisotropic inelastic constitutive model of cortical bone. *49th Stapp Car Crash Conference*.

Jacob, N., Amin, A., Giotakis, N., Narayan, B., Nayagam, S., and Trompeter, A.J., 2015. Management of high-energy tibial pilon fractures. *Strategies in Trauma and Limb Reconstruction*, 10 (3), 137–147.

Kitagawa, Y., Ichikawa, H., King, A.I., and Levine, R.S., 1998. A severe ankle and foot injury in frontal crashes and its mechanism. *42nd Stapp Car Crash Conference Proceedings*, 983145, 14.

Klopp, G.S., Crandall, J.R., Hall, G.W., Pilkey, W.D., Hurwitz, S.R., and Kuppa, S.M., 1997. Mechanisms of injury and injury criteria for the human foot and ankle in dynamic axial impacts to the foot. *1997 IRCOBI Conference*, 73–86.

Kuppa, S., Wang, J., Haffner, M., and Eppinger, R.H., 2001. Lower extremity injuries and associated injury criteria. *In*: *Proceedings of the 17th International Technical Conference on Enhanced Safety of Vehicles Paper 457*. Amsterdam, Netherlands.

LSTC, 2015. *LS-DYNA Keyword User’s Manual*. Livermore, CA, USA.

Martini, F.H., Timmons, M.J., and Tallitsch, R.B., 2009. *Human Anatomy*. 6th ed. San Francisco: Pearson Benjamin Cummings.

McKay, B.J. and Bir, C.A., 2009. Lower extremity injury criteria for evaluating military vehicle occupant injury in underbelly blast events. *Stapp Car Crash Journal*, 53 (November), 229–249.

Mertz, H.J., 1993. Anthropomorphic Test Devices. *In*: *Accidental Injury*. New York, NY: Springer New York, 66–84.

Morgan, R., Eppinger, R., and Hennessey, B., 1991. Ankle joint injury mechanism for adults in frontal automotive impact. *35th Stapp Car Crash Conference Proceedings*, 10.

National Highway Traffic Safety Administration, 2016. *2015 Motor Vehicle Crashes: Overview*. Traffic Safety Facts: Research Note. Washington, DC.

North Atlantic Treaty Organization, 2011. *Procedures For Evaluating the Protection Level of Armoured Vehicles*. Allied Engineering Publication 55.

North Atlantic Treaty Organization HFM-090 Task Group 25, 2007. *Test methodology for protection of vehicle occupants against anti-vehicular landmine effects*. France: Research and Technology Organisation.

Owen, C. and Lowne, R., 2001. Requirements for the evaluation of the risk of injury to the ankle in car impact tests. *17th International Technical Conference on the Enhanced Safety of Vehicles in Amsterdam*, 1–12.

Pandelani, T., Sono, T.J., Reinecke, J.D., and Nurick, G.N., 2015. Impact loading response of the MiL-Lx leg fitted with combat boots. *International Journal of Impact Engineering*, 92, 26–31.

Pattimore, D., Ward, E., Thomas, P., and Bradford, M., 1991. The nature and cause of lower limb injuries in car crashes. *35th Stapp Car Crash Conference Proceedings*, 912901, 20.

Quenneville, C.E., 2016. High-Speed Impact Testing and Injury Assessment of Whole Bones. *In*: R. Zdero, ed. *Experimental Methods in Orthopaedic Biomechanics*. London, UK: Elsevier Publishing, PP 3-17.

Quenneville, C.E. and Dunning, C.E., 2011a. Development of a finite element model of the tibia for short-duration high-force axial impact loading. *Computer Methods in Biomechanics and Biomedical Engineering*, 14 (2), 205–212.

Quenneville, C.E. and Dunning, C.E., 2011b. Evaluation of energy attenuating floor mats for protection of lower limbs from anti-vehicular landmines. *Journal of Battlefield Technology*, 14 (3), 4–7.

Quenneville, C.E. and Dunning, C.E., 2012. Evaluation of the biofidelity of the HIII and MIL-Lx lower leg surrogates under axial impact loading. *Traffic Injury Prevention*, 13 (1), 81–85.

Quenneville, C.E., Fraser, G.S., and Dunning, C.E., 2010. Development of an apparatus to produce fractures from short-duration high-impulse loading with an application in the lower leg. *Journal of Biomechanical Engineering*, 132 (January 2010), 14502.

Quenneville, C.E., McLachlin, S.D., Greeley, G.S., and Dunning, C.E., 2011. Injury tolerance criteria for short-duration axial impulse loading of the isolated tibia. *The Journal of Trauma*, 70 (1), E13–E18.

Ramasamy, A., Hill, A.M., Masouros, S., Gibb, I., Phillip, R., Bull, A.M.J., and Clasper, J.C., 2013. Outcomes of IED foot and ankle blast injuries. *The Journal of Bone and Joint Surgery*, 95 (5), e25.

Ramasamy, A., Hill, A.M., Phillip, R., Gibb, I., Bull, A.M.J., and Clasper, J.C., 2011a. The modern 'deck-slap' injury—calcaneal blast fractures from vehicle explosions. *The Journal of Trauma: Injury, Infection, and Critical Care*, 71 (6), 1694–1698.

Ramasamy, A., Masouros, S.D., Newell, N., Hill, A.M., Proud, W.G., Brown, K.A., Bull, A.M.J., and Clasper, J.C., 2011b. In-vehicle extremity injuries from improvised explosive devices: current and future foci. *Philosophical Transactions of the Royal Society of London B: Biological Sciences*, 366, 160–170.

Saha, M.C., Mahfuz, H., Chakravarty, U.K., Uddin, M., Kabir, M.E., and Jeelani, S., 2005. Effect of density, microstructure, and strain rate on compression behavior of polymeric foams. *Materials Science and Engineering: A*, 406 (1), 328–336.

Sapuan, S.M., Osman, M.R., and Nukman, Y., 2006. State of the art of the concurrent engineering technique in the automotive industry. *Journal of Engineering Design*, 17 (2), 143–157.

Seipel, R.C., Pintar, F.A., Yoganandan, N., and Boynton, M.D., 2001. Biomechanics of calcaneal fractures: A model for the motor vehicle. *Clinical Orthopaedics & Related Research*, (388), 218–224.

Semiconductor, F. and Freescale Semiconductor, 2012. *MMA3202 Surface Mount Micromachined Accelerometer*. Data Sheet: Technical Data.

Shin, J., Yue, N., and Untaroiu, C.D., 2012. A finite element model of the foot and ankle for automotive impact applications. *Annals of Biomedical Engineering*, 40 (12), 1–13.

Smith, B.R., Bageman, P.C., Leland, R., Meehan, R., Levine, R.S., Yang, K.H., and King, A.I., 2005. A mechanism of injury to the forefoot in car crashes. *Traffic Injury Prevention*, 6 (2), 156–169.

Takahashi, Y., Kikuchi, Y., Konosu, A., and Ishikawa, H., 2000. Development and validation of the finite element model for the human lower limb of pedestrians. *Stapp car crash journal*, 44, 335–55.

Takebe, K., Nakagawa, A., Minami, H., Kanazawa, H., and Hirohata, K., 1984. Role of the fibula in weight-bearing. *Clinical Orthopaedics and Related Research*, (184), 289–92.

Taylor, A., Morris, A., Thomas, P., and Wallace, A., 1997. Mechanisms of lower extremity injuries to front seat car occupants - An in depth accident analysis. *1997 IRCOBI Conference*, 53–72.

Untaroiu, C., Darvish, K., Crandall, J., Deng, B., and Wang, J., 2005. A finite element model of the lower limb for Simulating pedestrian impacts. *Stapp Car Crash Journal*, 49 (November), 1–26.

Untaroiu, C., Darvish, K., Crandall, J., Deng, B., and Wang, J.T., 2004. Development and validation of a finite element model of the lower limb. *Proceedings of IMECE04*, 1–10.

Untaroiu, C.D., Ivarsson, J., Genovese, D.R., Bose, D., and Crandall, J.R., 2008. Biomechanical injury response of leg subjected to combined axial compressive and bending loading. *Biomedical Sciences Instrumentation*, 44, 141–6.

Untaroiu, C.D., Yue, N., and Shin, J., 2013. A finite element model of the lower limb for simulating automotive impacts. *Annals of Biomedical Engineering*, 41 (3), 513–526.

Wang, J., Bird, R., Swinton, B., and Krstic, A., 2001. Protection of lower limbs against floor impact in army vehicles experiencing landmine explosion. *Journal of Battlefield Technology*, 4 (3), 8–12.

Whiting, W.C. and Zernicke, R.F., 1998. Chapter 6: Lower-Extremity Injuries. *In*: *Biomechanics of Musculoskeletal Injury*. Human Kinetics, 350.

Yoganandan, N., Arun, M.W.J., Pintar, F.A., and Szabo, A., 2014. Optimized lower leg injury probability curves from postmortem human subject tests under axial xmpacts. *Traffic Injury Prevention*, 15, S151–S156.

Yoganandan, N., Pintar, F.A., Kumaresan, S., and Boynton, M.D., 1997. Axial impact biomechanics of the human foot-ankle complex. *Journal of Biomechanical Engineering*, 119 (4), 433–7.

Yoganandan, N., Pintar, F. a, Boynton, M.D., Begeman, P., Prasad, P., Kuppa, S.M., Morgan, R.M., and Eppinger, R.H., 1996. Dynamic axial tolerance of the human foot-ankle complex. *Society of Automotive Engineers, Inc.*, 962426, 207–218.

Appendix A: Glossary of Medical Terms

anterior	Situated near or toward the front of the body in anatomical position
articulation	The juncture between two bones in the skeleton of a vertebrate
biofidelity	Ability to accurately represent the natural biological response
cadaveric	Of, or pertaining to, a dead body
cancellous bone	Spongy tissue of bone found at the ends of long bones
cartilage	Connective tissue found in the articulating surfaces of joints, allows low-friction movement and distributes loads
contralateral	Pertaining to the other side of the body
cortical bone	Dense, rigid tissue of bone that surrounds the internal cavity of bones
diaphysis	The shaft or central part of a long bone
distal	Situated away from the centre of the body or from the point of attachment
epiphysis	The articular end part of a long bone, made of cancellous bone surrounded by a cortical shell
fibula	The outer and smaller of the two bones between the knee and the ankle, parallel with the tibia
in vivo	Latin for “within the living”, meaning taking place within a living organism
lateral	The side of the body or a body part that is farther from the middle or centre of the body
malleolus	The bony protuberance on either side of the ankle, at the lower end of the fibula or of the tibia
medial	Situated near the median plane of the body
plafond	The distal articular surface of the tibia which articulates with the talus at the ankle
plantar	Of, or relating to, the sole of the foot

posterior	Situated near or toward the back of the body in anatomical position
proximal	Situated nearer to the centre of the body or the point of attachment
shank	The part of the lower extremity between the knee and ankle
talus	Bone in the ankle that articulates with the tibia of the shank and the calcaneus and navicular bone of the foot
tibia	The larger bone of the lower leg, extending between the knee and the ankle
tibial plateau	The proximal articular surface of the tibia which articulates with the femur at the knee

Appendix B: Strain Gauge Application Procedure

The following technique was used to apply strain gauges directly to the cadaveric bone specimens. It was developed based on previous studies on attaching strain gauges to bone (Finlay et al., 1982; Wright and Hayes, 1979). All supplies were purchased from Tokyo Sokki Kenkyujo (Tokyo, Japan).

1. Use a scalpel to remove any soft tissue on the area where the strain gauge is to be attached.
2. Sand the surface of the bone directly where the strain gauge is to be attached using 400 grit sandpaper. Rub the area with an alcohol pad to degrease.
3. Apply 2 drops of CN cyanoacrylate adhesive to the area and press into a thin layer using finger pressure and tape. Remove finger pressure after 1 minute.
4. Let sit for 5 minutes.
5. Remove the tape and sand evenly again with 400 grit sandpaper. Wipe again with alcohol pad.
6. Place the strain gauge on the clean surface and press a piece of installation tape onto top. Use the tape to pick up the gauge.
7. Align the strain gauge and apply 1 drop of CN cyanoacrylate adhesive to the attachment site. Press down evenly and hold down finger pressure for 1 minute, pressing on all corners of the gauge.
8. Let sit for 5 minutes, remove tape.
9. Apply a coating of clear nail polish to the gauge and lead wire attachment points.

10. Let sit for 5 minutes.
11. To provide strain relief in the cables, use a zip tie to secure the wires to the bone, approximately 5 cm from the strain gauge.

References

Finlay, J. B., Bourne, R. B., & McLean, J. (1982). A technique for the in vitro measurement of principal strains in the human tibia. *Journal of Biomechanics*, *15*, 723–729.

Wright, T. M., & Hayes, W. C. (1979). Strain gage application on compact bone. *Journal of Biomechanics*, *12*, 471–475.

Appendix C: Technical Drawings

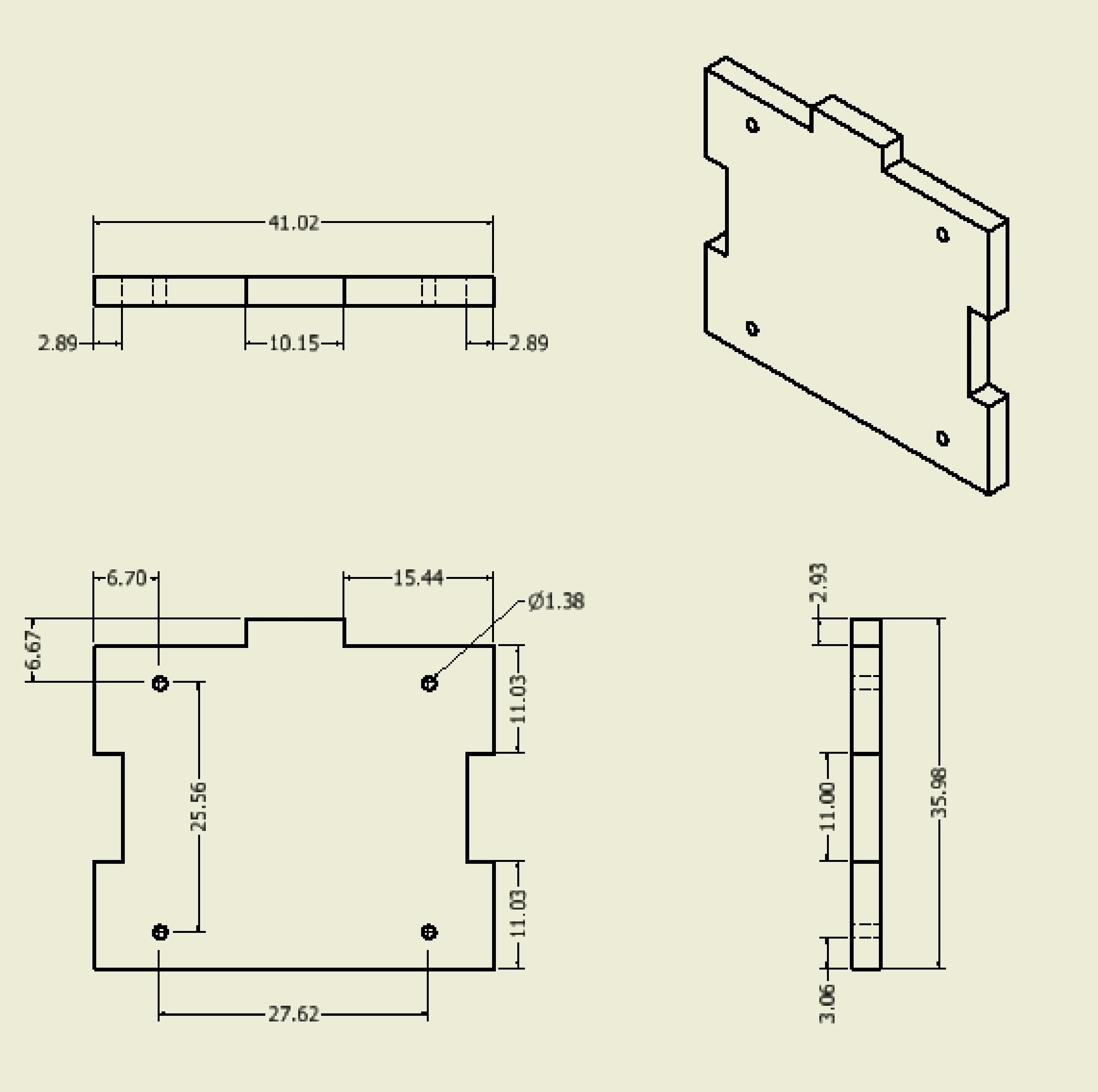

Figure C.1: Dual-Axis Accelerometer Plate for Alignment Fixture
All dimensions in mm, made of 3 mm thick acrylic.

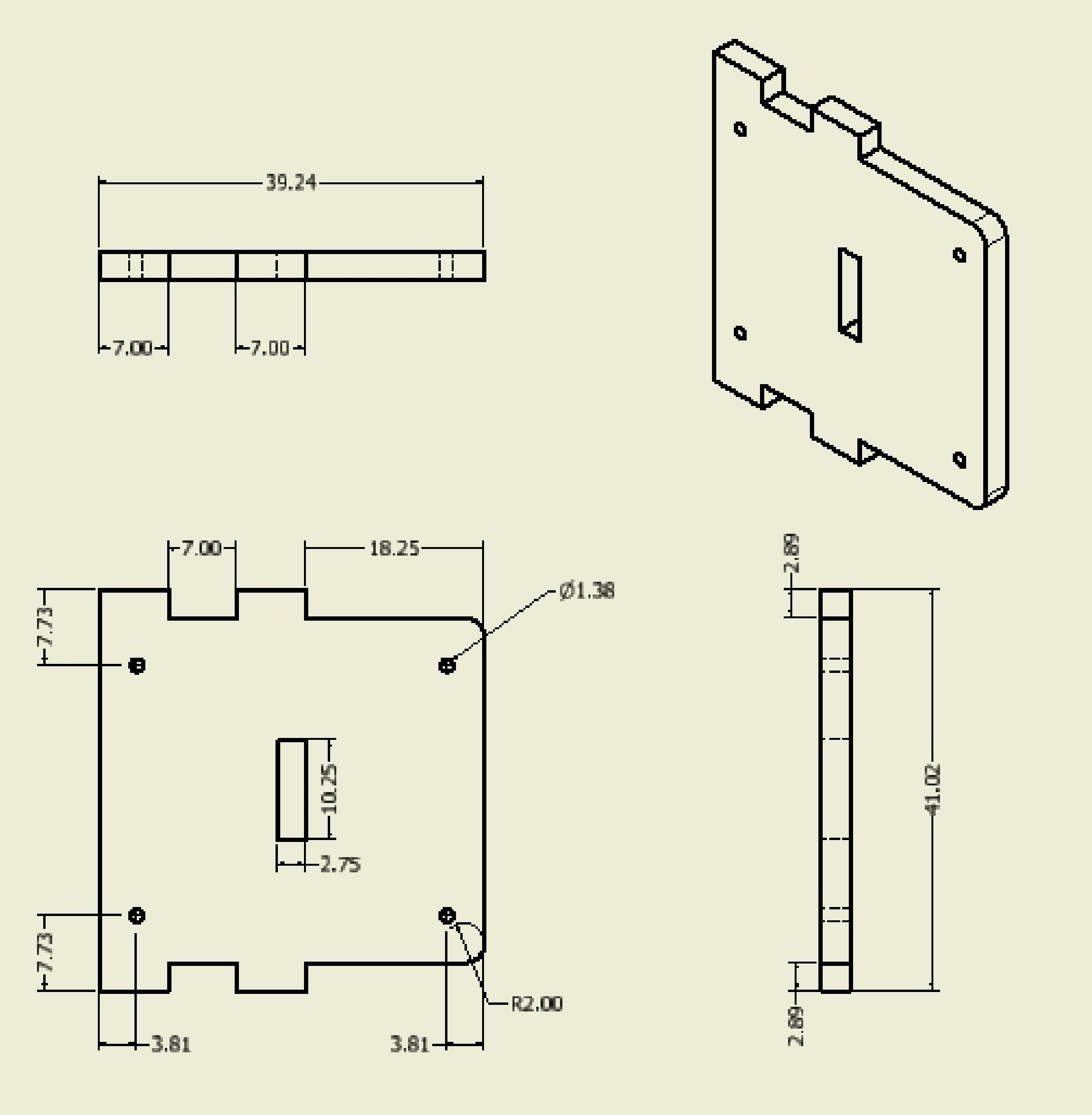

Figure C.2: Uniaxial Plate for Accelerometer Alignment Fixture
All dimensions in mm, made of 3 mm thick acrylic.

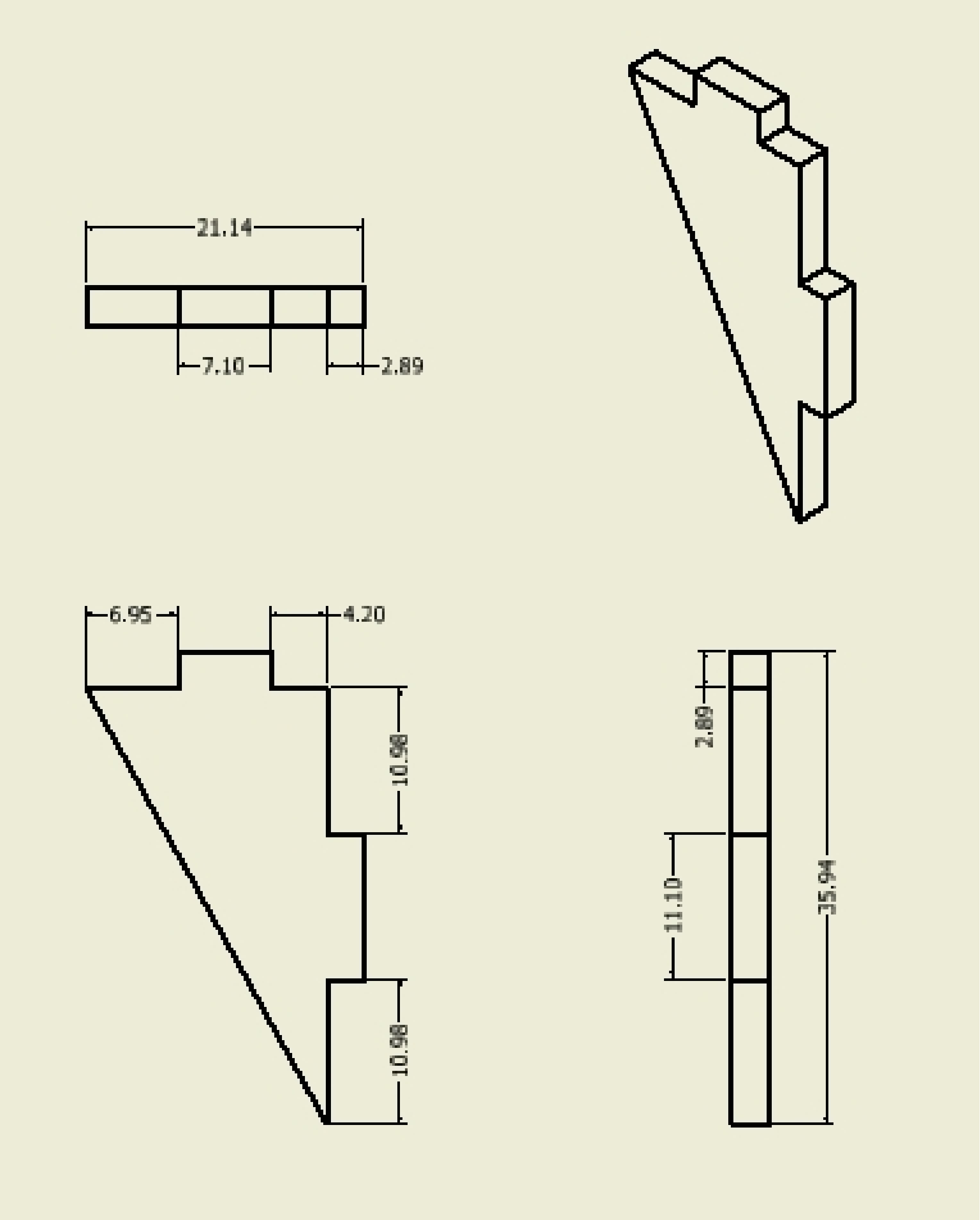

Figure C.3: Gusset Plate for Accelerometer Alignment Fixture
All dimensions in mm, made of 3 mm thick acrylic.

Appendix D: Electrical Circuits

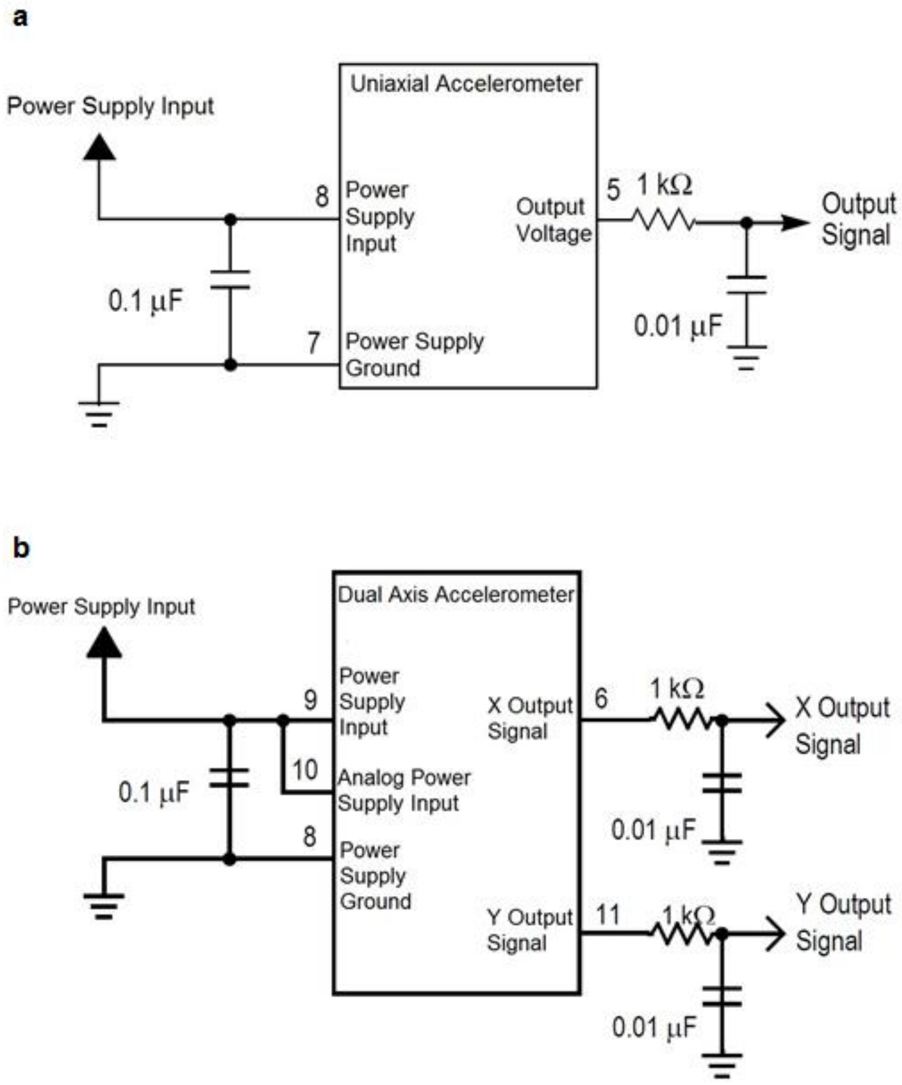

Figure D.1: Accelerometer Circuits
The circuits used to collect measurements from the accelerometers, as per manufacturer's recommendations. The circuits included a 0.1 μF capacitor placed between the power source and ground to decouple the power source, a 1 kΩ resistor and a 0.01 μF capacitor on the accelerometer outputs. A 5 VDC power supply was used for both the **a)** uniaxial accelerometers, adapted from Freescale Semiconductor (2009) and **b)** dual-axis accelerometer. Output signals were connected to the data acquisition system as analog inputs, adapted from Freescale Semiconductor (2012).

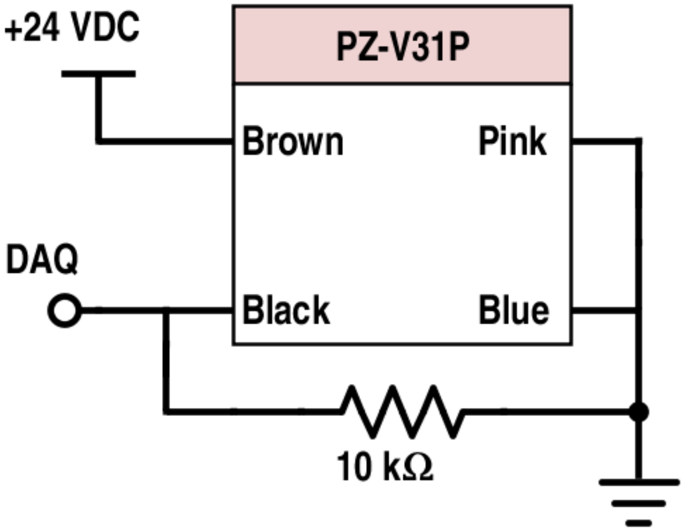

Figure D.2: Photoelectric Sensors Circuit
The circuit used to power the two photoelectric sensors that were used to create a velocity sensor. A 24 V power supply was used to supply power to the sensors.

References

Freescale Semiconductor, 2009. MMA2202 Surface Mount Micromachined Accelerometer. Data Sheet: Technical Data.

Freescale Semiconductor, 2012. MMA3202 Surface Mount Micromachined Accelerometer. Data Sheet: Technical Data.

Appendix E: LabVIEW® Programs

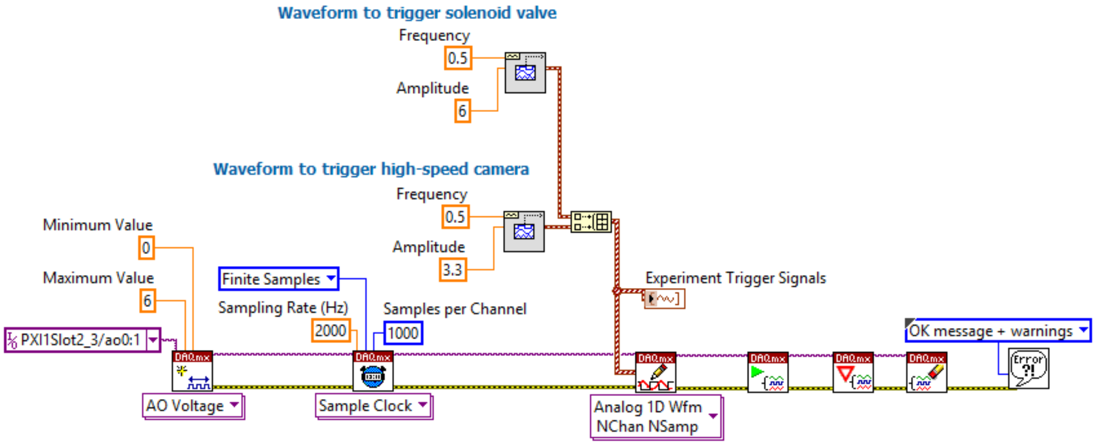

Figure E.1: Trigger Signals Subprogram Back Panel
This program analog output voltage signals used to trigger the solenoid valve and high speed camera.

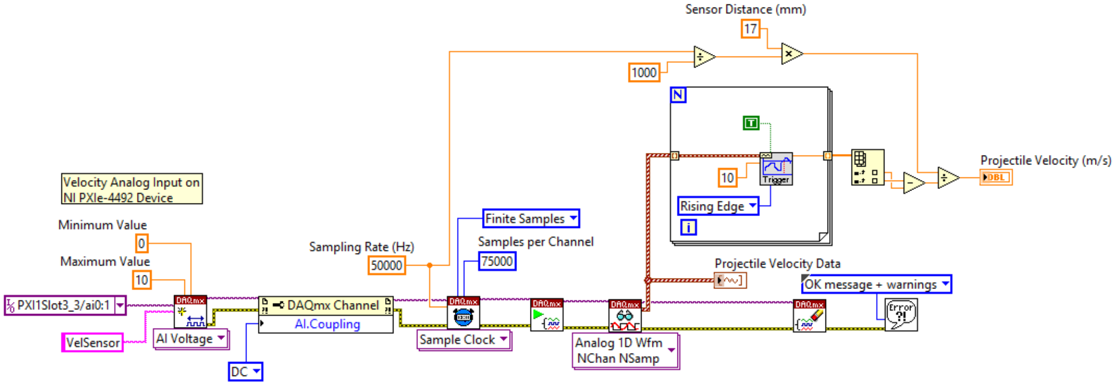

Figure E.2: Calculate Projectile Velocity Subprogram Back Panel
This program uses the data from the photoelectric sensors to calculate the velocity of the projectile, which is then displayed on the front panel.

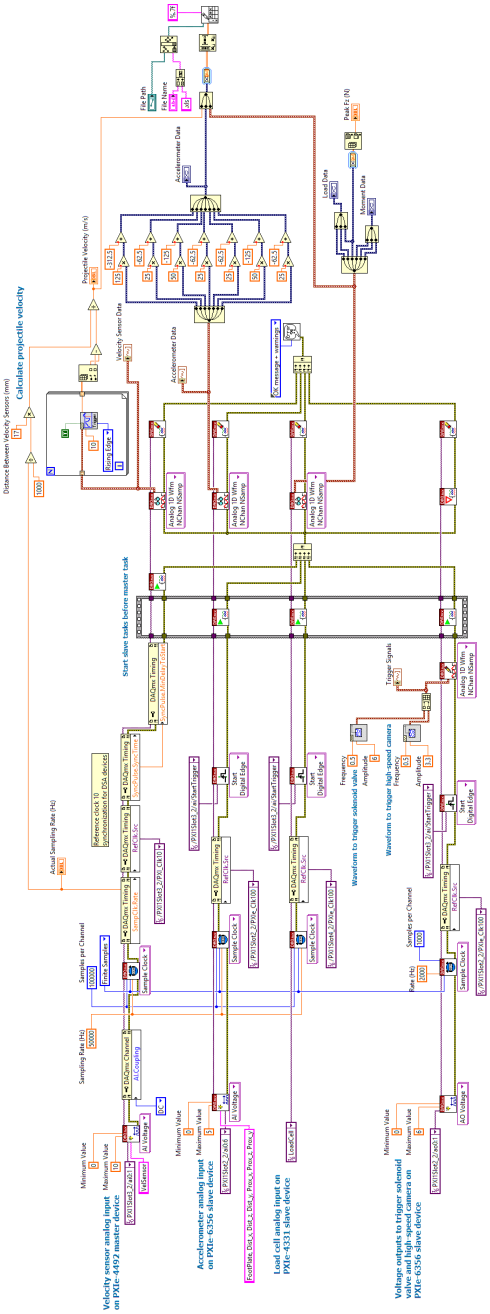

Figure E.3: Main Experiment Back Panel

The main experiment back panel included the inputs for the photoelectric sensors, accelerometers, and load cells, and also included the trigger signals and projectile velocity subprograms. All data acquisition and triggering was synchronized across all modules. The instrumentation data was displayed on graphs in the front panel and saved into a user-indicated file path. The accelerometer offsets from the accelerometer calibrations were included in the program.

Appendix F: Pneumatic Impactor Calibration Curves

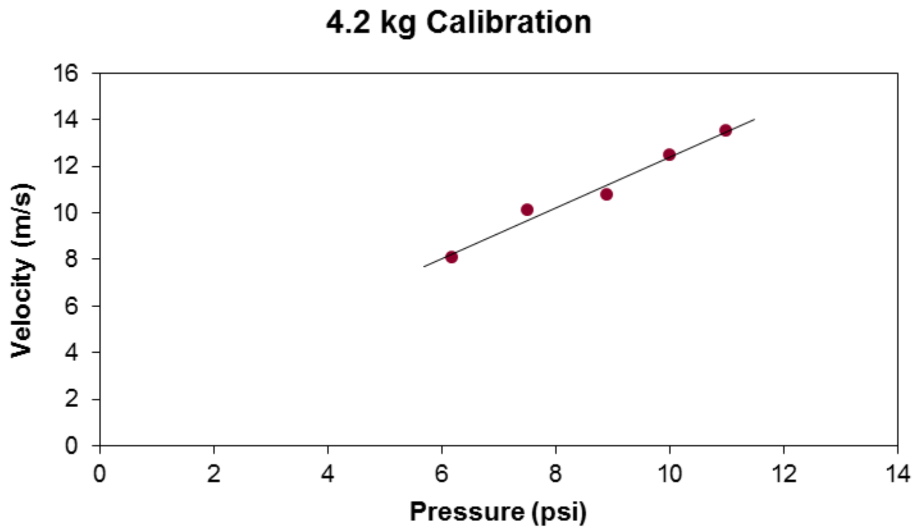

Figure F.1: Calibration Curve for 4.2 kg Mass
Projectile velocity as a function of tank pressure, $R^2 = 0.978$.

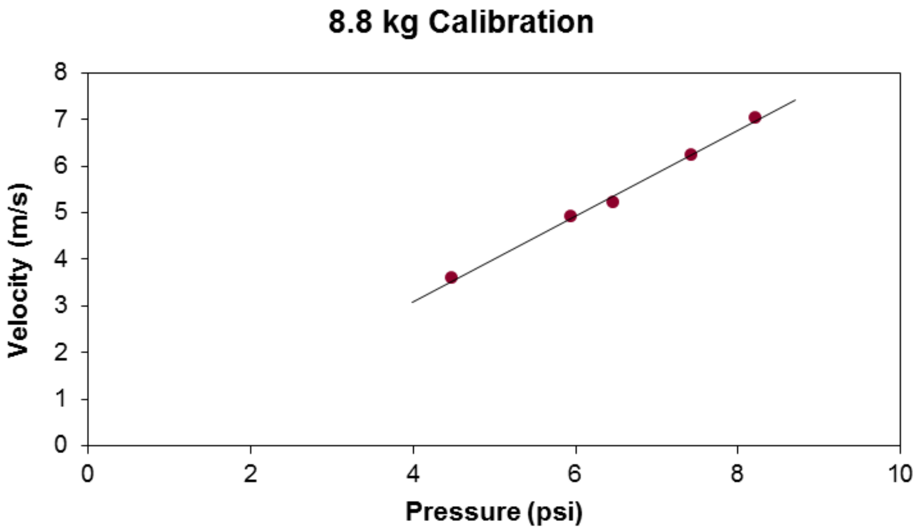

Figure F.2: Calibration Curve for 8.8 kg Mass
Projectile velocity as a function of tank pressure, $R^2 = 0.996$.

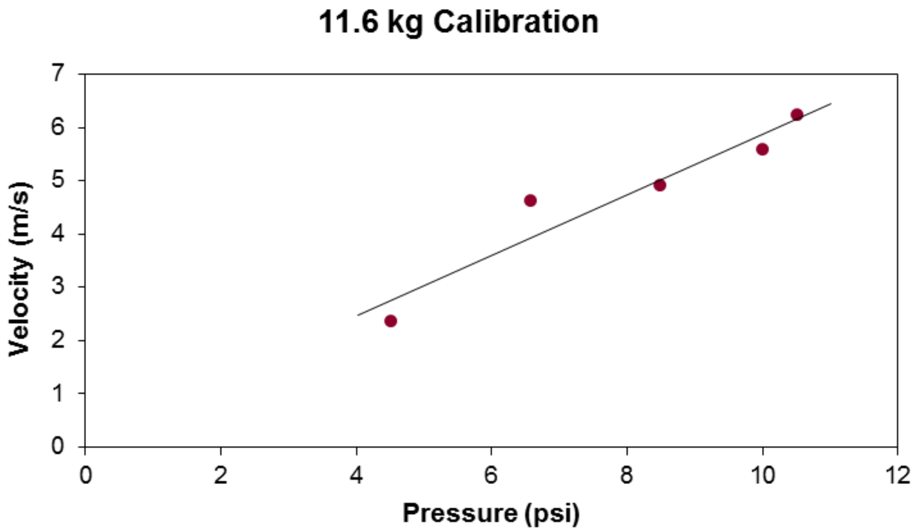

Figure F.3: Calibration Curve for 11.6 kg Mass
Projectile velocity as a function of tank pressure, $R^2 = 0.913$

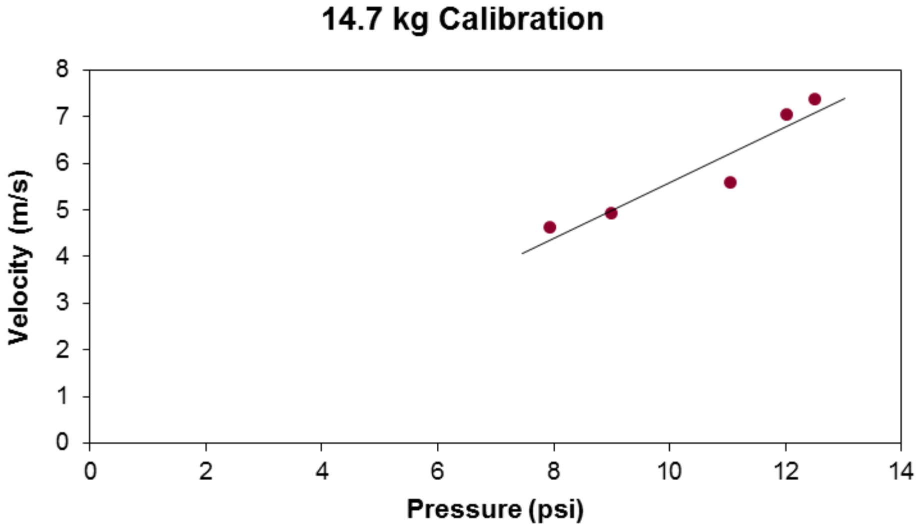

Figure F.4: Calibration Curve for 14.7 kg Mass
Projectile velocity as a function of tank pressure, $R^2 = 0.901$.

Appendix G: Detailed Impact Data

Table G.1: Detailed Impact Data

Detailed impact data is presented for all specimens for both the **a)** lower-rate automotive and **b)** higher-rate military test conditions. Fracture data from the last impact that was delivered to the specimen are presented on the right, while data from previous impacts that contained peak values are on the left. Data from the final fracture impact were used for statistical analysis, unless one of the previous non-injurious impacts contained a greater value. Data for all factors from the non-injurious impact that contained a peak value were included, while bolded values represent peak values that were greater than the value for that factor for the final fracture impact, and as such, were used for statistical analysis. For the rows that do not contain data for the non-injurious tests, the peak values occurred at the final fracture impact for that specimen, and as such, no data from the non-injurious impacts replaced values from the fracture impact for statistical analysis. Average and standard deviation values are shown for the fracture impact data but were not calculated for the non-injurious tests.

a)	Lower-Rate (Automotive) Impact Condition									
	Peak Values from Non-Injurious Impacts					Fracture Impact				
Specimen	Projectile Mass (kg)	Force (kN)	Kinetic Energy (J)	Impulse (Ns)	Load Rate (kN/ms)	Projectile Mass (kg)	Force (kN)	Kinetic Energy (J)	Impulse (Ns)	Load Rate (kN/ms)
1494R	27.8	**10.6**	**435**	**53.8**	**2.3**	31.6	8.1	381	32.7	1.2
1536R	25.0	**10.8**	**442**	**57.1**	**1.2**	31.6	7.0	381	50.8	1.2
1538L	-	-	-	-	-	21.0	9.1	449	26.1	1.3
1541L	31.6	10.1	501	**62.7**	1.9	34.6	12.8	603	33.1	2.5
1567L	31.6	9.4	551	**45.0**	**2.3**	34.6	11.3	666	34.7	1.8
1600R	21.0	5.6	**564**	**48.4**	0.7	21.0	11.0	449	21.1	3.7
Average (±S.D.)	-	-	-	-	-	29.1 (6.4)	9.9 (2.2)	489 (119)	33.1 (10.1)	2.0 (1.0)

b)	Higher-Rate (Military) Impact Condition									
	Peak Values from Non-Injurious Impacts					Fracture Impact				
Specimen	Projectile Mass (kg)	Force (kN)	Kinetic Energy (J)	Impulse (Ns)	Load Rate (kN/ms)	Projectile Mass (kg)	Force (kN)	Kinetic Energy (J)	Impulse (Ns)	Load Rate (kN/ms)
1494L	-	-	-	-	-	6.9	13.3	443	22.1	4.6
1536L	7.6	**14.3**	**594**	**30.3**	**9.2**	8.3	13.3	548	22.9	3.2
1538R	6.9	**13.5**	443	**27.3**	**4.7**	8.3	7.3	533	14.9	2.2
1541R	6.3	**11.8**	417	**27.3**	2.9	6.5	10.2	429	18.8	3.7
1567R	6.3	10.5	405	**27.3**	2.6	6.9	13.3	443	18.2	6.2
1600L	6.3	**14.5**	**612**	**25.9**	**4.8**	7.6	12.6	408	21.6	4.4
Average (±S.D.)	-	-	-	-	-	7.4 (0.8)	11.6 (2.5)	467 (58)	19.8 (3.0)	4.0 (1.4)

Appendix H: Detailed Specimen Information

Table H.1: Specimen Information
The donor number, age, side, potted mass, and length are given for all the tibia specimens used during experimental testing in Chapter 3. All donors were male, and each provided a pair of tibias.

Donor	Age (years)	Right/Left	Potted Specimen Mass (kg)	Tibia Length (m)
1494	50	L	1.47	0.40
		R	1.56	0.41
1536	55	L	1.54	0.43
		R	1.58	0.43
1538	66	L	1.49	0.38
		R	1.48	0.40
1541	68	L	1.51	0.41
		R	1.52	0.41
1567	61	L	1.60	0.42
		R	1.53	0.41
1600	74	L	1.48	0.38
		R	1.49	0.37